On-Orbit Cryogenic Refueling: Potential Mission Benefits, Associated Orbital Mechanics, and Fuel Transfer Thermodynamic Modeling Efforts

Thesis

Presented in Partial Fulfillment of the Requirements for Degree Master of Science in the Graduate School of The Ohio State University

By

Justin Ronald Clark, B.S.

Graduate Program in Aerospace Engineering

The Ohio State University

2021

Thesis Committee:

John M. Horack, Adviser

Mei Zhuang

Mrinal Kumar

Abstract

The placement of cryogenic fuel/propellant depot stations in Earth orbit has the potential to transform the nature and operations for many types of spaceflight missions. Today, spaceflight missions are almost universally required to carry the entire amount of fuel required for the mission, for the entire duration of the mission, from the point of launch. This is the rough equivalent of making a drive from Ohio to California, requiring the traveler to bring along the total sum of gasoline required for the entire trip, without being able to 'fill-up' anywhere along the route. Obviously, this framework of travel greatly encumbers the breadth, scope, and efficiency of potential journeys. Cryogenic fuel/propellant depots have not been implemented because many technical, operational, and engineering challenges still exist. These must be overcome prior to the placement of usable on-orbit propellant depots. This thesis investigates three specific engineering challenges related to on-orbit propellant depots, and presents the current state, technological challenges, and ultimate benefits of on-orbit cryogenic refueling.

This thesis begins with a literature review of past and present research endeavors being undertaken to realize on-orbit refueling depots, focusing on the technologies necessary for and the orbital mechanics associated with cryogenic fuel depot operations. Then, an orbital dynamics study is conducted, and a method for computing refueling orbits to optimize total mission architecture mass savings over a no-refueling, single rocket case is presented. A MATLAB script has been written that allows for calculation and assessment of optimal refueling orbits around the Earth and Moon for deep space missions, utilizing specific impulses of engines and mass ratios of stages as inputs. Python is also used in conjunction with this MATLAB script to compute launch windows and to create dedicated plots to find optimal mission windows for minimizing mission energy requirements ("porkchop" plots). Next, the results of a parametric study

analyzing the effects of staging, mass ratio, and specific impulse on optimal refueling orbit placement and mass savings are shown and discussed. Specifically, this parametric study confirms that orbital refueling can offer significant launch vehicle mass savings, potentially providing equivalent missions for 1.4-7.3 times less total mass than the traditional single rocket architecture for two-stage rockets and enabling utilization of single-stage to orbit (SSTO) launch vehicles for more demanding missions. Additionally, upcoming missions, such as NASA's *Artemis 1* mission and a SpaceX Starship Mars mission are assessed with refueling in mind, and potential mass savings are tabulated for applicable optimal refueling architectures. Finally, the idea of sustainable, on-orbit cryogenic refueling infrastructures is discussed as a whole, with long-term effects on the human exploration of the solar system theorized and presented.

The second topic of research in this thesis concerns itself with developing technologies and methods needed to achieve on-orbit refueling. Specifically, the storage and transfer of cryogenic fuels between spacecraft tanks has been identified as a key issue, and so is addressed in this thesis. In the environment of microgravity, propellants are unsettled in their tanks and cannot be transferred with the receiving tank's vent valve open. For normal (storable) fuels few problems would arise. However, for cryogenic fuels, rapid conversion to a vaporized state can occur, causing the pressure to build within a tank. This process can ultimately force the vent valve on the receiving tank to open, relieving pressure but allowing for liquid fuel to escape. One method of solution here is to pre-chill the receiver tank to some "target temperature" that is sufficiently cold to then allow a non-vented fill (NVF) to take place. Predicting this "target temperature" is a key goal of this work, and a derivation based on the 1st Law of Thermodynamics is undertaken. This derivation is similar to what was done in Kim et al. (2016) but is extended to include heat leak from the space environment as well account for initial fill

levels in the receiver tank (a no-vent top off fill). Accounting for these specific factors subsequently allows for application of this prediction parameter to the entire no-vent fill and no-vent top off experimental database. The "target temperature" is computed for 158 historical tests over a wide range of fluids, injection methods, and tank geometries. Additionally, a parametric study is conducted to determine the influential factors that affect NVF, and an efficiency parameter is derived to determine the efficiency of a given no-vent fill process. Results indicate that the predicted "target temperature" (also known as the prediction parameter) can always predict the failure of a non-vented transfer if the thermal energy needing to be taken from the tank metal is too large for the transferred fluid to absorb. It is concluded here that the resulting pressure in the receiver tank depends on the specific filling method used and as such is path dependent. Therefore, transient modeling of the no-vent fill process is needed to sufficiently predict how a tank/injector/cryogen pair will behave.

The third technical chapter of this thesis presents work done on a trajectory subroutine for such a model, allowing a user to select tank geometry, fuel injection method, and specify dimensions of each. The program subsequently outputs parameters necessary for a transient 1st order no-vent fill model, including the height of the liquid-vapor interface in the tank, the average angle that injected fuel impacts the tank wall, and the average distance the fuel travels through vaporized fuel. Additionally, the subroutine is then applied to the available NVF historical tests for validation. In each research area of this thesis, limitations of the research and recommended future work to improve and supplement the findings in this thesis are addressed.

Acknowledgements

I would first like to acknowledge and thank Dr. Jason Hartwig of NASA's Glenn Research Center for all he has done for me throughout my graduate studies. Without him, none of this research would have been possible, and I am immensely grateful to him for his guidance and expertise on the topic of on-orbit cryogenic refueling. Dr. Hartwig's willingness to mentor me and trust that I can contribute to NASA's mission has allowed me to learn and grow as an engineer. I feel as though the work I accomplished with his team matters, and I am excited to present some of that work in this thesis.

I am very grateful to Dr. John Horack for offering to sponsor my continued work in this area of research, and without his support and guidance, I might have never aspired to reach this point. Dr. Horack has provided many opportunities to learn from, interact with, and become part of the wider aerospace community. Upon looking back, I realize how transformational these opportunities have been for my development as an engineer and as a person. I cannot imagine how my path would have been different otherwise, and I am exceedingly thankful for his mentorship.

I would also like to thank Dr. Elizabeth Newton and Ms. Jenny Shields of The Ohio State University's Battelle Center for Science, Engineering, and Public Policy. They have been instrumental in my development as a student at Ohio State. I have found a home at their center where I have been able to connect with students and professionals in an environment that fosters creativity, cultivates passion, and ultimately offers inspiration for all wanting to grow as young professionals.

Finally, I would like to extend love and thanks to my wonderful family and friends for all

their continued support throughout all these years. There have been many strenuous and challenging times, but it has always been reassuring to have a great support system behind me. I have been lucky to be able to conduct such challenging and exciting research, and ultimately, I know it has helped me develop as an engineer while contributing to human expansion into the cosmos.

Vita

2015……..Milford High School

2018……..Presented at the 69th International Astronautical Congress

2019……..B.S. Aerospace Engineering, The Ohio State University

2020……..Presented at the 71st International Astronautical Congress

Fields of Study

Major Field: Aerospace Engineering

Table of Contents

List of Figures

List of Tables

Acronyms/Abbreviations

Nomenclature:

a – Semi-major axis of the orbit, [km]

C – Specific Heat, [J/kg*K]

C3 – Characteristic Energy, [km^2/s^2]

CFM – Cryogenic Fluid Management

CFD – Computational Fluid Dynamics

d – Incremental Change

dt – Time step, [s]

dT – Temperature increment, [K]

h – Specific enthalpy, [J/kg]

ISRU – In-Situ Resource Utilization

Isp – Specific Impulse, [s]

LEO – Low Earth Orbit

LLO – Low Lunar Orbit

LV – Launch Vehicle

m – Mass, [kg]

$\dot{m}$ – Mass flow rate, [kg/s]

OTV – Orbital Transfer Vehicle

$\dot{Q}$ – Heat transfer rate, [W]

r – Radius of the body being orbited, [km]

SSTO – Single Stage to Orbit

T – Temperature, [K]

t – Time, [s]

TLI – Trans Lunar Injection

u – Internal energy, [J/kg]

Δ – Delta change

η – Efficiency definition 1

μ – Standard gravitational parameter, [m^3/s^2]

χ – Efficiency definition 2

Subscripts:

actual – Experimentally determined

avg – Average value

final – Final state

fluid – Fluid property

initial – Initial state

injector – Property of injector performance

inlet – Inlet or incoming fluid

sat – Fluid saturation value

tank – Tank metal property

target – Property of the tank where a fill can succeed

Chapter 1: Thesis Introduction

As increasingly ambitious missions to the Moon and Mars are planned for the coming years, payload masses must increase in order to fulfill these more demanding and complex mission architectures. Ultimately, this trend will result in increasing launch vehicle size, cost, and complexity. This is partly why one can see the development and planning of launch vehicles such as NASA's Space Launch System (SLS), SpaceX's Starship, and Blue Origin's New Glenn. Additionally, the exponential relationship between launch vehicle size and performance dictates that a method of operations and architecture be developed that limits the size of launch vehicles, while also keeping payload masses high. One potential solution to this problem lies with on-orbit refueling depots, where a given spacecraft can be launched with a smaller launch vehicle, refueled in orbit, and then allowed to continue its mission. Ultimately, such architectures could maximize payload masses, simplify staging requirements, and reduce launch vehicle masses. Furthermore, cryogenic fuels will be required for more demanding missions, as cryogenic fuels often have higher energy densities than storable alternatives, thereby increasing the performances of spacecraft propulsion systems while also reducing mission architecture masses. Cryogenic fuels are also capable of being produced via in-situ resource utilization (ISRU) at destinations such as the Moon and Mars. Today, many of the high-performance launch vehicles and deep-space mission architectures utilize cryogenic fuels for these very reasons. Consequently, any refueling depot for deep-space missions will likely be required to operate with cryogenic fuels.

The idea of cryogenic fuel depots is not a new one, and researchers have been developing the required technologies for decades. However, one downside to utilizing cryogenic fuels is the challenging engineering requirement to maintain the propellant in a liquid state, and directly leads to the many challenging issues of cryogenic fluid management (CFM) in a space

environment. Specifically, issues such as boil off, two-phase transfer, and more have made the realization of cryogenic fuel depots a challenge and are among the main hurdles remaining before any cryogenic refueling depot can become operational. Recently, however, development efforts at NASA and other space organizations to overcome the remaining technological challenges have made notable progress, potentially enabling the use of on-orbit cryogenic fuel depots within the next decade. Therefore, it is worth investigating how this technology might be implemented into today's space environment and assessing what benefits this technology might offer for planned future missions.

Overall, this thesis addresses a few of the most prominent remaining technical issues currently preventing cryogenic on-orbit refueling from being realized and used optimally. It begins with a thorough historical literature review to build on significant work undertaken to date, in efforts to realize on-orbit cryogenic fuel transfer and storage. This acquaints the reader with the historical body of work and allows this thesis to build off past research in a novel manner.

Chapter 1.1: Background

This section reviews the available literature and summarizes research work completed on the topic of on-orbit cryogenic refueling to date. Emphasis is placed on works that summarize the potential mission benefits of on-orbit refueling, such as mission mass and cost reductions. Additionally, works that identify past and present technological challenges preventing the realization of on-orbit refueling are also emphasized.

Chapter 1.1.1: The Conception of Orbital Refueling

The concept of on-orbit orbital refueling for spacecraft has been around since at least 1963, when Dyer Brainerd Holmes, the NASA Director of Manned Space Flight at the time, appeared before the U.S. House of Representatives for the 1964 NASA Budget Authorization. In the hearing, Holmes states of the Apollo program, "We plan to do many Earth-orbit missions. What we will not do is rendezvous a big tanker stage with another stage and refuel in Earth orbit". This testimony can be found in H.R. 5466: 1964 NASA Authorization Hearing (1964). Holmes states that NASA will not utilize orbital refueling in Earth orbit for the Apollo program, due to cost and complexity at the time. However, his testimony provides evidence that NASA has been researching orbital refueling since at least 1963.

Further supporting this point, at the 1964 meeting of The Working Group on Extraterrestrial Resources, Chairman William Henderson stated of Rollin Gillespie's paper titled "Impulse Propulsion Gains Resulting From 'Free' Retanking of Propellants on Various Orbits and Stations at the Earth, the Moon, Mars, and Venus", that,

> Of special significance, was the discovery that lunar resources could substantially decrease the earth launched propellant requirements for low velocity planetary missions if refueling were accomplished at a lunar liberation point. This approach, coupled with refueling in the vicinity of the planets, would make major manned planetary missions an economic reality (NASA, 1964).

In the paper itself, Gillespie creates plots of remaining fuel mass as a function of departure speed for a hypothesized single-stage rocket leaving from a few various orbits around the Earth, the Moon, Mars, and Venus. From this point, Gillespie demonstrates how the orbits can be combined and replotted to assess different refueling orbits and gives a few examples such as a round-trip to

Mars and a round-trip to Venus. Among his findings, Gillespie notes that, “Retanking a rocket at the cis-lunar liberation point [can be] shown to multiply ten-fold the cargo which can be sent on an interplanetary trip, assuming a propellant factory on the Moon” (Gillespie, 1964). This is quite a significant statement, and again provides evidence for the potential benefits of on-orbit spacecraft refueling. The author has found no further research pertaining to optimizing the orbital mechanics associated with refueling depots for deep space mission, and this is presumably due to the focus on enabling the technology in the first place.

Chapter 1.1.2: Identified Technical Challenges

Since the 1960s, research has almost exclusively consisted of answering the technical questions of cryogenic fuel storage, transport, and transfer of cryogenic liquids between tanks. In 2000, Dr. David J. Chato conducted an in-depth literature review of the technologies required for cryogenic on-orbit refueling. Some of the key technological issues identified in his paper included the development of vapor-free liquid outflow, control of liquid inflow to prevent liquid venting, and quick disconnects for on-orbit mating of transfer lines. Some of the specific technologies discussed included methods for achieving non-vented fills utilizing liquid hydrogen, propellant management devices (PMDs) for separation of propellant liquid and gas phases, and liquid acquisition devices (LADs) for transporting liquid helium between two tanks (Chato, 2000). Building off of this literature review, Glaister et al. (2011) published another technology assessment titled “Long Term Cryogenic Storage Technologies Overview for NASA Exploration Applications”, in which the main technical challenges preventing the realization of on-orbit refueling include: “1) microgravity mass gauging of stored cryogenic propellants; 2) high fill efficiency tank-to-tank propellant transfer in low gravity; 3) long duration low boil-off of stored

cryogens; and 4) controlled acquisition and flow of cryogenic propellants in low gravity environments" (Glaister et al., 2011). More recently, in a 2017 presentation by Johnathon Stephens and Wesley Johnson titled "Cryogenic Fluid Management: Technology Development Roadmaps", technology readiness levels, or TRLs, of technologies required for cryogenic orbital refueling are detailed with plans for readying them for mission utilization. Specifically, the presentation lays out which technologies would require in-space demonstration missions, depending on whether the technology would be affected by changes in the local gravitational acceleration. Additionally, the presentation mentions a planned 2023 demonstration mission for accomplishing demonstrations of these enabling technologies, and specific details of this mission are presented in the next subsection. Technologies discussed in the presentation include liquid acquisition devices, to ensure that purely liquid propellant can be pulled from a tank no matter the distribution of liquid and vapor in the tank; unsettled liquid mass gauging, to determine how much propellant is left in a tank; and high-capacity, high-efficiency 20K cryocoolers, to keep cryogens (i.e. hydrogen) in liquid form (Stephens et al., 2017). Once these technologies reach a TRL of 6, following successful operations in a realistic environment, they are deemed allowable for use in a wider range of tests and for use in actual spaceflight missions. Possession of these technologies would significantly aid in the development of on-orbit refueling capabilities.

Significant advancement for some of these key enabling technologies came in 2019 with the Robotic Refueling Mission 3, or RRM3. The mission consisted of a payload mounted on the exterior of the International Space Station (ISS), and aimed to test various CFM technologies. RRM3 successfully demonstrated key technologies such as zero boil-off of cryogenic methane, mass gauging via a radio frequency mass gauge (RFMG), and autogenous pressurization through use of a wick-and-heater technique. Unfortunately, other goals of the mission, such as on-orbit cryogen transfers and microgravity cryogen orientation management, could not be demonstrated

(Breon et al., 2019). RRM3 enabled significant progress, and further strengthens the author's view that all components necessary to enable utilization of on-orbit cryogenic refueling could be realized within a decade.

Still though, more research is needed, and one of the key technical challenges today concerns gaining the ability to predict the thermodynamic outcome of a no-vent fill (NVF) transfer, in which the vent valve of the receiving tank is kept closed, to prevent unwanted liquid loss in low-g. Transferring cryogenic fluids with a tank with a closed tank vent valve can lead to a buildup of boil-off gases if cold fuel interacts with a relatively hot tank, potentially raising tank pressure past its limit and leading either to the opening of the vent valve and the loss of fuel, or even physical damage to the tank. Processes that include droplet tracking and subsequent heat transfer, liquid-vapor interface movement, and pool boiling can significantly complicate fuel transfer modeling efforts. Their presence can significantly affect the outcomes of cryogenic fuel transfer methods or thwart fuel transfer efforts altogether. The loss of significant quantities of fuel during the transfer can render the overall benefits of cryogenic fuel depots null. Therefore, solutions clearly need to be found.

The first, and probably simplest, method for solving this issue of heat transfer to the transferred cryogen would be to utilize a cryocooler to chill a receiving tank to the saturation temperature of the fuel by having a cold cryocooler conduct the thermal energy out of the tank metal. The receiving tank could then be filled successfully. However, cryocoolers are still a developing technology. They require extra mass and may require a power supply a spacecraft cannot afford from a size, weight, energy, or complexity perspective. Therefore, it is necessary to examine the hypothetical case where a cryocooler malfunctions or a spacecraft cannot utilize one. One potential solution here is a fuel transfer method called "chill and fill". This method works by

injecting the cold fuel into the tank, whereby the fuel absorbs thermal energy from the tank itself, which is subsequently cooled. The absorption of energy by the fuel converts it to a warmer, gaseous form, where it is then vented. This process is repeated until sufficient energy has been removed from the tank, and a no-vent-fill or no-vent-top-off (NVF and NVTO) can subsequently be initiated. Unfortunately, valuable fuel mass is utilized to cool the tank, and so the "chill and fill" approach may be more costly than that of the cryocooler to successfully complete a NVF or NVTO. Note that the difference between NVF and NVTO is whether there is any fuel initially in the tank. If the receiver tank is empty when filling is commenced, then it is an NVF. If there is fuel in the receiver tank when filling is commenced, then it is an NVTO. Otherwise, both processes are identical. The difficulty with NVFs and NVTOs occurs when insufficient thermal energy has been removed from the receiver tank. As a result, the pressure in the tank can rise beyond the pressure of the supply tank, causing the pressure difference (delta-P) across the injector to become zero (or even negative) and terminating the flow into the tank. From this point, the hot tank can continue to heat the already injected fluid, causing the pressure to rise even further. In such a situation, the only solution is to vent the tank and risk the loss of liquid propellent.

Past research into predicting NVF/NVTO transfer success has been pursued, with all studies consisting of ground experiments, since any zero-g space experiment would be much more expensive. These NVF/NVTO experiments always have some pairing of a tank with different injection methods, cryogens, or both. These past experiments were aimed at better understanding the underlying mechanisms governing the resulting thermodynamic response of the system in order to predict the outcomes of theoretical 0-g cases in the future. Specifically, these experiments consist of Chato et al. (1990), Chato et al. (1991), Chato and Sanabria (1991),

Moran et al. (1991), Moran et al. (1993), Chato et al. (1993), Flachbart et al. (2013), Kim et al. (2016), Breon et al. (2019), and Hartwig et al. (2021), and will be further discussed later in this thesis.

Simulations of no-vent fill processes have also been constructed and include the works of Majumder (2013) and Ma et al. (2017). In Majumder et al., the Generalized Fluid System Simulation Program (GFSSP) was utilized to construct nodal models of both the fuel transfer line and the receiver tank from a historical test and compare the results. It was found for the receiver tank model that, "Agreement between test and predictions are good for propellant consumption. Discrepancies between test and prediction are observed in pressure and temperature history" (Majumder, 2013). Specifically, their NVF model seems to overpredict the heat transfer coefficient between the injected propellant and the tank walls, leading to the predicted fluid temperature and pressure being greater than what was experimentally measured for the nine-node tank model case. A plot of the predicted and experimentally measured fluid temperature is included below and was adapted from Figure 13 in Majumder (2013).

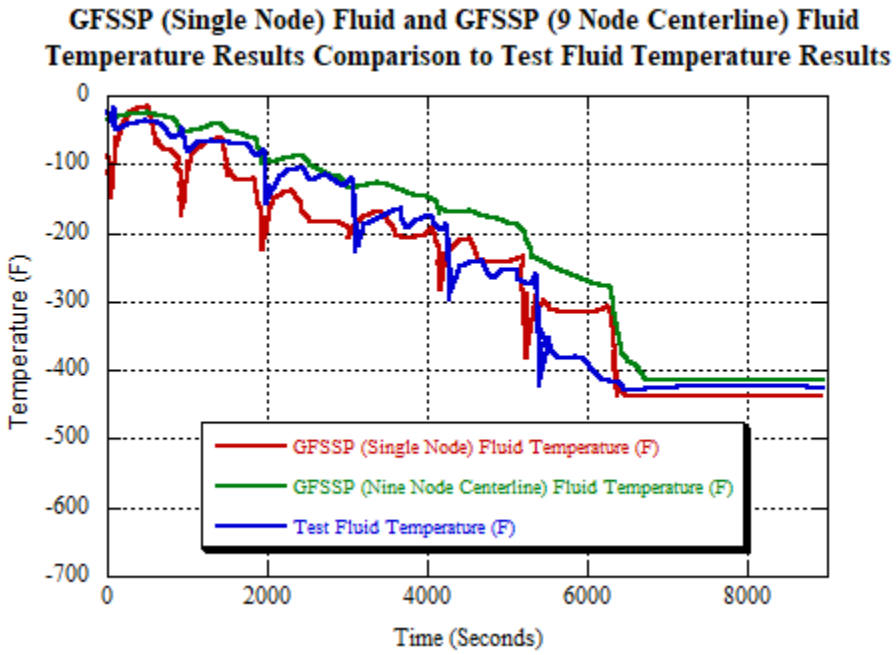

Figure 1.1: Predicted and Measured Fluid Temperature Adapted from Figure 13 in Majumder (2013)

Overall, the no-vent fill model was not accurate enough to properly predict the thermodynamic outcome of the system, and it is the position of this author that the model did not properly account for the trajectory of the injected cryogenic fuel and affecting the predicted heat transfer rates between the fuel and the tank wall. This is because the program (GFSSP) does not have the ability to simulate injection methods besides just filling from the bottom of the tank, due to its nodal basis.

In Ma et al. (2017), a computational fluid dynamics (CFD) study of Chato et al. (1993) is conducted by creating three different geometric cases with the same tank and different fuel injection methods. Liquid hydrogen is used as the fuel for two of the cases and liquid nitrogen for the other, with gravity set either at zero-g or 1-g, for a total of six simulations. Good agreement

between the CFD 1-g simulations and the experimental data from Chato et. Al (1993) was found for the temperature response, always within 5 K for all cases. However, the predicted pressure response had significant deviation from the experimental data, differing by 10s of kPa in some instances. This finding was especially true for the case involving liquid nitrogen, and a plot of the experimental and simulation pressure is included below. It is unclear to this author why the nitrogen case pressure deviated more than the hydrogen cases. However, it could be due to the fact that the initial tank pressure rise for cryogen injection cases involving LH2 is primarily governed by flashing, which may be easier for a CFD simulation to predict. On the other hand, for LN2, the flashing plays a less important role, due to the fact that LN2 will have a lower saturation pressure than LH2, and so the initial pressure rise will be more governed by boiling and interaction with the tank wall.

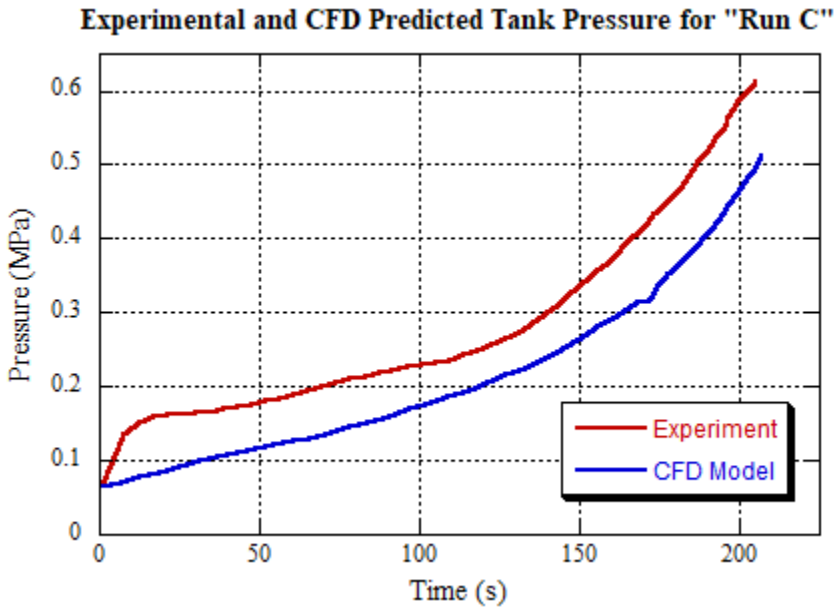

Figure 1.2: Experimental and CFD Predicted Pressure Curves for “Run C”. Adapted from Figure 7 in Ma et al. (2017)

A parametric study is also done in Ma et al. (2017) by varying the initial tank temperature, the temperature of the incoming fuel, the injection method, and the inlet mass flow rate. Overall, this study reveals that CFD simulations would need significant improvements to accurately and reliably predict the outcome of general no-vent fill cases. As has been shown, even with these past research efforts, the issue of being able to predict the success of a no-vent fill remains unsolved, and so unsuccessful or wasteful no-vent fills are still a possibility in the future. Therefore, the ability to predict when a no-vent fill will be successful is paramount to orbital refueling, and consequently is a topic of research in this thesis.

Chapter 1.1.3: Context in the Present Space Environment and Looking Forward

This work is presented at a time when some preliminary depot designs have already been proposed, such as the United Launch Alliance (ULA) depot design of Kutter et al. (2008) and McClean et al. (2011). However, their utilization has been prevented by issues including the reliable and successful transfer of cryogenic fuel from these depots. On-orbit testing is the only clean way to demonstrate these technologies in the relevant environment, and NASA has recognized that fact by putting even more emphasis on orbital refueling research and testing in recent years, and it is the hope of this author that many of the remaining technical challenges will be resolved over the next decade.

Looking forward, if cryogenic orbital refueling does become a reality, optimal utilization of on-orbit refueling technologies logically becomes an important issue needing addressed. Differences in utility may occur depending on where a refueling depot is positioned. Consequently, exploring where a potential optimal benefit is gained is extremely worthwhile.

While the exploration of optimal refueling orbits is something that has been mostly unaddressed in the literature since Gillespie (1964), this question will soon become relevant again if the technical issues of orbital refueling are resolved in the coming years.

Chapter 1.2: Thesis Overview

The first technical chapter of this thesis begins with an orbital dynamics study of on-orbit cryogenic refueling. Specifically, the ESA's PyKEP orbital mechanics library from Izzo (2017) is utilized with Python and MATLAB to determine where cryogenic fuel depots might be best positioned around the Earth and Moon for aiding human missions to deep space. The outputs of this program include plots of launch windows and characteristic energy for minimizing the energy and fuel required for the mission ("porkchop" plots) and estimates of optimal depot orbits for minimizing mass for locations in cis-lunar space. Next, required fuel masses are computed for propelling a spacecraft from a depot to a destination, such as Mars. From this point, the resulting launch vehicle masses are calculated to compute possible mass savings and compared to the masses required by traditional architectures not utilizing on-orbit refueling. Finally, the idea of sustainable on-orbit cryogenic refueling infrastructures is discussed as a whole, with the potential long-term effects on the human exploration of the solar system theorized and presented.

The next chapter of this thesis focuses on efforts aimed at overcoming the thermodynamic challenges associated with using cryogenic fuels, and presents work completed by the author under the mentorship of Dr. Jason Hartwig at NASA's Glenn Research Center. Work was done under the Reduced Gravity Cryogenic Transfer Project, or RGCT, and concentrated on thermodynamic modeling and optimization efforts for cryogenic fuel transfer processes between tanks. The project's efforts will not just enable the prediction of success or failure of cryogenic

fuel transfers, but will also uncover how such fuel transfers could be optimized to conserve fuel and remove engineering complexity. The work consists primarily of developing a 0^{th} order thermodynamic model for predicting fill success and overall fuel transfer efficiency, with historical data sets utilized to assess validity of this model. Additionally, a study of the different parameters involved in the system thermodynamics is conducted to determine which parameters have the greatest impact on the outcome of no-vent fills. Some of these parameters include inlet fuel temperature, supply tank pressure, tank wall thickness, and fuel type.

In the final technical section, Chapter 4, work was done to build a trajectory analysis code for supporting a transient 1-g thermodynamics model of the fill process to determine necessary properties of fuel injector-tank pairs. These properties include the average spray distance, the surface area of spray hitting the tank wall, the surface area of the ullage touching the wall, the surface area of the tank liquid touching the wall, the fraction of the spray going to the wall, and the fraction of the spray going to the liquid. The code also accounts for variation in the tank fill fraction, so that these properties can be assessed from 0 to 100% of fill of liquid. This thesis focuses on the trajectory portion only, and other aspects of the overall transient model are beyond the scope of this dissertation.

Chapter 1.3: Disclaimer

This thesis is a coherent and integrated assembly of published and unpublished original research work on the topic of on-orbit refueling, with co-authors and publication information specified below. Permission has been obtained by all necessary publishers, co-authors, and organizations to allow for the reproduction of the author's work into this thesis. Specifically,

these parties include Dr. Jason Hartwig of NASA's Glenn Research Center, Dr. John Horack of Ohio State University, Dr. Elizabeth Newton of Ohio State University, the International Astronautical Congress, NASA, the Battelle Center at the Ohio State University, and the research journal Cryogenics. The published work included in this thesis is cited as Clark et al. (2020) and Clark and Hartwig (2021).

Chapter 2: An Assessment of On-Orbit Cryogenic Refueling: Optimal Depot Orbits, Launch Vehicle Mass Savings, and Deep Space Mission Opportunities

Chapter 2.1: Theory and Calculation

The primary motivation behind this study is the theory that due to the exponential relationship of delta-V and launch vehicle mass, as articulated in the Tsiolkovsky rocket equation, (Equation 2.1 below), refueling may allow for 2+ launch vehicles, carrying 1+ refueling depot(s), and resulting in a total architecture mass less than a single, large launch vehicle. A short proof for demonstrating this possibility is included in Appendix A: Refueling Theory Proof.

$$\Delta V = g_0 * Isp * \ln\left(\frac{m_0}{m_f}\right) \tag{2.1}$$

The primary question this chapter aims to explore is as follows: Where might refueling depots be best positioned to minimize overall mission architecture mass necessary for a mission? Overall mission architecture mass consists of both the initial mass of the rocket carrying the primary payload (deemed the primary rocket), and the mass of the rocket required to get the depot to orbit and to refuel the primary rocket (deemed the secondary rocket). Optimization over the ensemble of the primary and secondary rockets is critical, as focusing only on the initial mass of the primary rocket could yield a situation where the primary rocket is quite light, but the depot and launch vehicle used to take the depot to orbit are extremely large, limiting any meaningful mass savings for the overall mission.

To further explore the methods used to calculate these optimal refueling orbits, the idea of minimum and maximum refueling depot usage cases needs to be introduced. Minimum depot usage

is considered in this chapter to mean no depot use at all, i.e. only utilizing a single rocket to accomplish the entire mission, with no refueling whatsoever. Maximum depot usage, on the other hand, means that the primary rocket launches and arrives to a specified orbit completely empty, refuels, and then continues with its mission. With these two bounds defined, a series of constraints and assumptions can be used to simplify the problem.

Chapter 2.1.1: Assumptions and Constraints

The first constraint is straightforward, since in any case, whether minimum or maximum depot use, it is known that the primary and secondary rockets must always achieve at least a circular LEO orbit prior to refueling, otherwise the rocket will not be able to remain in space to complete its mission, regardless of refueling. The successful arrival of both rockets into a stable LEO might represent a lower bound for any potential refueling scenario, both in terms of orbit altitude and energy required to it.

The next constraint is more practical and is the decision by the authors to only look at launches from NASA's Kennedy Space Center in Florida. This choice simplifies the analysis by removing multiple launch sites as a variable. Kennedy Space Center was chosen due to its relevance to cis-lunar mission plans in the United States, and its frequent launch cadence, although any other launch site would have been an equally valid choice for analysis. An average of 9.5 km/s of delta-V is required from a rocket flying due East from Kennedy Space Center to reach a 200 km by 200 km LEO with an inclination of 28.5° (Graham, 2008). This delta-V includes considerations such as steering losses, aerodynamic drag, and gravity losses. Additionally, this analysis assures that the rocket carrying the refueling depot also launches from the same location and in the same direction. Other launch sites for launching the tanker rocket are not considered, due to the

complexity of analysis that would be introduced.

To achieve higher orbits, for example, achieving a hyperbolic trajectory for a deep-space mission, a spacecraft will most likely try to benefit from the Oberth Effect to utilize its fuel as efficiently as possible (Adams et al., 2010). The significance of the Oberth Effect is due to the fact that at higher speeds, firing a spacecrafts reaction engine generates a greater change in the spacecraft's kinetic energy than at lower speeds. This means that when in orbit around a body, firing an engine at the point of highest speed (the periapsis) is more efficient than firing at any other point in the orbit. Therefore, it would be in the benefit of the mission designer to fire the spacecraft's engine at periapsis when trying to achieve a hyperbolic orbit, such as in the case of an interplanetary mission. However, the spacecraft does not have to burn all its fuel at once to achieve the hyperbolic orbit. Instead, the spacecraft can burn some of its fuel at one moment in time, achieve an elliptical trajectory, and then burn later in the orbit when the craft has returned to perigee. In terms of energy, these two processes are identical, and therefore little-if-no penalty in terms of delta-V is incurred by the craft staying for a short time in the elliptical orbit. To prove this, Equations 2.2 through 2.6 below first compute the delta-V (ΔV_1) required for a single burn from a circular orbit with an altitude of X km, to an elliptical orbit with a periapsis of X km and an apoapsis of Y km. This result is then compared to the delta-V (ΔV_2) of another case where one burn (with delta-V $\Delta V_{2,1}$) is used to change from a circular orbit with an altitude of X km, to an elliptical orbit with a periapsis of X km and an apoapsis of $Z < Y$ km, and another burn (with delta-V $\Delta V_{2,2}$), where an engine is fired at the periapsis to increase the apoapsis from Z to Y km. The Vis-Viva equation (Equation 2.2) is used for this proof, with μ being the standard gravitational parameter of the body of interest, "a" being the semi-major axis of the current orbit, and "r" being the radius of the planet or other body.

$$V = \sqrt{\mu\left(\frac{2}{r} - \frac{1}{a}\right)} \tag{2.2}$$

$$\begin{aligned}
\Delta V_1 &= V_Y - V_X \\
&= \sqrt{\mu\left(\frac{2}{r+X} - \frac{1}{a_2}\right)} - \sqrt{\mu\left(\frac{2}{r+X} - \frac{1}{a_1}\right)} \\
&= \sqrt{\mu\left(\frac{2}{r+X} - \frac{2}{(r+X+r+Y)}\right)} - \sqrt{\mu\left(\frac{2}{r+X} - \frac{2}{(2r+2X)}\right)} \\
&= \sqrt{\mu\left(\frac{2}{r+X} - \frac{2}{(2r+X+Y)}\right)} - \sqrt{\mu\left(\frac{2}{r+X} - \frac{1}{(r+X)}\right)}
\end{aligned} \tag{2.3}$$

$$\begin{aligned}
\Delta V_{2,1} &= V_Z - V_X \\
&= \sqrt{\mu\left(\frac{2}{r+X} - \frac{1}{a_2}\right)} - \sqrt{\mu\left(\frac{2}{r+X} - \frac{1}{a_1}\right)} \\
&= \sqrt{\mu\left(\frac{2}{r+X} - \frac{2}{(r+X+r+Z)}\right)} - \sqrt{\mu\left(\frac{2}{r+X} - \frac{2}{(2r+2X)}\right)} \\
&= \sqrt{\mu\left(\frac{2}{r+X} - \frac{2}{(2r+X+Z)}\right)} - \sqrt{\mu\left(\frac{2}{r+X} - \frac{1}{(r+X)}\right)}
\end{aligned} \tag{2.4}$$

$$\begin{aligned}
\Delta V_{2,2} &= V_Y - V_Z \\
&= \sqrt{\mu\left(\frac{2}{r+X} - \frac{1}{a_2}\right)} - \sqrt{\mu\left(\frac{2}{r+X} - \frac{1}{a_1}\right)} \\
&= \sqrt{\mu\left(\frac{2}{r+X} - \frac{2}{(r+X+r+Y)}\right)} - \sqrt{\mu\left(\frac{2}{r+X} - \frac{2}{(r+X+r+Z)}\right)} \\
&= \sqrt{\mu\left(\frac{2}{r+X} - \frac{2}{(2r+X+Y)}\right)} - \sqrt{\mu\left(\frac{2}{r+X} - \frac{2}{(2r+X+Z)}\right)}
\end{aligned} \tag{2.5}$$

$$
\begin{aligned}
\Delta V_2 &= \Delta V_{2,1} + \Delta V_{2,2} \\
&= \sqrt{\mu\left(\frac{2}{r+X} - \frac{2}{(2r+X+Z)}\right)} - \sqrt{\mu\left(\frac{2}{r+X} - \frac{1}{(r+X)}\right)} \\
&+ \sqrt{\mu\left(\frac{2}{r+X} - \frac{2}{(2r+X+Y)}\right)} - \sqrt{\mu\left(\frac{2}{r+X} - \frac{2}{(2r+X+Z)}\right)} \\
&= \sqrt{\mu\left(\frac{2}{r+X} - \frac{2}{(2r+X+Y)}\right)} - \sqrt{\mu\left(\frac{2}{r+X} - \frac{1}{(r+X)}\right)} \\
&= \Delta V_1
\end{aligned}
\tag{2.6}
$$

The utility in this approach is that a spacecraft could launch from the Earth, achieve LEO, burn at perigee to achieve an elliptical orbit, refuel, then burn at perigee again to leave the Earth's sphere of influence on a hyperbolic trajectory without needing to produce additional delta-V as compared to the case where the spacecraft goes directly from LEO to the hyperbolic orbit. Therefore, any elliptical orbit between the initial LEO and a target elliptical or hyperbolic orbit could be used as a refueling orbit without generating any significant disadvantage in terms of delta-V. Note that any orbit higher than or equal to a parabolic orbit could not be used as a refueling orbit, since the craft would never return to perigee to continue to take advantage of the Oberth Effect.

Chapter 2.1.2: Optimal Refueling Orbit Calculation Method

Given the required delta-V the spacecraft needs to expend from LEO to complete its mission to another planet or moon (on the order of 1 km/s), the mass of the payload, the specific impulse (Isp) of each stage engine system, and the mass ratio of each stage, the method for finding the optimal refueling orbit is done by calculating overall architecture masses required for refueling in individual orbits, starting with LEO. Specifically, the process of finding the overall architecture

mass for a given orbit begins by finding the minimum rocket mass to get the payload to the current refueling orbit being analyzed. For a single-stage rocket, this can be done simply by solving the Tsiolkovsky Rocket Equation. For a two-stage rocket, this is done by finding the optimal delta-V distribution between stages, and then finding the overall mass of the launch vehicle. Equations 2.7 through 2.9 below describe how each stage contributes to the overall required delta-V to get to orbit for an example two-stage rocket. The equations are derived from the Tsiolkovsky Rocket Equation, with g_0 being the gravitational acceleration at the Earth surface (9.81 m/s^2), Isp_1 being the specific impulse of the first stage rocket's propulsion system, Isp_2 being the specific impulse of the second stage rocket's propulsion system, m_{s1} being the mass of the structure of the first stage, m_{s2} being the mass of the structure of the second stage, m_{p1} being the initial mass of the propellant of the first stage, m_{p2} being the initial mass of the propellant of the second stage, and $m_{payload}$ being the mass of the payload.

$$\Delta V = g_0 * Isp * \ln\left(\frac{m_{\text{intial}}}{m_{final}}\right) \tag{2.7}$$

$$\Delta V = g_0 * Isp_1 * \ln\left(\frac{m_{initial}}{m_{initial} - m_{p1}}\right) + g_0 * Isp_2 * \ln\left(\frac{m_{initial} - m_{p1} - m_{s1}}{m_{initial} - m_{p1} - m_{s1} - m_{p2}}\right) \tag{2.8}$$

$$\Delta V = g_0 * Isp_1 * \ln\left(\frac{m_{s1} + m_{s2} + m_{p1} + m_{p2} + m_{payload}}{m_{s1} + m_{s2} + m_{p2} + m_{payload}}\right) + g_0 * Isp_2 * \ln\left(\frac{m_{s2} + m_{p2} + m_{payload}}{m_{s2} + m_{payload}}\right) \tag{2.9}$$

Again, it is assumed that it takes an average of 9.5 km/s of delta-V to get to a 200x200 km

LEO, so any orbit higher than LEO has the delta-V required to get to that higher orbit from LEO plus 9.5 km/s. That delta-V is then used to find the minimum launch vehicle mass to get the payload to that orbit, with the launch vehicle arriving empty. From this point, two cases exist. In the first case, the delta-V required by the spacecraft to complete its mission from the refueling orbit is less than or equal to the delta-V the refueled uppermost stage of the minimum mass launch vehicle can provide. Here, the uppermost stage can simply be partially or completely refueled and allowed to continue its mission. Note that in this case the launch vehicle cannot be further downsized for this orbit, since the primary rocket is still always required to get that payload to the refueling orbit in the first place.

In the second case, the delta-V required to complete the mission from the refueling orbit is greater than the delta-V of the uppermost stage of the minimum mass launch vehicle can provide. Here, the mission requires that the launch vehicle be upsized. One method of achieving this upsizing consists of sizing the uppermost stage of the primary launch vehicle to provide the necessary delta-V from this orbit, and then finding the required structural mass for the uppermost stage to carry the required fuel. From here, the uppermost stage of the launch vehicle from Earth is constrained to have the required structural mass just calculated, and then the optimal division of delta-V between the stages is found. The upsized primary launch vehicle overall mass can then be computed. In this case, it is possible to have the primary rocket launch with the uppermost stage at less than full, since the vehicle can now provide more delta-V than required to get to the refueling orbit, initially full. The primary launch vehicle in this case will also reach the refueling orbit empty. Note that since the uppermost stage of the primary rocket is sized to provide the necessary delta-V from that orbit, it will always be refueled here to 100% capacity, instead of a partial refueling.

A second method of upsizing the primary launch vehicle could be to find the required structural mass of the uppermost stage, as before, but then always fill the uppermost stage

completely, and size the lower stages based on their optimum delta-V distribution found earlier in the minimum mass rocket case. The motivation here is the idea that having any excess structural mass leads to a more inefficient rocket, so forcing the rocket to be completely full at launch may prove more efficient. This approach may cause the uppermost stage to arrive only partially empty to the refueling orbit. However, any leftover fuel resulting from this method would be fuel that does not need to be carried by the refueling depot and rocket, and the refueling depot would therefore only need to "top-off" the uppermost stage. A priori, it is unclear which of these two methods yields lower overall mission masses. Therefore, both methods are explored in this study. A flowchart diagram of the refueling methods discussed thus far is presented below in Figure 2.1 for visualization and includes steps additional steps to be discussed.

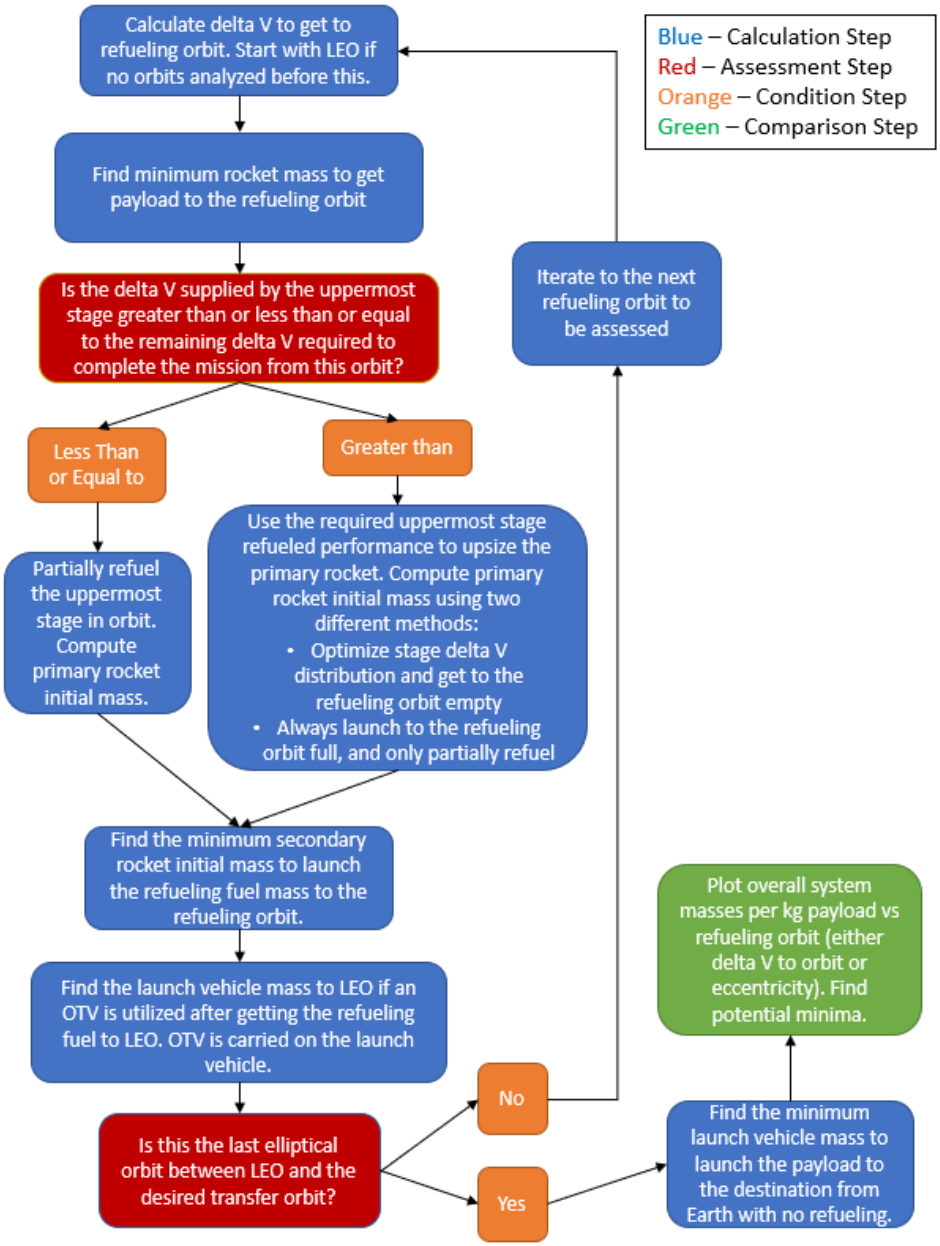

Figure 2.1: Optimal Orbit Computation Flowchart

From this point, the required amount of fuel to refill is computed and the minimum launch vehicle mass to get the fuel to the desired refueling orbit is found. Overall mission architecture mass will therefore be the sum of the refueling rocket(s), the primary rocket. and associated propellant. One possible alternate architecture for getting the depot to the refueling orbit could be

to utilize an orbital transfer vehicle (OTV) once LEO has been achieved, and then boosting the refueling depot up to the desired orbit. The potential benefit here is that the OTV could utilize an efficient electric propulsion system, possibly alleviating mass from the secondary/refueling/tanker rocket, even though that rocket is required to carry all the fuel, structures, and engines of the OTV. This trade-space is also explored by the author.

This entire process is then repeated for each orbit between LEO and the target orbit, with perigee altitude fixed at 200 km and the eccentricity incremented in steps of 0.01 until the target orbit it reached, or the Earth-centric orbit is no longer elliptical, i.e. a parabolic orbit with e = 1. For example, if going to Mars, a mission could launch to LEO, then burn to change inclination and to achieve a hyperbolic trajectory. Therefore, the valid refueling orbits for this case would be any elliptical orbit with an eccentricity between 0 and 0.99, a perigee altitude of 200 km, and an inclination between the initial LEO and target hyperbola. Another example might be that a spacecraft is trying to reach GEO, and so the nominal trajectory would get to LEO, burn to change inclination and to achieve the elliptical Hohmann transfer orbit, and then burn at apogee to circularize. The valid refueling orbits here would be all elliptical orbits in all inclinations between the initial LEO and the elliptical Hohmann transfer orbit, and for a perigee altitude of 200 km, the orbits assessed in this analysis would have eccentricities ranging from 0 to 0.72. Note that the trajectory in this case is not what a modern-day mission would take, but still provides a visualization for the reader. Unfortunately, investigating all valid inclinations between the two orbits would add another degree of freedom to this analysis, and so as a simplification, only eccentricities co-planar with the initial LEO are assessed throughout this chapter.

Finally, the overall mission architecture masses for the valid refueling orbits are assessed, and minima can be found. Additionally, using the required delta-V the spacecraft needs to produce from the surface of the Earth to complete its mission, the mass of the payload, the Isp and thrust of

each stage engine system, and the mass ratio of each stage, the optimal delta-V distribution between stages and the minimum rocket mass can be computed, giving the mass of the case where a singular rocket is used to complete the mission, with no refueling. Mass savings comparisons can then be conducted. Note that all mass calculations are computed with a normalized payload mass, so that the overall mission architecture mass is the overall mission architecture mass per kg of payload mass.

Chapter 2.1.3: Lunar Refueling for Interplanetary Missions

The following lunar refueling scenario for an interplanetary mission is utilized for this analysis: the primary rocket and payload achieves the same initial 200 x 200 km LEO as before, then an inclination change and boost burn is performed to intercept the Moon. Next, the rocket travels to a lunar orbit eccentricity between 0 and 0.99, by performing a capture maneuver at a perilune altitude of 50 km and an inclination of 6.67° above the equator of the Moon. Note that any other perilune altitude would be valid, and this 50 km was simply chosen as a simplification. Between these two eccentricities is where the process presented in chapter 2.1.2 can be used for finding optimal orbits with different specific impulses, mass ratios, staging methods, and OTV usage cases. Note that this 6.67° stems from the obliquity of the Moon, which is the inclination a spacecraft would arrive in from Earth if it intercepted the Moon directly from the lunar orbit plane. This information originates from Borough (2019), and a diagram of the system can be found in Figure 7 in the source.

After refueling, the rocket leaves lunar orbit with a hyperbolic excess velocity from lunar orbit that gives it the delta-V required to leave Earth orbit once back into the Earth's frame, and head to interplanetary space. The amount of fuel needed for the refueling process is based on the

delta-V necessary to finish the mission, i.e. the delta-V to leave the Moon plus the mission delta-V remaining after leaving Earth. Note that the delta-V for the refueling rocket to get to low-lunar orbit (LLO) can be assumed to be just the speed required to maintain the circular LLO, or 1.66 km/s due to minimal gravity drag with utilization of a gravity turn maneuver as described in Glasstone (1965) and a high-thrust system. One difference between lunar refueling and Earth-orbit refueling is that for the refueling rocket from the lunar surface, the delta-Vs involved to reach the rendezvous orbit do not warrant utilization of more than a single stage, since the mass of the refueling rocket will be small compared to primary rocket in most cases. Therefore, the refueling rocket is assumed to be a single stage rocket having the same specific impulse and mass ratio as the uppermost stage of the primary rocket for this study.

Concerning the inclinations involved, the spacecraft would change inclination at Earth to arrive at the Moon at 5.1° above the ecliptic, then once at the Moon (in the Moon's frame) the spacecraft will be inclined at 6.67° above the lunar equator. Note that the 5.1° results from launching due east from Kennedy Space Center at specific time of day and would be larger if launch occurs at another time. Finally, the spacecraft will change inclinations when leaving the Moon to achieve an orbit such that the hyperbolic excess velocity leaving the Moon will allow the craft to follow the necessary hyperbolic trajectory. Theoretically, valid refueling orbits here would be all eccentricities between the initial 6.67° inclination and the hyperbolic trajectory inclination. But as was stated earlier, this would add another degree of freedom to the analysis and take significantly longer to compute. Therefore, the initial spacecraft inclination of 6.67° is where the refueling orbits are assessed. See Figure 2.2 below for a diagram visualizing the inclinations between the Earth, Moon, and ecliptic plane.

The Python coding space in PyCharm (JetBrains, 2019) was one of the main programs

utilized over the course of this research, with the PyKEP module (Izzo, 2017) used to compute launch windows and develop plots of launch windows and characteristic energy for minimizing the energy and fuel required for interplanetary missions ("porkchop" plots). Additionally, NASA's General Mission Analysis Tool (GMAT) program (NASA Technology Transfer Program, 2018) was used for plotting 3D orbits to provide visualization of key results and examples.

MATLAB (The Mathworks Inc., 2019) was also employed to compute optimal orbits and mass savings for refueling in Earth and Moon centric orbits, following the method defined in the previous subsection. This script is an original contribution made by the author.

Chapter 2.2: Results and Discussion

This section presents the results of the parametric study, the NASA *Artemis 1* refueling impact study, and the SpaceX Starship refueling impact study in three distinct subsections. For each, a discussion of the results is also provided.

Chapter 2.2.1: Parametric Study

In order to complete a parametric study assessing the impacts of launch vehicle staging, mass ratio, engine specific impulse, OTV utilization, and lunar orbit refueling, a mission to place a payload in low-Mars orbit has been constructed. Note that for analyzing and comparing the effect of lunar refueling on interplanetary missions to Earth-centric refueling, it is imperative that common hyperbolic excess velocities and inclinations are used to place spacecraft utilizing either one on the same trajectory after entering interplanetary space. Also note that delta-Vs from either LEO or low-lunar orbit can be found from these constraints. Finally, the delta-V needed to place the spacecraft into low-Mars orbit is calculated, and the mission energy requirements are known.

Note that inclination changes between a due-East Cape Canaveral launch (28.5° above the equator and 5.1° above the ecliptic), the Moon (Also 5.1° above the ecliptic), and the nominal mission departure inclination were considered. Figures 2.3-2.5 below reveal the specific interplanetary trajectory chosen and the energy requirements to undertake it. For the "porkchop" plots in Figures 2.3 and 2.4, a modified version of Dario Izzo's Python script utilizing PyKEP from Izzo (2016). After the plots were made, minima of total characteristic energy (C3) between Earth departure and Mars arrival were found, and the launch opportunity in June 2035 was chosen as the energy-optimal mission window. Specifically, for a C3 of 17.27 km^2/s^2, an Earth departure hyperbolic excess velocity of 3.21 km/s inclined 7.87° above the ecliptic, and a Mars capture maneuver delta-V of 2.11 km/s, a 100 x 100 km orbit around Mars can be achieved in 200 days. These values were output from the Python script for the June 2035 mission window.

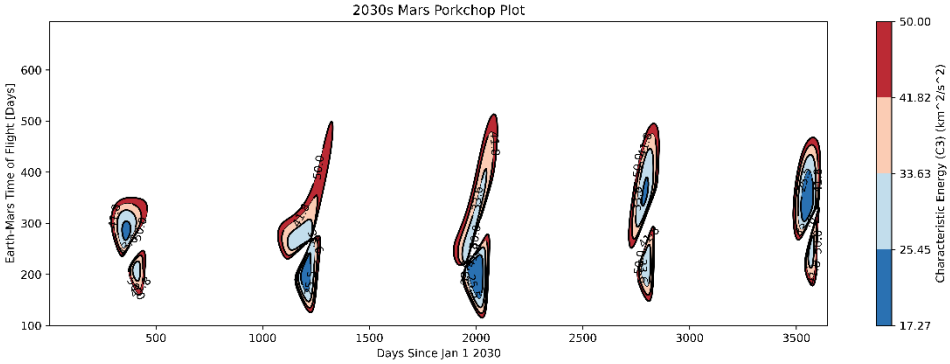

Figure 2.2: 2030s Mars C3 "Porkchop" Plot

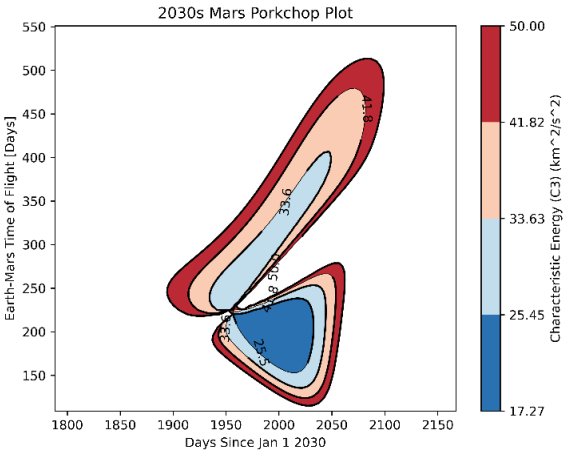

Figure 2.3: 2035-2036 Mars Mission "Porkchop" Plot

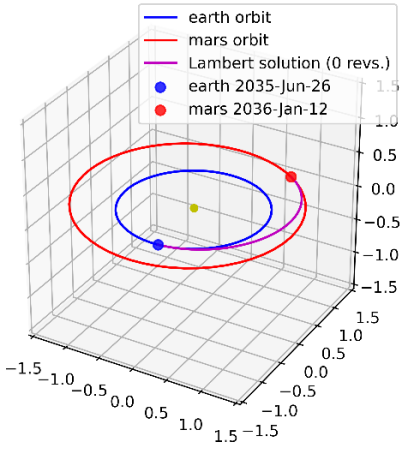

Figure 2.4: 2035-2036 Mars Mission Trajectory

For this parametric study, nothing is unique about setting low Mars orbit as the destination, other than that it yields constraints for this parametric study. Of course, changes in the mission destination will result in different requirements for the placement of the refueling depot, and so, this parametric study was done to understand how different parameters generally impact depot placement and mass savings, and their influences should be mostly independent of small variations in the mission specifics. The exception here would be if a mission is aimed at, for example, going to geostationary orbit (GEO) instead of Mars, since refueling in lunar orbit would be unnecessary for traveling to GEO.

Moving on, the methods and flowchart described in sections 2.1.2 and 2.1.3 can be followed, and the effects of engine Isps, rocket mass ratios, OTV utilization for transporting the depot from LEO to a higher orbit, and lunar refueling orbit usage on optimal refueling orbit placement and overall mission architecture mass can be found. For cases utilizing an OTV, an Isp of 3000 s and a mass ratio of 0.8 are used for the depot transfer vehicle utilizing an electric propulsion system. The results are given in Tables 2.1 through 2.4 below and are computed for a

two-stage rocket system refueling in Earth orbit, a single-stage-to-orbit system refuelng in Earth orbit, a two-stage rocket system refueling in lunar orbit, and a single-stage-to-orbit system refuelng in lunar orbit. In each case, the total architecture mass, the primary rocket initial mass, the tanker/secondary/refueling rocket initial mass, the refueling amount, the no-refueling singular rocket initial mass, the optimal orbit eccentricity, the fill fraction of the uppermost stage of the primary rocket at lift-off, and the fill fraction of the primary rocket uppermost stage prior to refueling are presented. Cases that utilize the OTV to supplement depot deployment are also specified.

Table 2.1: Two-Stage Rocket Earth Orbit Refueling Results

Two Stage Rocket Results (Earth Orbit Refueling)											
Set Up	**Orbital Tranfer Vehicle in Use?**	**Total Mission Mass per kg Payload**	**Primary Rocket Mass per kg Payload**	**Refueling Fuel Mass per kg Payload**	**Refueling Rocket Mass per kg Payload**	**Single Rocket Mass per kg Payload**	**Mass Savings (%)**	**Optimal Orbit e (28.5° Inc and Rp = 200 km)**	**Uppermost Stage Launch Fill Fraction**	**Uppermost Stage Refueling Fill Fraction**	**Notes**
MRs of .95 and ISPs of 400s	No	75.31	18.36	3.15	56.95	106.9	141.95	0.18	1	1	Near/at 1-1 fractions optimal zone
MRs of .95 and ISPs of 400s	Yes	59.25	31.06	1.74	28.19	106.9	180.42	0.7	1	0.4	Near/at OTV optimal zone
MRs of .95 and ISPs of 360 and 465s	No	53.86	12.14	3.44	41.72	84.95	157.72	0	1	0.55	Hits e = 0 bound limit
MRs of .95 and ISPs of 360 and 465s	Yes	46.87	23.19	1.79	23.68	84.95	181.25	0.6	1	0.24	Near/at OTV optimal zone
MRs of .95 and .85. ISPs of 400s	No	129.1	41.27	2.15	87.83	264.1	204.57	0.62	1	1	Near/at 1-1 fractions optimal zone
MRs of .95 and .85. ISPs of 400s	Yes	83.48	41.27	2.15	42.21	264.1	316.36	0.62	1	1	Near/at OTV optimal zone

Beginning with the case of a two-stage rocket refueling in Earth orbit, it is apparent that the stage mass ratios, the stage Isps, and OTV utilization all significantly affect the positioning of the optimal orbit, as well as the total mission architecture mass. This can be seen by looking at the optimal orbit eccentricity and total mission mass columns. Looking at the mass savings results, one can observe that even from this initial analysis, orbital refueling can lead to significant mass savings when the total mission mass and the no-refueling, single rocket case mass are compared. Specifically for the parameters involved in this case, the resulting mass savings over the single rocket case range from 1.5 to 3 times reduction. Additionally, it is significant that the optimal refueling orbits for the three non-OTV parametric cases all occur

where the initial launch vehicle fill fraction and the on-orbit refueling fraction are both maximized while maintaining an elliptical orbit. This finding makes logical sense as the optimal refueling case should occur when the rocket launches from the pad full, gets to the refueling orbit empty, and then refills completely once there. Additionally, this finding makes sense in that the amount of unused structural mass to carry fuel is minimized, increasing performance. Indeed, this is the optimal refueling scenario for non-OTV cases. For example, if a rocket launches, and only needs to be refueled partially in orbit to complete its mission, then there is some amount of mass of the rocket's structure that could have been further minimized. Next, OTV utilization is shown for each case (in its respective column) to either maintain or increase the optimal refueling orbit eccentricity, leading to only partial refueling being required as the balance between taking more fuel to a lower orbit and less fuel to a higher orbit shifts due to the efficiency of the OTV.

When looking at the effect of Isp on the optimal orbit position and necessary mission mass, it can be seen how decreasing the first stage Isp to 360s, and increasing the second stage Isp to 465s (from the base case of 400s) results in a decrease in the optimal orbit apogee. One reason this occurs is that by increasing the Isp of the second stage, it is able to contribute more delta-V for the same amount of fuel, meaning that the refueling condition where the craft arrives to the orbit empty and refills completely is able to take place at lower orbits. Additionally, when varying stage mass ratios, as decreasing the mass ratio of the second stage to 0.85 from 0.95 drives the optimal refueling orbit significantly higher.

Overall, for the two-stage Earth-refueling case, it is found that when increasing the size of the primary rocket to yield more delta-V is necessary, using the first upsizing method proves superior in terms of decreasing the resulting architecture mass. For this upsizing method, the optimal delta-V division between stages is found and the uppermost stage of the rocket can launch partially empty. This method proves especially superior when an OTV is in use as well, since it is better to maximize the amount of fuel brought to the refueling orbit by the more efficient OTV propulsion system.

Table 2.2: Single-Stage Rocket Earth Orbit Refueling Results

Single Stage Rocket Results (Earth Orbit Refueling)											
Set Up	**Orbital Tranfer Vehicle in Use?**	**Total System Mass per kg Payload**	**Primary Rocket Mass per kg Payload**	**Refueling Fuel Mass per kg Payload**	**Refueling Rocket Mass per kg Payload**	**Single Rocket Mass per kg Payload**	**Mass Savings (%)**	**Optimal Orbit e (28.5° Inc and Rp = 200 km)**	**Uppermost Stage Launch Fill Fraction**	**Uppermost Stage Refueling Fill Fraction**	**Notes**
MR of .95 and ISP of 400s	No	205.9	24.46	7.42	181.44	Not Possible	n/a	0	1	0.33	Hits e = 0 bound limit
MR of .95 and ISP of 400s	Yes	205.9	24.46	7.42	181.44	Not Possible	n/a	0	1	0.33	Hits e = 0 bound limit
MR of .95 and ISP of 465s	No	64.96	12.73	4.1	52.23	Not Possible	n/a	0	1	0.37	Hits e = 0 bound limit
MR of .95 and ISP of 465s	Yes	64.96	12.73	4.1	52.23	Not Possible	n/a	0	1	0.37	Hits e = 0 bound limit
MR of .85 and ISP of 400s	No	Not Possible									Primary Rocket is too large
MR of .85 and ISP of 400s	Yes	Not Possible									Primary Rocket is too large

The case of a single stage rocket refueling in Earth orbit presented in Table 2.2 yields entirely different results. Here, the optimal refueling orbit is the initial low-Earth circular orbit in four of the six cases. One reason for this difference between the single and two-stage rocket cases is that the single stage rocket always has to provide at least 9.5 km/s of delta-V at initial launch. Since the mission delta-V from LEO in this case is ~7 km/s, there is no need for the vehicle to go to a higher orbit to refuel, since the minimum rocket necessary just to get to LEO is already larger than needed for refueling. As stated before, if the rocket were to go to a higher orbit and refuel, the increase in size of the SSTO to get to that orbit would lead to more wasted structures upon refill, and this higher orbit would prove to be more inefficient. Additionally, the remaining two cases result in no possible mission completion scenario for the parameters

provided, due to the primary launch vehicle being too large to even reach LEO. Here, the system is constrained by the same type of performance limit on which all the non-refueled, single rocket base cases failed.

Table 2.3: Two-Stage Rocket Lunar Orbit Refueling Results

Two Stage Rocket Results (Lunar Orbit Refueling)											
Set Up	**Orbital Tranfer Vehicle in Use?**	**Total System Mass per kg Payload**	**Primary Rocket Mass per kg Payload**	**Refueling Fuel Mass per kg Payload**	**Refueling Rocket Mass per kg Payload**	**Single Rocket Mass per kg Payload**	**Mass Savings (%)**	**Optimal Orbit e (Moon, 6.7° Inc and Rp = 50 km)**	**Uppermost Stage Launch Fill Fraction**	**Uppermost Stage Refueling Fill Fraction**	**Notes**
MRs of .95 and ISPs of 400s	No	27.28	24.4	1.52	2.88	106.9	391.86	0.99	1	0.41	Hits e = .99 bound limit
MRs of .95 and ISPs of 400s	Yes	26.81	24.4	1.52	2.41	106.9	398.73	0.99	1	0.41	Hits e = .99 bound limit
MRs of .95 and ISPs of 360 and 465s	No	22.61	20.15	1.42	2.46	84.95	375.72	0.99	1	0.2	Hits e = .99 bound limit
MRs of .95 and ISPs of 360 and 465s	Yes	22.26	20.15	1.42	2.11	84.95	381.63	0.99	1	0.2	Hits e = .99 bound limit
MRs of .95 and .85. ISPs of 400s	No	36.86	33.3	1.68	3.56	264.1	716.49	0.99	1	0.923	Hits e = .99 bound limit
MRs of .95 and .85. ISPs of 400s	Yes	36.21	33.3	1.68	2.91	264.1	729.36	0.99	1	0.923	Hits e = .99 bound limit

Next, for the two-stage rocket lunar orbit refueling results, one can see from the mass savings column that significant mass savings can be realized in every cases. In one instance, a mass savings up to ~7 times over the non-refueled, single rocket case was found. These results occur because the refueling craft no longer needs to launch from Earth, but can instead launch from the Moon, needing less energy to rendezvous with the primary rocket. Here, launching from the lunar surface to a lunar orbit means a smaller gravity well (only 1.62 m/s^2 at the surface) and no losses due to aerodynamic resistance. When considering the effects of Isp and mass ratio, changes in parameters that limits performance of the second stage ultimately results in greater mass savings over the single rocket case. Optimal orbits for the three non-OTV cases all occur at the minimum, e = 0.99 lunar orbit with a periapsis altitude of 50 km. These optimal orbit locations result from the fact that the refueling rocket requires less fuel relative to payload mass than it would take for the primary rocket to go to a lower lunar orbit, leading to maximal use of the refueling rocket being more efficient. Utilizing an OTV for the 400 s Isp two-stage Luna-refueling case decreases the total system mass by 2.3 kg/kg of payload for the 400 s Isp. This can be compared with the 400 s Isp two-stage Earth-refueling case, in which the OTV

decreases the total system mass by 16.06 kg/kg payload. This disparity in the OTV utilization results between the Earth and Moon refueling cases is due to the fact that the OTV in the Earth refueling case is required to provide more delta-V than the Luna refueling case. Therefore, the resulting mass savings for the Earth-refueling OTV cases are greater. The optimal orbit for Luna refueling OTV utilization is where the primary spacecraft just enters orbit around the Moon (e = 0.99, again), and the OTV subsequently brings fuel from the lunar surface that orbit. This result is understandable as the OTV Isp offers much higher fuel efficiency, so minimalization of mass for the entire mission architecture will occur where OTV use can be maximized.

Table 2.4: Single-Stage Rocket Lunar Orbit Refueling Results

Single Stage Rocket Results (Lunar Orbit Refueling)											
Set Up	**Orbital Tranfer Vehicle in Use?**	**Total System Mass per kg Payload**	**Primary Rocket Mass per kg Payload**	**Refueling Fuel Mass per kg Payload**	**Refueling Rocket Mass per kg Payload**	**Single Rocket Mass per kg Payload**	**Mass Savings (%)**	**Optimal Orbit e (Moon, 6.7° Inc and Rp =**	**Uppermost Stage Launch Fill Fraction**	**Uppermost Stage Refueling Fill Fraction**	**Notes**
MR of .95 and ISP of 400s	No	124.3	108.9	8.14	15.4	Not Possible	n/a	0.99	1	0.08	Hits e = .99 bound limit
MR of .95 and ISP of 400s	Yes	122	108.9	8.14	13.1	Not Possible	n/a	0.99	1	0.08	Hits e = .99 bound limit
MR of .95 and ISP of 465s	No	29.43	25.48	2.28	3.95	Not Possible	n/a	0.99	1	0.1	Hits e = .99 bound limit
MR of .95 and ISP of 465s	Yes	28.94	25.48	2.28	3.46	Not Possible	n/a	0.99	1	0.1	Hits e = .99 bound limit
MR of .85 and ISP of 400s	No	Not Possible									Primary Rocket is too large
MR of .85 and ISP of 400s	Yes	Not Possible									Primary Rocket is too large

Finally, for the SSTO lunar refueling case, the results almost mirror the Earth orbit refueling SSTO case. Here, none of the non-refueling SSTO base cases are achievable, and the 400 s Isp/0.85 mass ratio refueling cases (OTV and non-OTV) are not possible as well. For the possible refueling cases, the optimal lunar refueling orbits were all found to be at the near-parabolic (e = 0.99) orbits for the same efficiency reasons discussed for the two-stage lunar refueling case.

Overall, some of the key findings in this section are as follow: 1) For a launch vehicle refueling in Earth orbit without utilizing an OTV, the optimal orbit will occur where the primary launch vehicle uses the entirety of its fuel and is then able to be refueled completely. This

assumes that the refueled uppermost stage of the launch vehicle is sized to exactly meet the mission delta-V requirements from the refueling orbit. 2) Orbital transfer vehicles utilizing an efficient electric propulsion system could be very beneficial when used to transport refueling depots to higher orbits. When OTVs are used to transport the depot to a higher orbit, the optimal refueling orbit is usually higher than the non-OTV case. 3) In the lunar refueling scenarios, results support the theory that utilization of lunar refueling orbits with fuel from the lunar surface can yield substantial mass savings, as much as ~7 times less than an equivalent single, non-refueled rocket (Table 2.3). 4) OTV utilization for lunar refueling orbits has also been shown to be beneficial but does not provide the same significant mass savings as in the Earth orbit refueling cases. Additionally, the optimal lunar refueling orbits were shown to be the highest possible eccentricity (e = 0.99 and periapsis altitude = 50 km) around the Moon, due to the increased efficiency of having a refueling rocket travel with less fuel to a higher orbit versus going to a lower orbit with more fuel. 5) In general, the lunar refueling results demonstrate consistency with those from Gillespie (1964). 6) Finally, the overall results illustrate the trend that as a launch vehicle becomes more inefficient (lower Isp, lower mass ratio) and as it is required to produce more delta-V itself, larger potential mass savings gained through utilizing orbital refueling are realizable. This behavior is directly a result of the exponential relationship between performance, efficiency, and mass presented in Equation 2.1 and the proof in Appendix A. Therefore, these results show that splitting the delta-V through refueling yields larger benefits relative to the no-refueling, single rocket case.

Chapter 2.2.2: *Artemis 1* Refueling Impact Study

NASAs upcoming *Artemis 1* mission plans to utilize the Space Launch System (SLS)

launch vehicle to send an unmanned *Orion* spacecraft with the European Service Module (ESM) to a distant retrograde orbit (70376 km above the lunar surface) around the Moon and back. A detailed mission architecture can be found in Figure 1 in Heaton et al. (2020). The main payload, *Orion* with the ESM, separates from the SLS after the trans-lunar injection orbit has been achieved, ultimately reaching lunar orbit and subsequently utilizing a gravity assist to return to Earth.

One way in which refueling could be adopted into this architecture would be to place a refueling depot in any elliptical orbit between the initial LEO and the highly elliptical trans-lunar injection orbit, while placing the *Orion*/ESM payload onto the trans-lunar injection orbit after refueling. Specifically, for this study, LEO is defined as a 200 X 200 km orbit inclined at 28.5°, and an average lunar orbit distance of 384,000 km from the Earth is used, resulting in a transfer ellipse eccentricity of 0.967. Consequently, all elliptical orbits up to between 0 and 0.96 are assessed. All details on the *Artemis 1* mission architecture used in this analysis originate from Heaton et al. (2020) and Smith (2017). Additionally, the solid rocket boosters used on SLS are not considered in this study, and so the launch vehicles utilized in this study are based on a rocket similar to SLS, but with only two liquid-propelled stages prior to *Orion*/ESM detachment. This is major simplification of the SLS system, but preliminary results for comparison can still be obtained.

Having defined a method of integrating refueling into the *Artemis 1* mission architecture, the rocket parameters must now be obtained to generate and examine results. From Smith (2017) and Kyle et al. (2020), the core-stage Isp of SLS is listed as 363s (at sea level), while the Interim Cryogenic Propulsion Stage Isp is listed as 462s. Mass ratios for these stages can be computed from the source data to be ~0.91 and ~0.89, respectively. The results from this analysis are

computed and shown in Table 2.5 below. For the non-OTV refueling case, the optimal refueling orbit is the initial circular LEO with an apogee of 200 km, offering about a 218% reduction in mass over the existing SLS Block 1 mass. For the OTV use case, the optimal refueling orbit will occur at an eccentricity of 0.14 (with a periapsis altitude of 200 km), resulting in a total architecture mass savings of about 222%. Note that the initial SLS Block 1 mass and payload mass to TLI were obtained from Dunbar et al. (2020) and are listed in Table 2.5. Interestingly, SLS Block 1 is slightly oversized for the *Artemis 1* mission requirements, as the launch vehicle is capable of sending a larger than required payload to TLI. This finding is simply due to the fact that SLS will be used in missions requiring more performance (delta-V) from SLS than *Artemis* 1 does.

Table 2.5: *Artemis 1* Refueling Study Results

Artemis 1 Refueling Study Results												
Set Up	**Total Mission Mass per kg Payload**	**Primary Rocket Mass per kg Payload**	**Refueling Fuel Mass per kg Payload**	**Refueling Rocket Mass per kg Payload**	**Single Rocket Mass per kg Payload**	**Mass Savings (%)**	**Exisiting SLS Mass per kg Payload**	**Mass Savings Over LEO Case (%)**	**Optimal Orbit e (28.5° Inc, Rp = 200 km)**	**Uppermost Stage Launch Fill Fraction**	**Uppermost Stage Refueling Fill Fraction**	**Notes**
Earth Orbit Refueling	46.02	18.47	1.49	27.55	68.63	149.13	100.32*	217.99	0	1	0.387	Hits e = 0 lower bound.
Earth Orbit Refueling w/ OTV	45.24	22.56	1.2	22.68	68.63	151.70	100.32*	221.75	0.14	1	0.284	Near/at OTV optimal zone
*Current SLS Setup is slightly oversized for Artemis 1. SLS is constructed for eventual upgrades, larger payloads, and more demanding missions.												

Chapter 2.2.3: Starship-Mars Mission Refueling Impact Study

SpaceX's Starship rocket is an ambitious, "super heavy-lift" launch vehicle attempting to establish the capability for human flights to Mars. Currently, the Starship mission architecture calls for refueling a primary Starship rocket in LEO prior to Earth departure (Musk, 2017). Therefore, assessment of optimal refueling orbits that may reduce total mission architecture mass are of general interest to the entire astronautics community, and so this short study is also presented as part of this thesis.

Existing Starship vehicle mass ratios and stage Isps were obtained from Musk (2017) and

implemented into the MATLAB orbital refueling code. Mass ratios of the first and second stages were given as 0.95 and 0.91, respectively. Isps of the first and second stages are stated to be 330s and 375s, respectively. It should also be noted that the mass ratios for the first stages and tanker second stages were adjusted by the author to be 0.85 and 0.82, respectively, to account for ~10% fuel saved for landing the SpaceX booster stage. Required mission delta-Vs of 4-6 km/s from LEO to a trans-Mars injection orbit and 1-2 km/s to capture and land on the Martian surface were are utilized and originate from Musk (2016). Furthermore, delta-V values of 5 km/s for Earth departure and 1.5 km/s for Mars capture and landing are employed in this analysis. This seemingly low Martian capture and landing delta-V value is the result of utilizing aerobraking, in conjunction with propulsive landing, and it is stated in Musk (2017) that "over 99% of [the] energy [is] removed aerodynamically". Additionally, for the trans-Mars injection orbit from LEO, a hyperbolic excess velocity of 6.49 km/s was computed from the delta-V provided and a LEO perigee altitude of 200 km was used. The Earth departure inclination is assumed to be between 5 and 7° above the ecliptic, so an average value of 6° was used in this analysis. The results for two-stage architectures are tabulated with and without OTVs for Earth and Moon centric refueling orbits and are listed in Table 2.6 below.

Table 2.6: Starship Mars Mission Refueling Results

SpaceX Starship Refueling Study Results											
Set Up	**Total Mission Mass per kg Payload**	**Primary Rocket Mass per kg Payload**	**Refueling Fuel Mass per kg Payload**	**Refueling Rocket Mass per kg Payload**	**Single Rocket Mass per kg Payload**	**Mass Savings (%)**	**Mass Savings Over LEO Case (%)**	**Optimal Orbit e (28.5° Inc, Rp = 200 km - Earth or 6.7° Inc, Rp = 50 km - Moon)**	**Uppermost Stage Launch Fill Fraction**	**Uppermost Stage Refueling Fill Fraction**	**Notes**
Earth Orbit Refueling	858.09	46.88	9.22	811.21	3681.30	429.01	n/a	0	1	0.98	Hits e = 0 bound limit. Method 2 is superior.
Earth Orbit Refueling w/ OTV	676.59	112.50	5.93	564.05	3681.30	544.10	126.83	0.52	1	0.45	Near/at OTV optimal zone
Lunar Orbit Refueling	113.70	98.94	7.13	14.76	3681.30	3237.80	754.71	0.99	1	0.58	Hits e = .99 bound limit
Lunar Orbit Refueling w/ OTV	111.14	98.94	7.13	12.20	3681.30	3312.33	772.08	0.99	1	0.58	Hits e = .99 bound limit

For the Isps and mass ratios used, the optimal Earth-centric refueling orbit (with a periapsis altitude of 200 km) is circular (e = 0) for the non-OTV case, and 0.52 for the OTV case. These cases represent 1.00 and 1.27 times less total mission architecture mass than the nominal LEO refueling case, respectively. These orbits are visualized in Figures 2.8a and 2.8b below, with the initial LEO, the Earth departure hyperbolic trajectory, and the ecliptic plotted for reference. As for the lunar refueling cases, the optimal refueling orbit eccentricity of 0.99 (with a periapsis altitude of 50 km) for both the non-OTV and OTV cases is again encountered, representing 7.55 and 7.72 times less total mission architecture mass than the nominal LEO refueling case, respectively. With this knowledge, it is clear that SpaceX should refuel their Starship vehicle in LEO to realize the greatest benefit from orbital refueling.

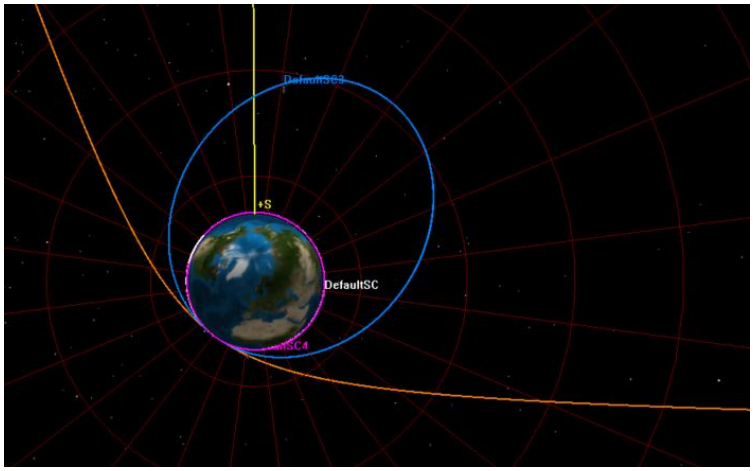

(a)

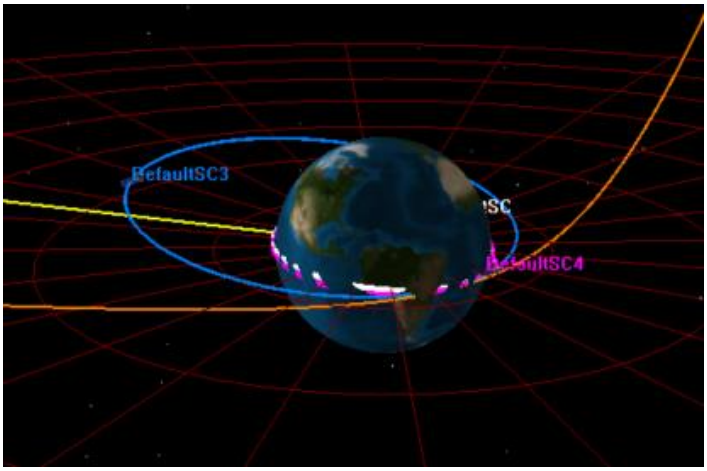

(b)

Figure 2.5: Starship Earth Refueling and Reference Orbits. White - Initial LEO. Purple – Non-OTV Case Optimal Refueling Orbit. Blue – OTV Case Optimal Refueling Orbit. Orange – Earth Departure Hyperbolic Orbit. Yellow – Direction of the Sun. Red Grid – Ecliptic Plane

Chapter 2.3: Chapter Review and Future Work

In this chapter, a method for investigating and quantifying optimal refueling orbits and resulting mission architecture mass savings has been presented. Two applicable cases where refueling can be utilized - the *Artemis 1* mission and the SpaceX Starship-Mars architectures - have been assessed to determine how optimally placed refueling orbits may benefit by reducing the overall mass of these missions.

Additionally, a parametric study was also conducted, demonstrating that orbital refueling can offer significant launch vehicle mass savings, potentially providing equivalent missions, while reducing overall mass by factors ranging from 1.4-7.3 when compared to the traditional single rocket architectures. Both two-stage rockets and SSTO launch vehicles were examined here for an example mission to Mars. One key takeaway from this study is that for a mission architecture utilizing similar primary and refueling rockets and launching from a common body, the optimal refueling orbit will occur where the primary launch vehicle utilizes all of its fuel-load and is then able to be refilled to 100% capacity. Another key takeaway is that orbital transfer vehicles utilizing efficient electric propulsion can prove very useful when transporting fuel depots to higher orbits. Furthermore, the greatest reduction in total mission architecture mass of all refueling architectures assessed in this study is found by utilizing a highly eccentric, lunar orbit to refill a primary rocket from Earth with fuel from the lunar surface. Last, it is shown that as the mass of a launch vehicle becomes larger, through either a reduction of vehicle performance parameters (e.g., decreasing Isp or mass ratio) or an increase in required delta-V. A larger mass savings is gained through utilizing orbital refueling, and the more orbital refueling becomes beneficial to reducing the overall architecture mass.

This study is intended to provide first-order estimates of potential launch vehicle mass

savings and optimal refueling orbits. Future improvements should account for scaling of the masses of launch vehicle structures and fuel mass. Accounting for this scaling is necessary as the structures utilized to contain the fuel will generally scale with the square of the launch vehicle radius, while fuel mass per volume will scale with the cube of the launch vehicle radius. Therefore, as a rocket increases in size, so too does its mass ratio, and the more efficient the vehicle becomes. Any future work should also account more thoroughly for gravity losses and aerodynamic drag when launching from the Earth. This study also does not account for differences in vehicle thrust to weight ratios stemming variations in rocket and stage sizings. Additionally, this paper found optimal orbits by performing a parameter sweep through all valid eccentricities. Therefore, a numerical optimization problem could be constructed, and could include orbit inclination as a parameter as well. Another improvement could be to account for the gravitational three-body problem of the spacecraft in cis-lunar space.

In conclusion, this analysis provides quantitative evidence to support the concept of orbital refueling to reduce overall mission mass when looking at the entire mission architecture. This analysis illustrates how on-orbit refueling could be game-changing, allowing smaller launch vehicles to play a role in transporting significantly greater payload masses than is currently thought possible.

Chapter 3: Assessment of Prediction and Efficiency Parameters for Cryogenic No-Vent Fill

Chapter 3.1: Motivation and Overview

The results presented in the previous chapter have shown the benefits of on-orbit refueling, including substantial mass savings. However, transferring fuel from a storage tank to a customer receiver tank is not as simple as it may seem. As more deep space missions utilize cryogenic fuels such as liquid hydrogen (LH_2) and liquid methane (LCH_4), fuel depots must be able to transfer cryogenic fuels reliably and automatically. Therefore, some technical goals of a well-designed cryogenic fuel depot and cryogenic fuel transfer method are: (1) to completely eliminate the possibility of venting liquid; (2) to minimize losses due to boil-off when the cold propellant comes in contact with the warm transfer line and customer receiver tank; and (3) to ensure high final fill fraction (usually >90%) at the end of transfer. Cryogenic fuels represent a unique problem to the fuel transfer process as these fuels, especially LH_2, are prone to boiling at modest wall temperatures, causing increases in pressure that can disrupt the no-vent fill transfer process.

A number of methods have been proposed to enable the successful refueling of a hot, empty customer receiver tank. One method introduced earlier is called the “chill and fill” method, which relies on the cooling capacity of the propellant itself to achieve successful transfer. This method works by injecting “charges” of cold fuel into the tank to allow for the fuel to absorb energy from the tank itself through boiling and convection heat transfer (Keefer and Hartwig 2016). After sufficient time to remove thermal energy from the tank has passed, the gas is vented, and the process is repeated until the tank walls have been cooled down to a certain

target temperature. Upon removing enough energy, a no-vent fill (NVF) can then be initiated, wherein fuel is transferred to the receiver tank with the vent valve closed to avoid venting liquid fuel overboard. Of course, the amount of fuel required to sufficiently cool the receiver tank will vary with the system parameters including cryogen type, tank metal, tank thickness, tank size, tank temperature, and more, but will generally be a fraction of the fuel mass required to fill the tank completely.

Predicting the target temperature required to initiate the fill is critical to mission success, and many system parameters such as tank mass, material, cryogen, and more can vary the target temperature. For real-world cases with non-uniform receiving tank temperatures, this target temperature could be compared with the average of sensor measurements if a receiving tank has multiple sensors. Precisely determining this target temperature is important. If fill is initiated too early, when the receiver tank is too warm, the pressure in the receiver tank can rise beyond the supply pressure, causing the pressure drop across the transfer interface to become zero (or even negative), terminating flow into the tank. At this point, the hot tank would continue to heat the injected fluid, causing the pressure to rise even further. Here, the only solution to reducing the pressure in the receiver tank to below that of the propellant supply tank would be to vent the receiving tank and dumping propellant into space. On the other hand, cooling the tank too much may lead to wasted fuel if the "chill and fill" method is employed, as the fill could have been initiated with a warmer tank.

To better understand what constitutes a successful non-vented transfer of fuel, it is instructive to examine typical pressure and fill level traces for NVF operation. Typical pressure response cases of a successful "chill and fill", and a failed "chill and fill" are plotted in Figure 3.1 below. In the figure, one can observe how the pressure in the tank spikes when the fill

begins; this is indicative of flashing and/or boiling that occurs when the cryogenic fluid removes the remaining residual thermal energy from the wall. At this point, the receiver tank pressure could potentially rise above the supply tank pressure, causing fuel flow into the tank to cease. To restore the proper pressure drop, one could vent the receiver tank. However, since the vent must always be closed to avoid dumping liquid overboard, the fill process fails. This describes what occurs in the failed fill in Figure 3.1. However, for a successful transfer, after the initial rapid pressure rise, the pressure reaches a maximum *below* the supply tank pressure, and then begins to drop. This is the portion of the fill process where the receiver tank pressure exceeds the fuel saturation pressure, cryogenic flashing stops, and the rate of condensation overtakes the rate of boiling in the tank. The receiver tank pressure now continues its trend of decreasing, until gas eventually becomes compressed by the rising liquid-vapor interface in the tank, near the end of fill, at around 80% capacity.

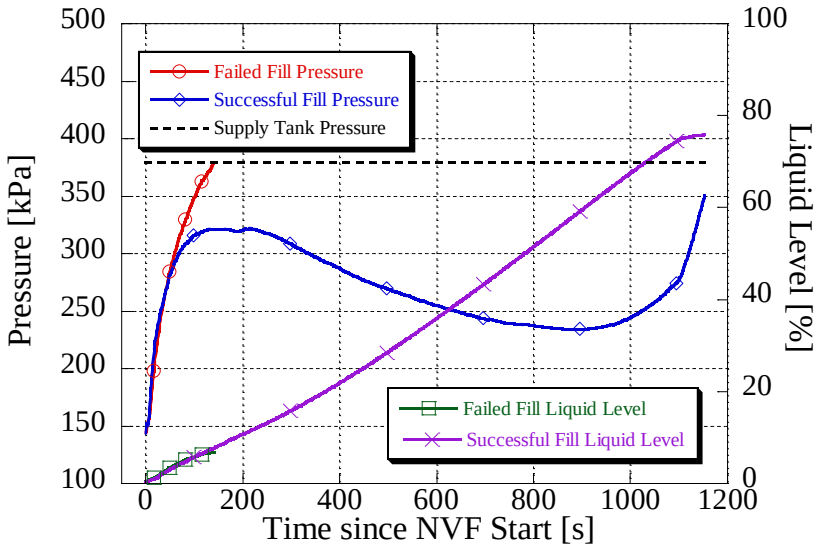

Figure 3.1: Pressure and Liquid Level Traces of Successful and Failed No-Vent Fill Tests from Hartwig et al. (2021)

Therefore, predicting the target temperature of the receiver tank is necessary for predicting a successful fill, and is the main goal of this paper. The outline of this chapter is as follows: First, a brief background into historical NVF and NVTO tests is presented. Then, the prediction parameter and an efficiency parameter are derived from first principles. Next, a parametric study is conducted to determine the relative importance of factors that affect the success of cryogenic NVF transfers. Finally, the prediction parameter is assessed against numerous historical tests over a wide range of fluids, injection methods, and tank geometries.

A brief summary of the historical NVF/NVTO tests is presented here. For a more thorough review of historical NVF and NVTO tests, the reader is referred to Hartwig et al. (2021). Note that in the historical literature, various injection methods are utilized, but can be generally referred to by the common categories that follow. A “top spray” is an injection method that utilizes a downward spray from the top of the tank, a “bottom spray” is an injection method that utilizes an upward spray from the bottom of the tank, a “spray bar” is an injection method that utilizes a long pipe through the middle of the tank and has many small orifices for even distribution of liquid, a “bottom diffuser” is an injection method that utilizes a diffuser at the bottom of the tank to fill the tank from the bottom, a “dip tube” is an injection method that utilizes a central pipe to transfer liquid to the bottom of the tank to fill in a similar method to the “bottom diffuser”, and an “upward pipe” is an injection method that utilizes a pipe at the bottom of the tank to direct liquid towards the top of the tank, and differs from the bottom spray by maintaining the liquid in a tight stream. The reader is referred to Hartwig et al. (2021) for further reading on this topic.

With these terms defined, a summary of the historical NVF/NVTO tests can be presented. Chato et al. (1990) conducted NVF tests using both LN_2 and LH_2 on a smaller 140-liter dewar.

Chato (1991) performed a series of LH_2 NVF experiments on a large 4960-liter tank with a top spray nozzle, and verified that NVF transfer is possible with well insulated, large tanks. Moran et al. (1991) then conducted over forty (40) NVF experiments with a 34-liter tank using multiple different injectors, including a top spray, an upward pipe, and a bottom diffuser. Chato and Sanabria (1991) then conducted a single tank chilldown and tank fill experiment on a large LH_2 tank, ultimately demonstrating the success of charge-hold-vent in conjunction with NVF. Moran and Nyland (1992) presented results of thirty-eight (38) NVF tests, including results for a spray bar. Moran and Nyland also examined the effect of the initial wall temperature, reporting many successful and failed tests. Chato et al. (1993) conducted twenty-two (22) NVF tests and investigated the effect of inlet mass flow rate and inlet condition on the transfer process. However, Chato et al. (1993) utilized a constant mass flow rate into the receiver tank by constantly increasing the supply tank pressure, thereby always achieving successful fills. Additional tests were performed at NASA's Marshall Space Flight Center and reported in Flachbart et al. (2013). These were a series of NVTO LH_2 tests of the Multi-purpose hydrogen testbed (MHTB) tank under the Advanced Shuttle Upper Stage (ASUS) test program. The tank used in this experiment was a large, thick-walled, roughly 18 m^3 domed cylinder, representative of actual, large space-flight tanks. Test number fourteen (14) was able to achieve a successful NVF after a vented-fill/chill was performed, filling the tank to 90%. In 2016, Kim et al. performed sixteen (16) parametric NVF tests on a small cylindrical tank using a methane surrogate fluid, tetrafluoromethane, or also known as LCF4 or R14. Their experimental setup utilized a nozzle at the top of the tank for the injection method. Initial tank wall temperature, incoming liquid temperature, mass flow rate, and supply tank pressure were all varied. A parametric study of these parameters was done as well, and it was found that: (1) the initial

receiver tank wall temperature and the incoming fluid temperature are closely related to the maximum pressure inside the receiver tank; (2) the supply tank pressure is closely related to the ability to condense vapor inside the receiver tank; (3) the mass flow rate only affects the duration of the fuel transfer process if the NVF is successful and manages to achieve a greater than 90% final fill level.

The most recent set of experiments was conducted on the CRYogenic Orbital Testbed Experiment (CRYOTE) tank. Johnson et al. (2015) conducted the first set of tests using CRYOTE, and thus was deemed CRYOTE 1. CRYOTE 1 completed one successful NVF transfer. Although the NVF procedure was not optimized in this experiment, a NVTO was also demonstrated, allowing for later analysis of the data for subsequent validation of various thermal models. The CRYOTE-2 tests consisted of more than fifty-three (53) tests demonstrating NVF and NVTO, varying many parameters such as injector type, supply tank pressure, initial fill level, and initial tank temperature (Hartwig et al. 2021). In summary, 158 NVF/NVTO tests can be compared against the efficiency parameter (defined in the next section), and have been performed with multiple different tanks, different injectors, and three cryogens (LH_2, LN_2, and LCF_4) over a wide range of thermodynamic conditions. These tests provide a robust set of data against which to apply and evaluate the target temperature computation method detailed subsequently, and stems from a control-volume energy balance analysis. Note here that the target temperature is also referred to as the “prediction parameter”.

It should be acknowledged here that the idea of utilizing an energy balance to derive the NVF/NVTO prediction parameter is inspired from the work presented in Kim et al. (2016). In their paper, Kim et al. proposed the use of a non-dimensional map to find the initial condition to achieve the desired final fill fraction below the desired final tank pressure. The prediction and

efficiency parameters in this paper aims to improve upon the work from Kim et al. (2016), in that they consider parasitic heat leak as well as initial liquid levels in the tank to permit calculations for both NVF and NVTO. The following section derives the parameter and accounts for heat leak and initial liquid levels in the tank, and is necessary to allow for the computations of the prediction and efficiency parameters for real-world cases. For example, an uninsulated receiver tank with some fuel remaining may arrive at a depot for refueling, so being able to accurately predict when fuel transfer will be successful is paramount for transferring fuel efficiently and successfully.

Chapter 3.2: Prediction and Efficiency Parameter Derivations, Applications, and Significances

The development of a prediction parameter stems from the desire to determine the warmest temperature at which a successful cryogenic NVF or NVTO could be initiated using a simple straightforward calculation, without having to run computationally expensive models. This maximum theoretical initial tank temperature is based on an energy balance of the tank metal, the incoming fluid into the tank, the final fluid in the tank, and any initial liquid or gas that may be present in the tank. The maximum theoretical initial tank temperature could therefore also be called the "ideal" initial tank temperature since it is the highest possible temperature of the tank where a successful NVF could occur.

The energy balance equation derivation can be seen in Equations 3.1 through 3.7, using the variables defined in the nomenclature section at the beginning of the thesis. From the 1st Law of Thermodynamics, the derivation begins by applying a control volume around the outside surface of the tank, including the inlet of the tank. The rate of change of the thermal energy of

the tank wall and any initial fluid in the tank is balanced by the environmental parasitic heat leak into the tank plus the incoming fluid enthalpy. Note that for this open system, the incoming fluid enthalpy is utilized to account for the flow work on system. This flow work specifically acts to transport the incoming fluid into the control volume, and therefore does work on the fluid contents in the control volume by acting like a piston. The resulting equation is represented below:

$$\frac{d(m_{fluid}u_{fluid})}{dt} + \frac{d(m_{tank}u_{tank})}{dt} = \dot{Q}_{Para} + \dot{m}_{inlet}h_{inlet} \tag{3.1}$$

The time differential dt can be multiplied to both sides of the equation, and time integrals are then applied to the incoming fluid and parasitic heat leak on the tank. The instantaneous energy balance on the control volume is now no longer instantaneous, but from an initial time to an end time, which can be defined as the beginning of NVF/NVTO and the end of NVF/NVTO, respectively:

$$\Delta(m_{fluid}u_{fluid}) + \Delta(m_{tank}u_{tank}) = \int_{t_i}^{t_f} \dot{Q}_{para}dt + \int_{t_i}^{t_f} \dot{m}_{inlet}h_{inlet}dt \tag{3.2}$$

Substituting the parasitic heat leak and instantaneous inlet mass flow rate with averaged versions, and substituting *dt* for *Δt*, with *Δt* being the elapsed time between NVF/NVTO start and NVF/NVTO end. Note that the specific inlet enthalpy h_{inlet} is not averaged because the temperature, pressure, and phase of the incoming fuel is considered constant.

$$\Delta(m_{fluid}u_{fluid}) + \Delta(m_{tank}u_{tank}) = \dot{Q}_{para,avg}\Delta t + \dot{m}_{inlet,avg}h_{inlet}\Delta t \tag{3.3}$$

Dividing the energies and masses into initial and final components, noting that for the tank, the mass does not change:

$$m_{fluid,final}u_{fluid,final} - m_{fluid,initial}u_{fluid,initial} + m_{tank}(u_{tank,final} - u_{tank,initial}) = \dot{Q}_{para,avg}\Delta t + \dot{m}_{inlet,avg}h_{inlet}\Delta t \quad (3.4)$$

The change in the internal energy of the tank metal is known, because it is simply the temperature integral of the specific heat of the tank metal as a function of temperature. Additionally, the mass of the fluid coming into the tank is simply the final mass in the tank minus the initial mass in the tank, because fluid is only coming in through the inlet, with none leaving the tank. Equation 3.4 becomes:

$$m_{fluid,final}u_{fluid,final} - m_{fluid,initial}u_{fluid,initial} + m_{tank}\int_{T_{initial}}^{T_{final}} C_{tank}dT = \dot{Q}_{para,avg}\Delta t + (m_{fluid,final} - m_{fluid,initial})h_{inlet} \quad (3.5)$$

Rearranging the terms yields:

$$m_{fluid,final}u_{fluid,final} - m_{fluid,initial}u_{fluid,initial} - (m_{fluid,final} - m_{fluid,initial})h_{inlet} = \dot{Q}_{para,avg}\Delta t - m_{tank}\int_{T_{initial}}^{T_{final}} C_{tank}dT \quad (3.6)$$

Finally, it is worthwhile to further divide the initial fluid energy term into its liquid and vapor components, since for NVTO it is possible to have a liquid be colder than the vapor, and in the case of low fill levels, the gas can be severely stratified. Such stratification could make the top portion of the gas warmer than its bottom layer, which is assumed to be in a saturation state with the top of the liquid. The significance in dividing the initial fluid energy term into its liquid and vapor components becomes clear in the case that one tries to base the initial fluid energy off of the pressure in the tank and by assuming that all the fluid in the tank is in a saturation state. Stratification would cause the measured pressure to be greater than the actual saturation pressure and doing so would cause the liquid to be estimated at a lower energy state than it is, potentially leading to significant inaccuracies when utilizing the equation later on. One solution is therefore to divide the initial fluid energy term into its liquid and vapor components and find the average

specific energy of the vapor, thereby accounting for inhomogeneity in the vapor due to stratification.

Conversely, the final fluid energy state can be assumed to be in a saturated state at the final tank pressure, as the fill level would be high enough, and enough time would have passed, to assume approximate thermodynamic equilibrium between the tank and the fluid. Therefore, with the final temperature of the tank equal to the final temperature of the fluid, no (or very little) stratification of the gas would occur, and the energy state of the fluid can be calculated as a saturated mixture:

$$m_{fluid,final}u_{fluid,final} - (m_{liquid,initial}u_{liquid,initial} + m_{vapor,initial}u_{vapor,initial}) - (m_{fluid,final} - m_{fluid,initial})h_{inlet} = \dot{Q}_{para,avg}\Delta t - m_{tank}\int_{T_{initial}}^{T_{final}} C_{tank}\,dT \quad (3.7)$$

Equation 3.7 states that the energy absorbed by the fluid is equal to the energy lost by the tank plus any parasitic heat leak into the tank. Consequently, Equation 3.7 can be used to determine the maximum allowable, or "ideal" initial tank wall temperature that permits a NVF at a desired final fill percentage and desired final temperature or pressure in the tank (assuming that the liquid and gas is in a saturated state, assuming the final temperature of the tank is equal to the final temperature of the fluid in the tank). Once the initial state of the fluid in the tank, the inlet specific enthalpy (based on inlet temperature and pressure), and the parasitic heat flux are all known or estimated, calculating the maximum, "ideal" initial tank temperature can be accomplished with a variety of numerical methods, such as the Bisection Method. $T_{initial}$ is this work's analog to the Kim et al. (2016) parameter, which is modified in this work to account for initial fill levels and parasitic heat.

Knowledge of the temperature dependent specific heat capacity of different tank metals is necessary in the calculation of maximum initial tank temperature. These metals include aluminum (Buyco et al., 1970), magnesium (Das, 2011), copper (Banerjee, 2005), stainless steel 304 (SS) (National Institute of Standards and Technology, 2020) (Bentz, 2007), titanium 6-4 (Titanium Metals Corporation, 1998), aluminum (Al) 5083 (National Institute of Standards and Technology, 2020), and Al-6061 (National Institute of Standards and Technology, 2020). Other alloys, such as Al-5056 (approximately 5% magnesium and 95% Al by mass) and Al 2219 (approximately 6.3% copper and 93.7% Al by mass) have a specific heat capacity vs. temperature relationship derived from the other material properties by utilizing Kopp's rule (Hurst et al. 1991).

Perhaps the most important characteristic of the "ideal" initial tank temperature is the subsequent ability to predict whether a NVF/NVTO will fail or succeed based on only the initial and desired final fluid conditions. If the fill process begins with the initial tank temperature at or above the maximum theoretical initial tank temperature, the fill is guaranteed to fail due to a rise in the tank pressure. This failure is due to the simple fact that the thermal inertia of the tank is too much for the desired change in the fluid energy to absorb. However, initiating a fill below the "ideal" maximum temperature does not guarantee a successful fill, and as will be shown, is because the fill process is path dependent, and thermal non-equilibrium during the fill is a main cause of this process dependency. Note that the model derived in this paper only considers equilibrium conditions between the fluid and tank metal, and so a higher-order, transient model would be needed to predict non-equilibrium conditions. The equations above do not account for the manner in which the fill is done, and only consider the initial and final states of the system. It is possible for the pressure in the receiver tank to deviate from the maximum pressure predicted

by the equations while the system is in non-equilibrium. Therefore, additional consideration must be taken with respect to this path dependency, and the injection method utilized for a given tank has perhaps the largest influence on the manner in which the fill is undertaken. Historical literature demonstrates that some injection systems are more efficient than others at keeping the pressure low due to cold liquid spraying into warm ullage as the tank is being filled. Indeed, looking back to Figure 3.1, the only variation between the failed and successful tests was the injector style used, demonstrating why selection of an effective injection method is so critical to a successful fill. More on the influence of the injector will be presented in the coming sections.

In any case, the only way to ensure a 100% success rate at filling would be to initiate fill with a tank chilled down at or below the saturation temperature of the incoming liquid. Between these two temperature bounds, the "ideal" maximum temperature and the fluid saturation temperature, is precisely where the following NVF/NVTO efficiency parameter can be useful in assessing performance:

$$\chi = \frac{T_{target,actual} - T_{sat}}{T_{ideal} - T_{sat}} \tag{3.8}$$

Hence, $T_{target,actual}$ is the experimentally determined maximum initial tank wall temperature for a given injector that achieves a successful fill. T_{ideal} is the "ideal" initial tank temperature calculated using Equation 3.7, and T_{sat} is the saturation temperature based on the maximum allowable final pressure in the tank, or the maximum allowable final temperature in the tank if that is the known value. Using Equation 3.8, it can be found that χ is equal to 1 at the "ideal" case, where the tank can successfully fill at the maximum theoretical initial tank temperature ($T_{target,actual} = T_{ideal}$), and that χ is equal to 0 in the worst case ($T_{target,actual} = T_{sat}$), where

the tank can only successfully fill at the desired final saturation temperature. Where this efficiency parameter will likely find its most effective use will be in comparing injectors for a specific tank with well-defined initial and desired final states.

Another way to define the efficiency parameter is to compare the ratio of energy lost by the tank with the maximum energy able to be absorbed by the fluid. In the "ideal" transfer, these energies equal one another:

$$\eta = \frac{\dot{Q}_{para,avg}\Delta t - m_{tank}\int_{T_{initial}}^{T_{final}} C_{tank}\,dT}{m_{fluid,final}u_{fluid,final} - (m_{liquid,initial}u_{liquid,initial} + m_{vapor,initial}u_{vapor,initial}) - (m_{fluid,final} - m_{fluid,initial})h_{inlet}} \tag{3.9}$$

One benefit to utilizing Equation 3.9 over Equation 3.8 is that it accounts for variations in inlet state and initial fill level that can occur during actual experiments. If these variations did not occur, the maximum energy able to be absorbed by the fluid would be a constant value across all tests. In Equation 3.8, the "ideal" initial tank temperature may not remain constant due to these slight variations, and analysis of test data later in this chapter shows this to be the case.

Note that the efficiency parameter is not a tool that quantifies the efficiencies of injectors alone, but rather a tool that quantifies the efficiencies of overall NVF/NVTO transfers, including the injection method and the tank geometry. To compare performances of various fill methods, all other test conditions need to be held constant. An additional complication to this efficiency parameter concerns the case of NVTOs, since in order to accurately calculate the maximum theoretical initial tank temperature, the initial energy states and masses of the liquid and gas in the tank would need to be known to an acceptable accuracy, which may lead to a requirement for more sensors needing to be placed in the receiver tank. This specific complication applies to the calculation of the prediction parameter as well. Nonetheless, now that the prediction parameter

and the efficiency parameter have been defined, and the entire NVF/NVTO database consolidated, the parameters can be compared against the historical database.

Chapter 3.3: Parametric Analysis of the Prediction Parameter

Here, a parametric study to determine the relative importance of factors that affect the success of cryogenic NVF is presented. The theoretical receiver tank used in this study is based on the CRYOTE tank introduced in an earlier section, with an inner diameter of 75 cm, a spherical shape, and a wall thickness and material that vary parametrically in the tests. The varied parameters include tank material, tank thickness (and therefore mass), working fluid, initial fill level, subcooled margin (inlet pressure minus saturation pressure based on inlet temperature), and desired final fill level. It is intended that each of the parameters have three or four different values/characteristics for variation, depending on the specific parameter. However, testing every combination of these parameters yields an unwieldy number of results. Consequently, a base case is defined from the parameters listed, and in bold in Table 3.1 below. Variations from the base case are used, reducing the number of results to a more manageable amount.

Table 3.1: Parametric Study Setup

Test Parameters for Assessing T ideal Change				
Test Parameters	1	2	3	4
Tank Material	**Al 2219**	304 SS	Ti 6-4	-
Tank Mass	Thin Wall	**Normal Wall**	Thick Wall	-
Fluid Type	**LN2**	LH2	LO2	LCH4
Initial Fill Level	Perfect Vaccum	**0 (Gas at 103.4 kPa)***	5%	10%
Pin - Psat(Tin)	68.9 kPa	**172.4 kPa**	344.7 kPa	-
Final Fill Level	90	**95**	97	-
Test Parameters Applied to a CRYOTE 1 Like Spherical Tank, ID of 75 cm				
Test Parameters	1	2	3	4
Tank Material	**Al 2219**	304 SS	Ti 6-4	-
Tank Mass/Thickness	.2 cm Thick	**.4 cm Thick**	.6 cm Thick	-
Fluid Type	**LN2**	LH2	LO2	LCH4
Initial Fill Level	Perfect Vacuum	**0 (Gas at 103.4 kPa)***	5%**	10%**
Pin - Psat(Tin)	68.9 kPa	**172.4 kPa**	344.7 kPa	-
Final Fill Level	90	**95**	97	-
*Gas in tank is near critical temperature for its fluid				
**Fill is in a saturated state 7K above the inlet temperature				

In each case with an initial fill level, the liquid is at the fill percentage shown and in a saturated state. The rest of the vapor in the tank is modeled at 7 K above the inlet temperature. A temperature of 7 K was selected to keep the tank pressure below the inlet pressure, while still having any initial fluid in the tank be warmer than the incoming fluid. Designating the initial fluid in the tank at a hotter temperature than the incoming fluid is crucial, since if the initial fluid temperature and the inlet fluid temperature were the same, varying the initial fill level would have no effect on the "ideal" initial tank temperature being calculated. Having an initial amount of liquid in the tank will decrease the amount of lower energy liquid able to be supplied by the inlet, and ultimately decreasing the amount of energy able to be absorbed from the tank by the fuel. In terms of Equation 3.7, having an initial amount of warm liquid in the tank will cause the left-hand side to decrease in magnitude, and therefore cause the right-hand side to decrease in magnitude as well, leading to a lower calculated initial tank temperature. Additionally, placing the initial tank fluid temperature higher than the inlet fluid temperature is more realistic, as tanks that have initial fill

levels likely may have had fluid sitting in the tank, warming up by absorbing heat from the surrounding tank. The requirement that any initial fluid be warmer than the incoming fluid also applies to the typical case in experiments where there is no fill level, with only warm cryogenic gas in the tank. Therefore, the base fill level case is a 0% full tank with 103.4 kPa cryogenic gas, just above the critical temperature of the cryogen.

Tables 3.2 and 3.3 below present these conditions to be used in the "ideal" initial tank temperature calculation (Equation 3.7), with Table 3.2 displaying the thermodynamic conditions in the tank, and Table 3.3 displaying the geometric setup of the tank being used in each calculation. REFPROP was utilized to find many of the parameters listed in Table 3.3 (Lemmon et al., 2010). Table 3.4 then presents the "ideal" initial tank temperature calculated for each parametric case using Equation 3.7. Higher temperatures imply that a NVF can commence earlier in the transfer process, thereby using less fuel to chill down the tank.

Table 3.2: Thermodynamic Conditions of each Test Case in the Parametric Study

Thermodynamic Conditions of Each Parametric Case						
Simulation Name	**Initial Fill Level**	**Initial Liquid Mass**	**Initial Gas Mass**	**Initial Fill Temp**	**Initial Fill Pressure**	**Fuel Type**
-	% Fill	kg	kg	K	kpa	Name
Base Case	0.00	0.00	0.62	126.00	103.42	NITROGEN
304 SS Tank Metal	0.00	0.00	0.62	126.00	103.42	NITROGEN
Ti 6-4 Tank Metal	0.00	0.00	0.62	126.00	103.42	NITROGEN
.2 cm Wall Thickness	0.00	0.00	0.62	126.00	103.42	NITROGEN
.6 cm Thickness	0.00	0.00	0.62	126.00	103.42	NITROGEN
LH2 Fuel	0.00	0.00	0.17	33.00	103.42	HYDROGEN
LO2 Fuel	0.00	0.00	0.57	154.00	103.42	OXYGEN
LCH4 Fuel	0.00	0.00	0.23	190.00	103.42	METHANE
Evacuated Tank	0.00	0.00	0.00	126.00	0.00	NITROGEN
5% Initial Fill	5.00	8.53	1.98	84.53	218.65	NITROGEN
10% Initial Fill	10.00	17.06	1.87	84.53	218.65	NITROGEN
Pin - Psat(Tin) = 68.9 kPa	0.00	0.00	0.62	126.00	103.42	NITROGEN
Pin - Psat(Tin) = 344.7 kPa	0.00	0.00	0.62	126.00	103.42	NITROGEN
Desired Final Fill Level = 90%	0.00	0.00	0.62	126.00	103.42	NITROGEN
Desired Final Fill Level = 97%	0.00	0.00	0.62	126.00	103.42	NITROGEN
Simulation Name	**Inlet Fuel Temp**	**Supply Tank Pressure**	**Pin-Psat(Tin)**	**Desired Final Fill**	**Desired Max Internal Temperature**	**Desired Max Final Pressure**
-	K	kpa	kpa	% Fill	K	kpa
Base Case	77.35	273.69	172.37	95.00	86.90	273.69
304 SS Tank Metal	77.35	273.69	172.37	95.00	86.90	273.69
Ti 6-4 Tank Metal	77.35	273.69	172.37	95.00	86.90	273.69
.2 cm Wall Thickness	77.35	273.69	172.37	95.00	86.90	273.69
.6 cm Thickness	77.35	273.69	172.37	95.00	86.90	273.69
LH2 Fuel	20.37	273.69	172.37	95.00	24.26	273.69
LO2 Fuel	90.19	273.69	172.37	95.00	100.90	273.69
LCH4 Fuel	111.67	273.69	172.37	95.00	125.28	273.69
Evacuated Tank	77.35	273.69	172.37	95.00	86.90	273.69
5% Initial Fill	77.35	273.69	172.37	95.00	86.90	273.69
10% Initial Fill	77.35	273.69	172.37	95.00	86.90	273.69
Pin - Psat(Tin) = 68.9 kPa	77.35	170.27	68.95	95.00	82.05	170.27
Pin - Psat(Tin) = 344.7 kPa	77.35	446.06	344.74	95.00	92.56	446.06
Desired Final Fill Level = 90%	77.35	273.69	172.37	90.00	86.90	273.69
Desired Final Fill Level = 97%	77.35	273.69	172.37	97.00	86.90	273.69

Table 3.3: Geometric Setup of each Test Case in the Parametric Study

Tank Geometric Setup for Parametric Cases					
Simulation Name	**Tank Volume**	**Tank Thickness**	**Tank Outer Surface Area**	**Tank Mass**	**Tank Material**
-	m^3	m	m^2	kg	-
Base Case	0.2209	0.004	1.81	20.29	2219 Aluminum
304 SS Tank Metal	0.2209	0.004	1.81	56.65	304 SS
Ti 6-4 Tank Metal	0.2209	0.004	1.81	31.58	Titanium 6-4
.2 cm Wall Thickness	0.2209	0.002	1.79	10.09	2219 Aluminum
.6 cm Thickness	0.2209	0.006	1.82	30.60	2219 Aluminum
LH2 Fuel	0.2209	0.004	1.81	20.29	2219 Aluminum
LO2 Fuel	0.2209	0.004	1.81	20.29	2219 Aluminum
LCH4 Fuel	0.2209	0.004	1.81	20.29	2219 Aluminum
Evacuated Tank	0.2209	0.004	1.81	20.29	2219 Aluminum
5% Initial Fill	0.2209	0.004	1.81	20.29	2219 Aluminum
10% Initial Fill	0.2209	0.004	1.81	20.29	2219 Aluminum
Pin - Psat(Tin) = 68.9 kPa	0.2209	0.004	1.81	20.29	2219 Aluminum
Pin - Psat(Tin) = 344.7 kPa	0.2209	0.004	1.81	20.29	2219 Aluminum
Desired Final Fill Level = 90%	0.2209	0.004	1.81	20.29	2219 Aluminum
Desired Final Fill Level = 97%	0.2209	0.004	1.81	20.29	2219 Aluminum

Table 3.4: Parametric Study Results

Parametric Analysis Results (K)			
Simulation Name	**Ideal Initial Tank Temperature (K)**	**Simulation Name**	**Ideal Initial Tank Temperature (K)**
Base Case*	318	Evacuated Tank	325
304 SS Tank Metal	233	5% Initial Fill	297
Ti 6-4 Tank Metal	301	10% Initial Fill	290
.2 cm Wall Thickness	483	Pin - Psat(Tin) = 68.9 kPa	216
.6 cm Thickness	255	Pin - Psat(Tin) = 344.7 kPa	416
LH2 Fuel	109	Desired Final Fill Level = 90%	309
LO2 Fuel	383	Desired Final Fill Level = 97%	321
LCH4 Fuel	387		
*The base case consists of all the bolded parameters in Table 3.1			

Beginning with the material of the tank, one can see that for the same tank size/thickness, use of Ti6-4 lowers the "ideal" initial tank temperature from 318 K to 301 K from the case of 2219Al, while 304SS lowers the "ideal" initial tank temperature from 318 K to 233 K. Even though 304SS has a lower specific heat capacity than 2219Al, the fact that 304SS is substantially more dense means that for the same tank thickness (and therefore volume) (see Table 3.3), the 304SS will hold considerably more thermal energy that needs to be removed by the incoming fluid.

Second, increasing the thickness of the tank metal will increase the mass of the tank. However, since the fluid in the tank can only absorb a certain amount of energy from the tank before the pressure in tank rises too high and the fuel transfer ends, the amount of energy per tank mass must decrease to account for the additional mass. Therefore, as tank thickness increases, the "ideal" initial tank temperature must decrease. This is indeed shown to be the case according to the results of the parametric study. Decreasing the tank thickness from 0.4 cm to 0.2 cm increases the "ideal" initial tank temperature from 318 K to 483 K, and increasing the tank thickness from 0.4 cm to 0.6 cm decreases the "ideal" initial tank temperature from 318 K to 255 K.

Third, the type of cryogen is varied between nitrogen, hydrogen, oxygen, and methane, with the resulting "ideal" initial tank temperatures being 318 K, 109 K, 383 K, and 387 K, respectively. This wide range in temperature is attributed to the fact that these fluids have very different physical properties, notably density and the specific heat under constant volume, or Cv. Utilizing the REFPROP program from Lemmon et al. (2010) and the specified inlet temperature and pressure, the density and the Cv for each cryogen can be computed. In the case of the cryogen density, the tank is filled with the same volume (95.0% tank volume), so varying the density will vary the mass, and therefore also vary the amount of energy that can be absorbed from the tank wall by the cryogen. Hydrogen has notably low density of 71.08 kg/m^3, while oxygen and nitrogen

have much greater densities of 1141.5 kg/m^3 and 806.55 kg/m^3, respectively. Therefore, the larger mass of LOX and LN_2 is able to absorb more energy and the tank walls can start at a higher energy state than with LH_2. As for the specific heats of these cryogens, if an assumption of constant volume for an injected blob of liquid is made, the Cv values can be compared. Again, by utilizing REFPROP, the Cv for the base case with LN_2 is 1084.5 J/kgK. For the LOx parametric case, the Cv is 929.22 J/kgK. For the LH2 parametric case, the Cv is 5662.7 J/kgK. Finally, for the LCH4 parametric case, the Cv is 2056.9 J/kgK. As can be observed here, LN2 and LOx have similar heat capacity values while the Cvs of LCH4 and LH2 are about two and five times greater, respectively. The difference in Cv values between LOx and LCH4 seems to make a great impact in the outcome of their similar "ideal" initial tank temperatures, as for the presented conditions, LOx is about 2.5 times denser than methane (1141.5 kg/m^3 for LOx and 422.51 kg/m^3 for LCH_4). As such, even though there is less methane in the tank to absorb heat, the fact that methane can store much more heat than LOx makes the cryogens about equal in the total amount of energy they can absorb. Overall, it can be concluded that the density and heat capacity of a cryogen both significantly impact the "ideal" initial tank temperature predicted. Additionally, it is notable that LH_2 exists at much lower temperatures than LOX and LCH_4, and factors into the "ideal" initial tank temperature being much lower for LH_2.

The fourth parameter is the initial state of the receiver tank. Beginning the transfer with a partially filled tank is shown to be detrimental to the ability to completely fill the tank, as demonstrated by the results in Table 3.4. By varying the fill between an evacuated state, a warm, gaseous (nominal) state, 5% liquid, and 10% liquid, distinctions between the resulting "ideal" initial tank temperatures can be seen to decrease with increasing fill level. This trend makes logical sense, since having a larger initial amount of warm fluid in the tank takes away from the total

amount of colder fluid being injected. Therefore, in order to account for the reduced ability of the fuel to absorb energy from the tank wall, the wall itself must be colder.

The fifth parameter to be varied in this study is the supply pressure (and thus subcooled margin) of the fluid coming into the tank. Varying the subcooled margin ($P_{in} - P_{sat}$) from 68.9 kPa to 344.7 kPa results in large changes in the "ideal" initial tank temperature. For the case of a 68.9 kPa subcooled margin, Table 3.4 predicts the "ideal" initial tank temperature to be 216 K. On the other hand, for the case of a 344.7 kPa subcooled margin, Table 3.4 predicts the "ideal" initial tank temperature to be 416 K, 200 K above the 68.9 kPa subcooled margin case, and 100 K above the base case with a subcooled margin of 172.4 kPa. This behavior can be explained by the fact that changing the supply tank pressure also causes the final maximum pressure to change, resulting in a warmer final equilibrium/saturation temperature. This allows the fluid to absorb more energy than previously allowable. Increasing the subcooled margin might therefore be one of the most significant parameters a transfer could utilize to ensure that a receiver tank successfully fills and may be one of the easiest to control.

The sixth and final parameter varied is the desired final fill fraction. Table 3.4 shows that altering this fraction between 90%, 95%, and 97% results in a general trend of increasing the "ideal" initial tank temperature. Increasing the desired final fill fraction increases the amount of mass of fluid injected which will therefore allow the fluid to absorb more energy from the tank wall, increasing the allowable initial energy state of the tank wall. However, it is notable that these differences in desired final fill fraction yielded relatively small differences in "ideal" initial tank temperatures as compared with other parameters, such as subcooled margin.

With the effects of varying these parameters in mind, one can envision that the most difficult scenario to fill a receiver tank would be one utilizing LH_2 to fill a thick-walled 304SS

tank that already has a substantial amount of warmer fluid in the tank. Additionally, the subcooled margin for which the LH_2 is transferred would be reduced in this scenario, and the desired final fill fraction would also be reduced. Conversely, the best-case scenario for fill might consist of LO_2 or LCH_4 being used to fill a thin-walled 2219Al tank that begins in an evacuated state. Additionally, the subcooled margin for which the LOX/LCH_4 is transferred would be as high as possible in this scenario, and the desired final fill fraction would be maximized.

Chapter 3.4: Application of the Prediction and Efficiency Parameters to Historical Data and Discussion

An assessment of the derived prediction parameter is achieved through calculation of the "ideal" initial tank temperature from Equation 3.7 and comparing with the actual initial tank temperature, and success or failure of the fill for each historical test. Pressure transducers and temperature sensors were used in the historical tests to measure the inlet state of the transferred fluid and the initial fluid state in the receiver tank, while the desired final fill level, tank material, and the maximum receiver tank pressure were either stated or could be derived. Parasitic heat load in each case was assumed to be zero, as some form of insulation was used throughout the historical tests assessed. As stated earlier, if the "ideal" initial tank temperature is lower than the actual initial tank temperature, the fill will always fail, since the tank is hotter than what is allowable via the 1st Law of Thermodynamics to achieve the desired end state. However, the converse of this statement, where fill should always succeed if the actual initial tank temperature is below the "ideal" initial tank temperature is not always true due to the fact that prediction parameter does not factor differences in heat transfer rates caused by different injection methods. The transient nature of the fill process allows for fills to fail depending on the complex heat

transfer processes taking place inside the tank at any given moment during the fill process. The fact that the historical data shows that the injector can affect whether an experiment succeeds is evidence enough for this behavior. It for this reason that the NVF/NVTO process can be deemed to be path dependent, with the manner in which the fill is conducted mattering just as much as the initial thermodynamic properties of the incoming fuel and receiver tank.

It is important to note that if the actual initial tank temperature is at or below the saturation temperature of the incoming fluid (such as could be the case in using a cryocooler), then heat transfer between the tank walls and the fluid would never cause the pressure to spike above the inlet pressure, and the fill should always succeed. Usually though, the range in temperature from the inlet fluid saturation temperature to the "ideal" initial tank temperature is on the order of 10s of K, which means that the transient nature of the fill process is usually a concern since the fuel can boil. Therefore, the injector plays an important role in determining NVF/NVTO success. The historical tests discussed do note the injector style used, and the "ideal" initial tank temperature is calculated using the variation of the tank metal's specific heat capacity with temperature, the tank properties, and the initial, final, and inlet fluid properties. With that being stated, the "ideal" initial tank temperature calculated for each test can be seen in Table 3.5 below. Injector style, actual initial tank temperature, desired final fill level, actual final fill level, whether the fill succeeded experimentally, and whether the actual outcome conforms to the theories are presented. Note that "< 0" and "> a number" in the "ideal" initial tank temperature calculation indicates the solution of Equation 3.7 lies outside the bounds of the metal-specific heat capacity and temperature data. In the case of "< 0", the inlet fluid state was at a higher energy state (for example, vapor or two-phase inlet flow) than allowable to reach the desired final fill equilibrium state, and it should never be possible to successfully fill. In the case

of “>” values, the bounds of the specific heat capacity and temperature data for the tank metal were exceeded. But since these bounds were significantly above 300K (the ambient temperature in most tests), these tests always successfully filled. Also note that the actual initial tank temperature column is an average value computed from various temperature sensors for each test series, and so some error could be introduced here, but will not affect the computation of the ideal initial tank temperature.

The prediction parameter derived here is validated against the historical data, as shown in Table 3.5 below. All of the historical test cases conform to the theory that if the “ideal” initial tank temperature is lower than the actual initial tank temperature, the fill should always fail. Additionally, the historical test cases conform to the second theory as well, in which fluid transfers can still fail even if the actual initial tank temperature is colder than the “ideal” initial tank temperature yet remaining warmer than the inlet saturation temperature.

Table 3.5: Prediction Parameter Calculation Results of Historical Tests

Results of the NVF/NVTO Parameter Applied to Historical Data								
Test Series	**Test Name**	**Injector Used**	**Desired Final Fill**	**Actual Final Fill Level**	**Successful?**	**Resulting Ideal T Tank**	**Initial Tank Temperature**	**In Agreement with Theory?**
Name	Name	Type	% Fill	%	Yes/No	K	K	Yes/No
CRYOTE 2	20141204	Shower Head (16 orifice)	95	93.45	Yes	295.29	199.80	Yes
CRYOTE 2	20141205.1	Shower Head (16 orifice)	95	3.48	No	154.82	252.49	Yes
CRYOTE 2	20141205.2	Shower Head (16 orifice)	95	6.59	No	192.98	234.03	Yes
CRYOTE 2	20141205.3	Shower Head (16 orifice)	95	95.05	Yes	296.79	224.12	Yes
CRYOTE 2	20141205.4	Shower Head (16 orifice)	95	86.70	Yes	297.11	224.57	Yes
CRYOTE 2	20141205.5	Shower Head (16 orifice)	95	86.51	Yes	294.59	199.19	Yes
CRYOTE 2	20141205.6	Shower Head (16 orifice)	95	6.77	No	209.47	238.53	Yes
CRYOTE 2	20141208	Shower Head (16 orifice)	95	2.92	No	<0	264.20	Yes
CRYOTE 2	20150116	Shower Head (8 orifice) and one spray nozzle (BETE TF10)	95	5.15	No	205.90	213.21	Yes
CRYOTE 2	20150120.1	Shower Head (8 orifice) and one spray nozzle (BETE TF10)	95	8.97	No	183.55	196.22	Yes
CRYOTE 2	20150120.2	Shower Head (8 orifice) and one spray nozzle (BETE TF10)	95	94.12	Yes	340.01	182.21	Yes
CRYOTE 2	20150121	Shower Head (8 orifice) and one spray nozzle (BETE TF10)	95	95.80	Yes	438.06	182.40	Yes
CRYOTE 2	20150122	Shower Head (8 orifice) and one spray nozzle (BETE TF10)	95	94.91	Yes	382.82	229.81	Yes
CRYOTE 2	20150123	Shower Head (8 orifice) and one spray nozzle (BETE TF10)	95	2.69	No	232.17	263.64	Yes
CRYOTE 2	20150126	Shower Head (8 orifice) and one spray nozzle (BETE TF10)	95	4.14	No	274.81	256.16	Yes
CRYOTE 2	20150127	Shower Head (8 orifice) and one spray nozzle (BETE TF10)	95	6.89	No	298.71	246.63	Yes
CRYOTE 2	20150128	Shower Head (8 orifice) and one spray nozzle (BETE TF10)	95	5.70	No	305.02	236.91	Yes
CRYOTE 2	20150212.1	Three spray nozzles (BETE TF10 and TF6 pointed down, TF8 up at lid)	95	1.36	No	<0	260.47	Yes
CRYOTE 2	20150212.2	Three spray nozzles (BETE TF10 and TF6 pointed down, TF8 up at lid)	95	1.94	No	196.58	262.46	Yes
CRYOTE 2	20150213	Three spray nozzles (BETE TF10 and TF6 pointed down, TF8 up at lid)	95	1.68	No	105.91	254.09	Yes
CRYOTE 2	20150218	Three spray nozzles (BETE TF10 and TF6 pointed down, TF8 up at lid)	95	94.56	Yes	>460	218.71	Yes
CRYOTE 2	20150219	Three spray nozzles (BETE TF10 and TF6 pointed down, TF8 up at lid)	95	3.46	No	181.19	246.98	Yes
CRYOTE 2	20150220	Three spray nozzles (BETE TF10 and TF6 pointed down, TF8 up at lid)	95	7.80	No	273.93	261.62	Yes
CRYOTE 2	20150227	Three spray nozzles (BETE TF10 and TF6 pointed down, TF8 up at lid)	95	95.04	Yes	>460	252.61	Yes
CRYOTE 2	20150302	Three spray nozzles (BETE TF10 and TF6 pointed down, TF8 up at lid)	95	2.78	No	151.72	249.02	Yes
CRYOTE 2	20150303	Three spray nozzles (BETE TF10 and TF6 pointed down, TF8 up at lid)	95	96.08	Yes	204.07	168.44	Yes
CRYOTE 2	20150304.1	Three spray nozzles (BETE TF10 and TF6 pointed down, TF8 up at lid)	95	5.04	No	222.63	246.27	Yes
CRYOTE 2	20150304.2	Three spray nozzles (BETE TF10 and TF6 pointed down, TF8 up at lid)	95	94.27	Yes	374.10	235.15	Yes
CRYOTE 2	20150309.1	Three spray nozzles (BETE TF10 and TF6 pointed down, TF8 up at lid)	95	4.70	No	226.96	254.45	Yes
CRYOTE 2	20150309.2	Three spray nozzles (BETE TF10 and TF6 pointed down, TF8 up at lid)	95	75.84	Yes	334.70	244.10	Yes
CRYOTE 2	20160914	Three spray nozzles (BETE TF10 and TF6 pointed down, TF8 up at lid)	95	1.13	No	227.64	242.89	Yes
CRYOTE 2	20160921	Three spray nozzles (BETE TF10 and TF6 pointed down, TF8 up at lid)	95	89.68	Yes	243.29	227.42	Yes
CRYOTE 2	20161004	Three spray nozzles (BETE TF10 and TF6 pointed down, TF8 up at lid)	95	2.34	No	191.75	192.78	Yes
CRYOTE 2	20161005	Three spray nozzles (BETE TF10 and TF6 pointed down, TF8 up at lid)	95	91.77	Yes	262.73	162.66	Yes
CRYOTE 2	20161006.1	Three spray nozzles (BETE TF10 and TF6 pointed down, TF8 up at lid)	95	94.05	Yes	257.01	165.33	Yes
CRYOTE 2	20161006.2	Three spray nozzles (BETE TF10 and TF6 pointed down, TF8 up at lid)	95	94.88	Yes	256.99	165.33	Yes
CRYOTE 2	20161006.3	Three spray nozzles (BETE TF10 and TF6 pointed down, TF8 up at lid)	95	6.87	No	217.48	172.56	Yes
CRYOTE 2	20161007	Three spray nozzles (BETE TF10 and TF6 pointed down, TF8 up at lid)	95	16.34	No	<0	170.40	Yes
CRYOTE 2	20161012	Three spray nozzles (BETE TF10 and TF6 pointed down, TF8 up at lid)	95	5.81	No	196.68	172.89	Yes
Chato 1990	N1	Top spray 120 deg cone	85	93.00	Yes	>800	123.89	Yes
Chato 1990	N2	Top spray 120 deg cone	85	98.00	Yes	>800	175.00	Yes
Chato 1990	N3	Top spray 120 deg cone	85	97.00	Yes	>800	185.00	Yes
Chato 1990	N4	Top spray 120 deg cone	85	90.00	Yes	485.97	97.80	Yes
Chato 1990	H1	Top spray 120 deg cone	85	45.00	No	162.22	61.70	Yes
Chato 1990	H2	Top spray 120 deg cone	85	91.00	Yes	237.59	85.00	Yes
Chato 1990	H3	Top spray 120 deg cone	85	39.00	No	42.53	41.70	Yes
Chato 1990	H4	Top spray 120 deg cone	85	86.00	Yes	237.70	60.60	Yes
Chato 1990	H5	Top spray 120 deg cone	85	14.00	No	131.35	50.00	Yes
Chato 1991	1	Top Spray	94	41.00	No	<0	48.33	Yes
Chato 1991	2	Bottom Spray	94	59.00	No	35.39	21.11	Yes
Chato 1991	3	Top Spray	94	53.00	No	115.04	17.22	Yes
Chato 1991	18	Bottom Spray	94	94.00	Yes	174.28	21.67	Yes
Chato 1991	19	Top Spray	94	94.00	Yes	144.86	104.44	Yes
Chato 1991	20	Top Spray	94	94.00	Yes	169.76	126.11	Yes
Chato 1991	21	Bottom Spray	94	94.00	Yes	175.84	101.67	Yes
Chato 1991	22	Bottom Spray	94	94.00	Yes	194.55	66.67	Yes
Chato 1991	23	Top Spray	94	94.00	Yes	151.89	70.00	Yes
Moran 1991	9088G	Bottom Diffuser	90	91.00	Yes	90.59	68.89	Yes
Moran 1991	9088H	Bottom Diffuser	90	77.00	No	107.89	67.78	Yes
Moran 1991	9080D	Bottom Diffuser	90	88.00	No	105.29	58.33	Yes
Moran 1991	9080B	Bottom Diffuser	90	79.00	No	104.51	52.22	Yes
Moran 1991	9088F	Bottom Diffuser	90	78.00	No	103.15	36.11	Yes
Moran 1991	9080C	Bottom Diffuser	90	67.00	No	100.40	35.00	Yes
Moran 1991	9081G	Bottom Diffuser	90	89.00	No	100.40	61.67	Yes
Moran 1991	9081H	Bottom Diffuser	90	82.00	No	98.35	87.22	Yes
Moran 1991	9081C	Bottom Diffuser	90	79.00	No	95.60	72.22	Yes
Moran 1991	9081D	Bottom Diffuser	90	82.00	No	93.72	63.33	Yes
Moran 1991	9075C	Bottom Diffuser	90	77.00	No	93.42	76.11	Yes
Moran 1991	9088D	Bottom Diffuser	90	82.00	No	93.15	86.11	Yes
Moran 1991	9088C	Bottom Diffuser	90	81.00	No	92.36	75.56	Yes
Moran 1991	9088B	Bottom Diffuser	90	76.00	No	89.37	48.33	Yes
Moran 1991	9081B	Bottom Diffuser	90	60.00	No	90.05	73.33	Yes
Moran 1991	9081F	Bottom Diffuser	90	29.00	No	80.50	85.56	Yes
Moran 1991	9094I	Upward Pipe	90	95.00	Yes	115.31	76.67	Yes
Moran 1991	9093F	Upward Pipe	90	95.00	Yes	112.23	56.67	Yes
Moran 1991	9093G	Upward Pipe	90	96.00	Yes	111.28	44.44	Yes
Moran 1991	9093E	Upward Pipe	90	87.00	No	103.44	62.78	Yes
Moran 1991	9094F	Upward Pipe	90	89.00	No	100.44	72.78	Yes
Moran 1991	9094G	Upward Pipe	90	94.00	Yes	96.86	55.00	Yes
Moran 1991	9094E	Upward Pipe	90	73.00	No	94.28	51.67	Yes
Moran 1991	9094H	Top Spray	90	96.00	Yes	114.34	47.78	Yes
Moran 1991	9093D	Top Spray	90	99.00	Yes	112.53	50.00	Yes
Moran 1991	9093C	Top Spray	90	97.00	Yes	110.27	55.56	Yes
Moran 1991	9093B	Top Spray	90	99.00	Yes	109.66	57.78	Yes
Moran 1991	9093A	Top Spray	90	98.00	Yes	109.49	53.33	Yes
Moran 1991	9081E	Top Spray	90	96.00	Yes	96.99	43.83	Yes
Moran 1991	9072B	Top Spray	90	98.00	Yes	97.46	53.61	Yes
Moran 1991	9075D	Top Spray	90	94.00	Yes	93.78	60.72	Yes
Moran 1991	9088E	Top Spray	90	99.00	Yes	101.30	41.11	Yes
Moran 1991	9080A	Top Spray	90	98.00	Yes	94.67	30.72	Yes
Moran 1991	9094D	Top Spray	90	88.00	No	95.63	54.44	Yes

Moran 1991	9094D	Top Spray	90	88.00	No	95.63	54.44	Yes
Moran 1991	9094C	Top Spray	90	91.00	Yes	95.68	55.56	Yes
Moran 1991	9094A	Top Spray	90	95.00	Yes	93.91	41.67	Yes
Moran 1991	9094B	Top Spray	90	90.00	Yes	93.74	29.44	Yes
Moran 1991	9072A	Top Spray	90	8.00	No	<0	71.33	Yes
Moran 1991	9088A	Top Spray	90	54.00	No	84.13	44.44	Yes
Moran 1991	9075B	Top Spray	90	67.00	No	76.17	50.72	Yes
Moran 1991	9081A	Top Spray	90	50.00	No	73.63	40.50	Yes
Moran 1991	9075A	Top Spray	90	10.00	No	<0	81.44	Yes
Moran 1992	91265a	Spray Bar - sb024	90	87.00	No	134.58	63.89	Yes
Moran 1992	91266a	Spray Bar - sb024	90	92.00	Yes	128.89	52.78	Yes
Moran 1992	91267a	Spray Bar - sb024	90	90.00	Yes	121.25	48.89	Yes
Moran 1992	91267b	Spray Bar - sb024	90	88.00	No	119.29	47.22	Yes
Moran 1992	91273c	Spray Bar - sb040	90	91.00	Yes	142.60	61.11	Yes
Moran 1992	91273b	Spray Bar - sb040	90	90.00	Yes	133.29	45.56	Yes
Moran 1992	91272c	Spray Bar - sb040	90	86.00	No	132.96	64.44	Yes
Moran 1992	91272a	Spray Bar - sb040	90	77.00	No	126.32	76.11	Yes
Moran 1992	91275	Spray Bar - sb040	90	68.00	No	106.33	69.44	Yes
Moran 1992	91274a	Spray Bar - sb040	90	86.00	No	98.88	36.67	Yes
Moran 1992	91281c	Spray Bar - sb052	90	90.00	Yes	144.55	60.56	Yes
Moran 1992	91280c	Spray Bar - sb052	90	90.00	Yes	141.92	76.67	Yes
Moran 1992	91279a	Spray Bar - sb052	90	92.00	Yes	138.67	42.78	Yes
Moran 1992	91281a	Spray Bar - sb052	90	79.00	No	108.23	71.11	Yes
Moran 1992	91280a	Spray Bar - sb052	90	81.00	No	104.57	71.67	Yes
Moran 1992	91282	Spray Bar - sb052	90	>82, test ended early	unk	127.07	52.22	Yes
Moran 1992	91274c	Spray Bar - sb040	90	91.00	Yes	137.81	36.11	Yes
Moran 1992	9153	Top Spray - ts4.3	90	93.00	Yes	129.51	45.56	Yes
Moran 1992	91274b	Top Spray - ts5.6	90	99.00	Yes	136.39	30.00	Yes
Moran 1992	91272b	Top Spray - ts5.6	90	97.00	Yes	123.90	32.22	Yes
Moran 1992	91273d	Top Spray - ts5.6	90	>82, test ended early	unk	113.68	29.44	Yes
Moran 1992	91273a	Top Spray - ts5.6	90	98.00	Yes	110.39	28.89	Yes
Moran 1992	91281d	Top Spray - ts14	90	94.00	Yes	138.49	36.11	Yes
Moran 1992	91280b	Top Spray - ts14	90	96.00	Yes	138.20	30.56	Yes
Moran 1992	91279b	Top Spray - ts14	90	95.00	Yes	139.21	50.00	Yes
Moran 1992	91280d	Top Spray - ts14	90	>80, test ended early	unk	131.40	42.22	Yes
Moran 1992	91281b	Top Spray - ts14	90	91.00	Yes	130.33	35.56	Yes
Moran 1992	91266b	Top Spray - ts27	90	97.00	Yes	143.25	70.56	Yes
Moran 1992	91267c	Top Spray - ts27	90	97.00	Yes	139.18	35.00	Yes
Moran 1992	91265b	Top Spray - ts27	90	96.00	Yes	139.19	61.67	Yes
Moran 1992	91266c	Top Spray - ts27	90	95.00	Yes	133.66	50.56	Yes
Moran 1992	91267d	Top Spray - ts27	90	90.00	Yes	120.00	36.11	Yes
Moran 1992	91258a	Top Spray - ts50	90	95.00	Yes	146.46	74.44	Yes
Moran 1992	91258b	Top Spray - ts50	90	96.00	Yes	142.53	75.56	Yes
Moran 1992	91254c	Top Spray - ts50	90	>79, test ended early	unk	141.51	80.56	Yes
Moran 1992	91254b	Top Spray - ts50	90	94.00	Yes	130.56	63.33	Yes
Moran 1992	91254a	Top Spray - ts50	90	90.00	Yes	109.16	56.11	Yes
Moran 1992	91259	Top Spray - ts50	90	96.00	Yes	104.99	66.67	Yes
Moran 1992	91282	Top Spray - ts14	90	>82, test ended early	unk	127.07	52.22	Yes
Moran 1992	91274c	Top Spray - ts5.6	90	91.00	Yes	137.81	36.11	Yes
CRYOTE 1	NVF Test	Shower Head (16 orifice)	95	100.00	Yes	426.46	91.7	Yes
Chato Sanabria 1991	Fill Portion	Top Spray and Bottom Jet	90	91.60	Yes	125.41	42.6	Yes
Kim 2016	Case 1	Top Orifice	90	95.00	Yes	708.90	180	Yes
Kim 2016	Case 2	Top Orifice	90	98.00	Yes	630.99	180	Yes
Kim 2016	Case 3	Top Orifice	90	98.00	Yes	422.98	180	Yes
Kim 2016	Case 4	Top Orifice	90	95.00	Yes	765.37	190	Yes
Kim 2016	Case 5	Top Orifice	90	95.00	Yes	>800	170	Yes
Kim 2016	Case 6	Top Orifice	90	95.00	Yes	765.37	200	Yes
Kim 2016	Case 7	Top Orifice	90	90.00	Yes	549.94	180	Yes
Kim 2016	Case 8	Top Orifice	90	95.00	Yes	342.95	180	Yes
Kim 2016	Case a	Top Orifice	90	50.00	No	290.86	160	Yes
Kim 2016	Case b	Top Orifice	90	17.00	No	196.26	160	Yes
Kim 2016	Case c	Top Orifice	90	18.00	No	196.26	160	Yes
Kim 2016	Case d	Top Orifice	90	4.30	No	275.43	180	Yes
Kim 2016	Case e	Top Orifice	90	69.00	No	228.56	170	Yes
Kim 2016	Case f	Top Orifice	90	33.00	No	219.96	180	Yes
Kim 2016	Case g	Top Orifice	90	3.40	No	228.56	180	Yes
Kim 2016	Case h	Top Orifice	90	10.00	No	170.32	160	Yes
Boeing ASUS	Test 14	Spray Bar	90	89.62	No	109.81	42.09	Yes

Recall that the prediction parameter can only be compared for different fills that utilize the same tank, and so, Figures 3.2 through 3.5 plot the outcomes of tests from Kim et al. (2016), Chato (1991), Moran et al. (1992), and CRYOTE 2, respectively. In each plot, the energy lost by the tank is plotted against the energy available to be absorbed by the fluid in the tank for each test, and the injector type is noted. A 1:1 line is plotted as well, which represents "ideal" performance, namely, that the energy to be lost by the tank exactly equals that of the fluid's capacity to absorb. If the data point lies above this line, it should always fail since the tank would

contain too much thermal energy for the fluid to absorb regardless of the transfer method. More efficient transfers occur closer to the line and still succeed, while less efficient transfers may still succeed further away from the line. The idea for and the usefulness of these plots follow similar plots presented in Kim et al. (2016).

Looking at Figure 3.2 below for Kim et al. (2016), just one type of injector, a top orifice nozzle, was utilized in this experiment. Notice how the tests become successful as more energy from the tank wall can be absorbed by the fluid coming into the tank. On the other hand, failed transfers occur closer to the line of "ideal" performance, where less energy from the wall is able to be absorbed by the fluid. As has been previously discussed, only successful fills should take place below the "ideal" performance line. However, due to the path-dependency of the fill process, failed transfers can occur in reality. As can be seen here and in later figures as well, no successful fills take place above the line of "ideal" performance. Again, this is because in an equilibrium condition, the fluid cannot absorb enough energy from the tank wall and still be below the desired final pressure.

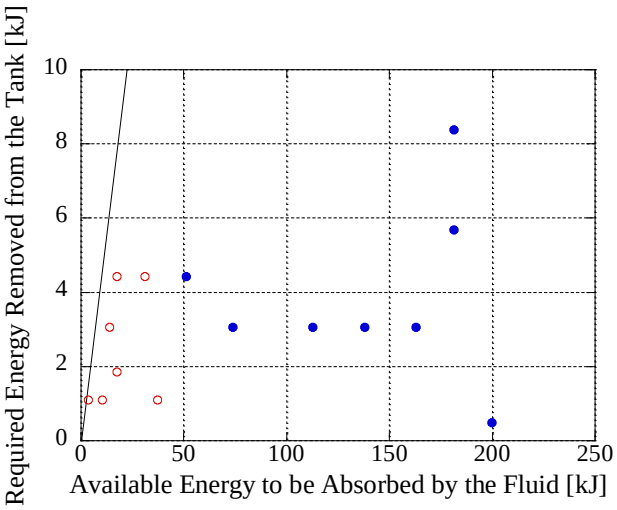

Figure 3.2: Energy Comparison Plot for Kim et al. (2016). Red open symbols represent failed fills while blue closed symbols represent successful fills. The black line is the line of "ideal" performance.

Moving on, for Chato (1991) Figure 3.3 below presents the fluid-tank wall energy comparison plot. In the experiment, the usage of the top spray injection method generally allowed for more efficient fills relative to the bottom spray injection method. This is due to the fact that the bottom spray injector becomes submerged during fill, essentially terminating the droplet spray into the ullage. More information on the injectors, including diagrams, can be found in Chato (1991).

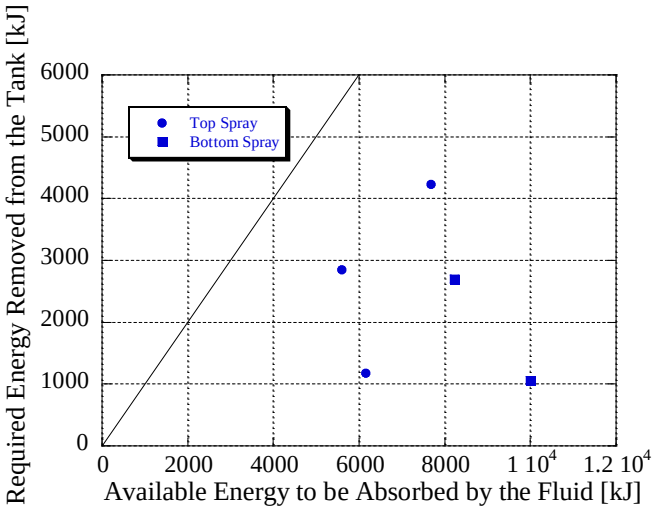

Figure 3.3: Energy Comparison Plot for Chato (1991). Red open symbols represent failed fills while blue closed symbols represent successful fills. The black line is the line of "ideal" performance.

For Moran et al. (1992), Figure 3.4 indicates that the various top spray injectors perform better than the spray bars, with top spray TS50 performing the best of all. However, no failed fill cases were recorded for the top spray tests. Note here that "SB" stands for spray bar, "TS" stands for top spray, and their subsequent numbers "indicate flow capacity in tenths of gallons per minute of water at a 10 psi pressure differential" (Moran, 1992). Therefore, higher numbers on the injectors indicate higher flow rates through the injector for a constant pressure difference. More information on the injectors, including figures, can be found in Moran et al. (1992). Unfortunately for this test series, no failed fills took place above the line of ideal performance and does not allow for the evaluation of the theory.

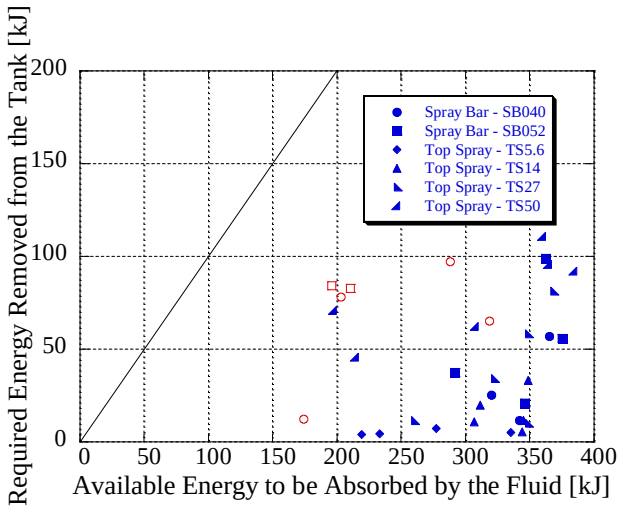

Figure 3.4: Energy Comparison Plot for Moran et al. (1992). Red open symbols represent failed fills while blue closed symbols represent successful fills. The black line is the line of "ideal" performance.

Finally, Figure 3.5 shows the energies involved for the CRYOTE test series. It is noteworthy that all tests lying above the line of ideal performance fail, agreeing with the theory presented earlier. Additionally, it can be seen that the second version of the three-spray nozzle injector achieved a fill close to "ideal" in one instance. Overall, it may seem that versions 1 and 2 of the three-spray nozzle design performed better than the other injectors. More information on the injectors can be found in Hartwig et al. (2021).

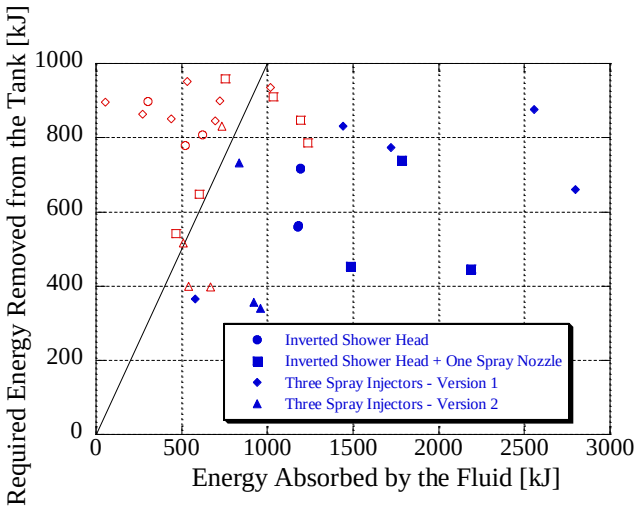

Figure 3.5: Energy Comparison Plot for the CRYOTE 2 Tests (Hartwig et al. 2021). Red open symbols represent failed fills while blue closed symbols represent successful fills. The black line is the line of "ideal" performance.

Overall, this work offers evidence that high-coverage sprays with a subcooled margin yield more efficient transfer processes, allowing tanks to be filled at higher initial energy states. However, other important factors such as droplet velocity, droplet size, droplet distribution, and the effect of gravity should be considered with respect to the injection method. One can further theorize that in order to obtain successful fills closer to the "ideal" initial tank temperature, high coverage sprays with high supply/inlet pressures should be used. This is consistent with test data from Hartwig et al. (2021) where injectors that maximize droplet heat and mass transfer and condensation heat transfer at the liquid-vapor interface tend to be better performing injectors. On the contrary, utilizing a fill method such as a dip tube with a low supply/inlet pressure might yield worse fill performance, and reduce NVF/NVTO transfer efficiency. However, more rigorous testing and higher-order transient models of the fill process could be used to ultimately confirm or refute this theory.

Chapter 3.5: Chapter Review and Future Work

In this chapter, a prediction parameter for assessing success or failure of cryogenic NVF has been applied to the consolidated database of 158 NVF experiments. A parametric study of the NVF/NVTO process was conducted, and the impacts of each parameter on the viability of a successful transfer were presented. The subcooled margin of the incoming liquid and the mass of the tank are the two most influential factors impacting NVF. Results show that the prediction parameter is always able to predict a failed transfer when the thermal energy required to be removed from the tank metal is greater than the transferred fluid can absorb. However, since cryogenic tank fill is dependent on the manner in which the fill is undertaken, the predictive parameter cannot be used to predict successful transfer in all cases. A higher order model that captures differences in performance of different fill methods is needed to further improve predictive performance. Nonetheless, the prediction parameter is a simple, easy-to-use, and useful, parameter that can be used for initial sizing and basic performance analysis, for both NVFs and NVTOs. Meanwhile, for datasets already in hand, the efficiency parameter can be used during post-processing to assess the performance of different injectors for the same tank.

Chapter 4: Tank-Injector Trajectory Analysis

Chapter 4.1: Motivation and Methods

As was concluded in Chapter 3, the pressure achieved during a no-vent fill process is path dependent, with factors such as tank geometry, material, injection method, cryogenic fuel, all impacting the maximum pressure experienced during the fill. Due to this path dependency a higher-order, transient model is necessary to accurately predict success or failure of a no-vent fill and is explored further in this section of the thesis.

This chapter therefore presents the results of a generalized tank-injector trajectory analysis subroutine applied to various historical no-vent fill tests and was done in support of a 1-g thermodynamic non-equilibrium nodal model being produced by the Reduced Gravity Cryogenic Transfer (RGCT) research group at NASA's Glenn Research Center (Brown, 2019). A reader might wonder how a 1-g model could be used to predict the fill outcomes in a 0-g space environment. It is hypothesized by the author that the 1-g case might actually be conservative in terms of the pressure response of the system, as the liquid is more likely to float freely in the tank system in 0-g, reducing contact with the tank wall (and therefore boiling) while also cooling the tank ullage to a greater extent. At the current time, however, this is just a hypothesis and rigorous 0-g and 1-g testing are still needed to support or refute this theory. Additionally, utilizing a 1-g refueling model makes the liquid-vapor interface much easier to predict, and so model design and solution computation can be greatly simplified.

The 1-g nodal model is designed to predict the resulting system thermodynamics of combinations of tank geometries, propellant type, and injection method, and knowing the

internal divisions of liquid, vapor, and two-phase mixture in the tank is paramount to predicting the resulting thermodynamic response of the system. Specifically, the nodal model works by dividing the receiver tank into the following six sections, where applicable: (1) a liquid node consisting of just the liquid propellant at the bottom of the tank; (2) a vapor node consisting of just the vaporized propellant and any spray above the liquid in the tank; (3) a liquid-vapor interfacial node for tracking the current saturation state of the overall propellant; (4) a liquid-wall node consisting of the tank metal currently adjacent to liquid propellant; (5) a vapor-wall node consisting of the tank metal currently adjacent to vaporized propellant; and (6) a two-phase-wall node consisting of the tank metal currently exposed to spray from the injector. From this point, heat and propellant mass transfer between the nodes is calculated based on the current nodal properties.

In accordance with this model development effort, a generalized trajectory analysis subroutine for any combination of tank geometry and injection method/size was required for supporting the model and determines necessary geometric properties of fuel injector-tank pairs while accounting for variation in the tank fill fraction. Therefore, these geometric properties can be assessed from 0 to 100% of liquid fill. As far as the specific output of this trajectory subroutine was concerned, the goal of this analysis was that for a given tank geometry, fill level, and injection method, the following parameters are calculated and output from the program:

1. The height of the liquid-vapor interface in the tank
2. Nodal surface areas with the wall and the liquid-vapor interface surface area
3. The average distance spray travels
4. The fraction of spray that hits the wall and the fraction of the spray that goes directly into the liquid node

5. The conduction areas and conduction lengths in the wall between the different nodes
6. The average angle to the wall at which spray impacts

The subroutine applies for any combination and desired size of the following tank geometries and injector types. For tank geometry, a user can select between a spherical tank, a spheroidal tank, a cylindrical tank, and a domed cylindrical tank. For injection type, the user can select between a bottom fill/dip tube, a top spray, a bottom spray, a spray bar, and a bottom jet. Note that in each combination, the injector is centrally located in each tank geometry and sprays evenly in all resulting directions. For example, a top spray injector paired with each tank type will appear similar to the following image, with the tanks, in order from left to right, being a domed cylindrical tank, a spherical tank, a spheroidal tank, and a cylindrical tank.

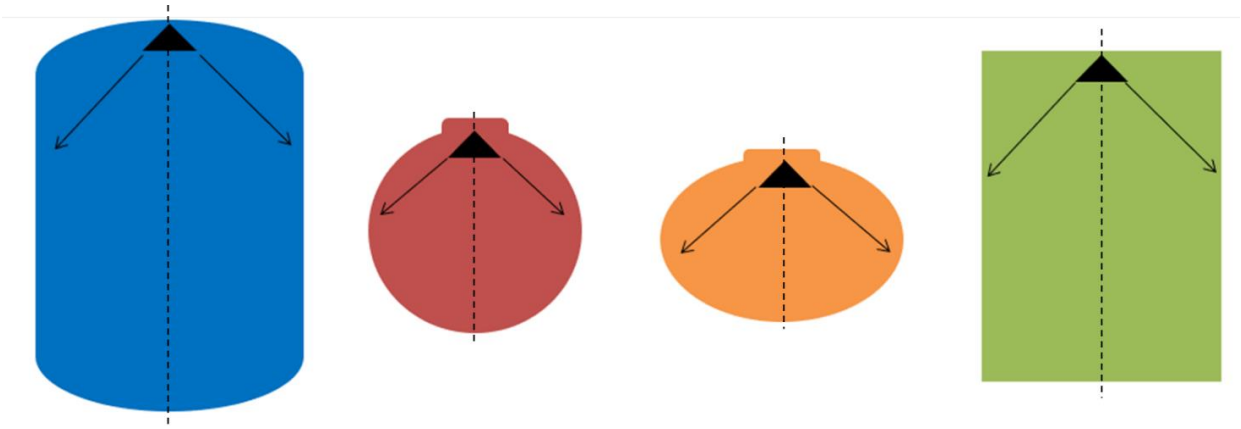

Figure 4.1: Example of a Top-Spray Injector Paired with Different Tank Geometries

After selection of tank geometry, injection method and sizes, the subroutine calculates the required parameters by making use of an axisymmetric assumption along the central axis of the injector, as shown in Figure 4.1. This assumption allows for the program to compute some of the necessary parameters, such as spray impact angle, in a 2-dimensional representation of the tank-injector combination. Additionally, it is assumed that the flow is moving quickly enough that

gravity (1-g) does not affect the resulting trajectory in a significant manner. Of course, this approach would be used with any 0-g fill as well. Due to the large number of combinations possible, the trajectory analysis subroutine is written as a collection of MATLAB scripts, with each script being an injection method type and tank geometry type with specific size parameters. Note that for the bottom jet injection methods, an additional parameter, the estimated average inlet mass flow rate, is required to determine the resulting jet velocity and height in the tank, with the average inlet fluid density and the jet orifice size being required as well.

For the sake of brevity, this chapter in the thesis only presents plots of the height of the liquid-vapor interface in the tank and the nodal surface areas with the wall and the liquid-vapor interface surface area as functions of liquid level for the various historical tests. These outputs are the most significant to the model, since they determine where the nodes are and how they interact with the rest of the model. For the remainder of this section, the different nodal areas as functions of liquid level are calculated for each historical test, specifically calculating the surface areas between the wall and liquid, the wall and the gas, the wall and the spray, and the wall and any potential spray runoff. As an accuracy verification, these wall surface areas are added together and should therefore always result in the total internal surface area of the tank, remaining constant across all liquid levels. The liquid-vapor interfacial area as a function of liquid level is also plotted, but does not contribute to the total internal wall surface area. Additionally, the height of the liquid-vapor interface above the bottom of the tank is plotted to demonstrate the effect of different tank shapes on liquid distribution in the tank.

Chapter 4.2: Model Application to the Tank-Injector Configuration in Chato et al. (1990)

Chato et al. (1990) utilizes a domed cylinder tank geometry with a top spray injector. The injector provides spray into the tank in a 120-degree arc, and becomes covered by liquid at roughly 90% of fill. Figure 4.2 below shows the liquid height from the bottom of the tank as a function of liquid level, and the influences of the different tank portions can be seen. In Figure 4.3 below, from 0 to roughly 10%, and from roughly 90 to 100% full, the wall-liquid surface area increase is determined by the domed portions of the tank. Between the domed ends the wall-liquid surface area increases linearly, reflecting the impact of the cylindrical portion of the tank. The wall-gas surface area is initially constant, but once the liquid-vapor interface reaches the edge of where the spray hits the wall, it begins decreasing linearly and then parabolically, again reflecting the influence of the cylindrical and domed portions of the tank. The wall surface area impacted by spray goes to zero around 60% liquid fill level, with the wall-gas node beginning its decrease at this point. There is no potential for spray runoff in the instance of a top-spray injector, so its surface area value is constantly zero. Finally, the liquid vapor interfacial area initially increases parabolically in the bottom dome, remains constant in the cylindrical portion, and finally decreases parabolically in the top dome.

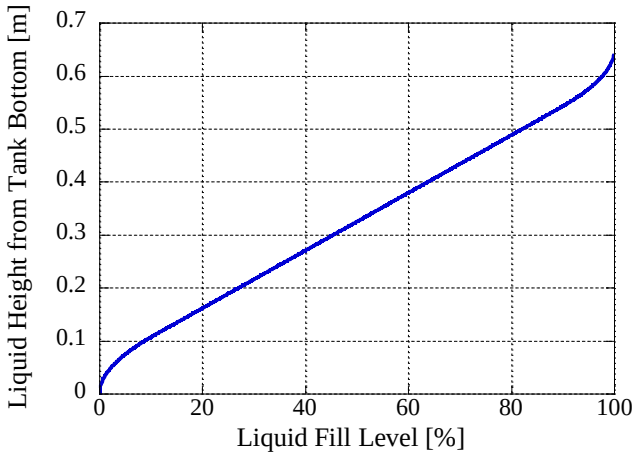

Figure 4.2: Liquid-Vapor Interface Height above Tank Bottom in Chato et al. (1990)

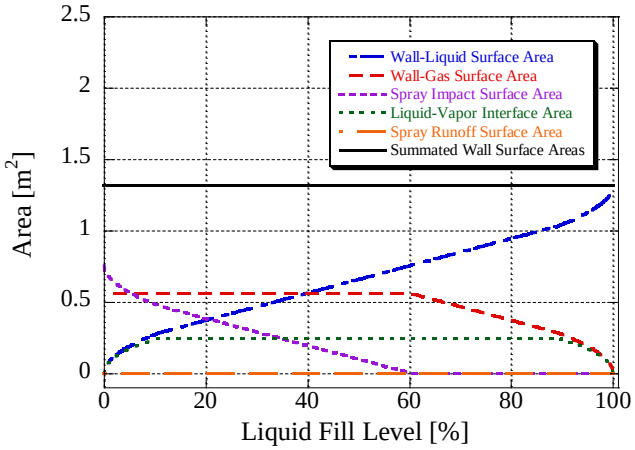

Figure 4.3: Internal Surface Areas of Interest in Chato et al. (1990)

Chapter 4.3: Model Application to the Tank-Injector Configuration in Chato et al. (1991)

Chato et al. (1991) utilizes an oblate spheroid tank with a bottom spray and a top spray. Figure 4.4 below shows the liquid-vapor interface height as a function of liquid level, demonstrating that as the liquid level rises, the height of the liquid-vapor interface is constantly changing, never reaching a period of linearity as seen in the cylinder. This figure applies to both the top and bottom spray since the injector does not influence the height of the liquid-vapor interface.

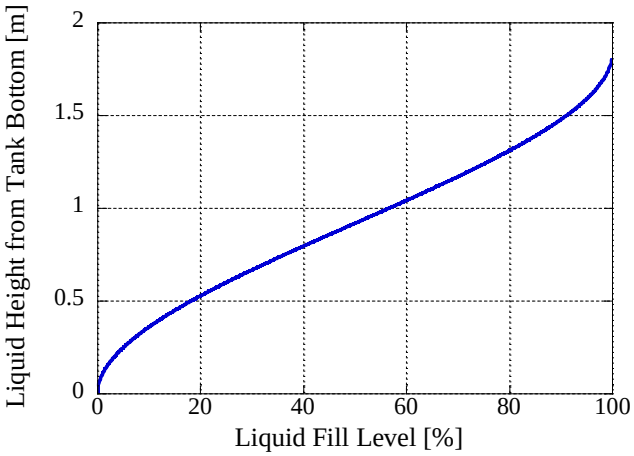

Figure 4.4: Liquid-Vapor Interface Height above Tank Bottom in Chato et al. (1991)

The bottom spray sits near the bottom of the tank, spraying in a 120-degree cone. It can be seen in Figure 4.5 below that once the injector becomes covered in liquid, the spray runoff and impact wall areas drop to zero, with the wall-gas surface area jumping to take their place.

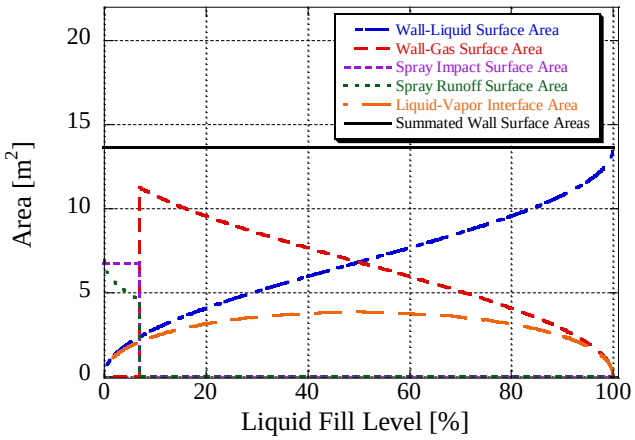

Figure 4.5: Internal Surface Areas of Interest for the Bottom-Spray in Chato et al. (1991)

The top-spray in Chato et al. (1991) shoots spray in nearly all directions at the top of the tank, essentially hitting all exposed wall with spray. As can be seen in Figure 4.6 below, only liquid and spray split the tank wall surface area, but once the injector becomes covered around 90% fill, the gas-wall surface area suddenly takes the place of the spray impact-wall surface area.

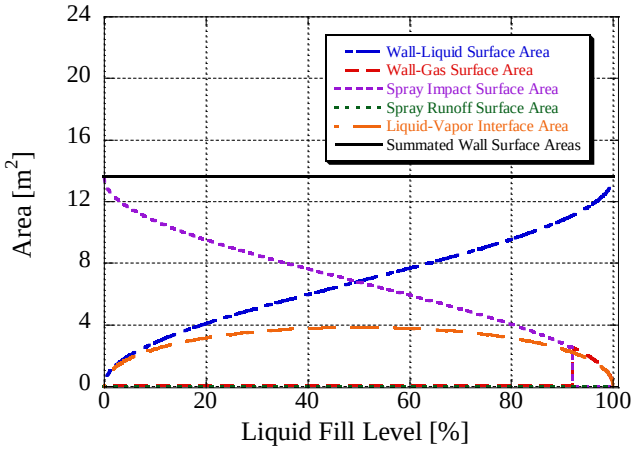

Figure 4.6: Internal Surface Areas of Interest for the Top-Spray in Chato et al. (1991)

Chapter 4.4: Model Application to the Tank-Injector Configuration in Chato and Sanabria (1991)

Chato and Sanabria (1991) use the same oblate spheroid tank used in Chato et al. (1991), but also employ a combination of the top spray and bottom jet injector types, with the top spray sitting near the top of the spray and the bottom jet sitting near the bottom of the tank. Figure 4.7 below shows the liquid-vapor interface height as a function of liquid level and is the same as in Chato et al. (1991). Figure 4.8 below plots the various surface areas with liquid level in the tank. Notice that as the bottom jet almost makes no difference in the areas plot. This is because the top spray is the same as in Chato et al. (1991), spraying in nearly all directions, so the top spray already covers the areas impacted by the bottom jet.

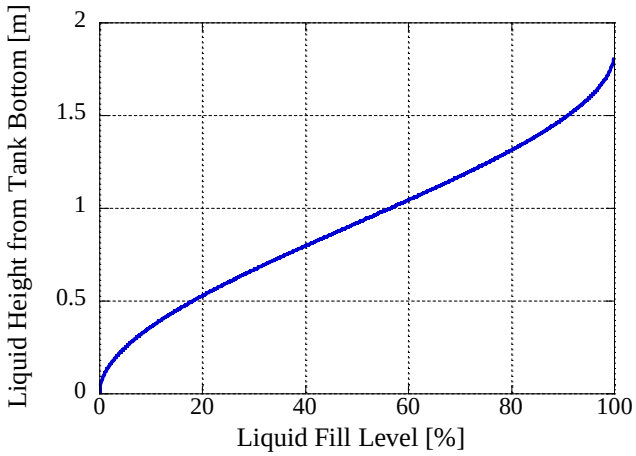

Figure 4.7: Liquid-Vapor Interface Height above Tank Bottom in Chato and Sanabria (1991)

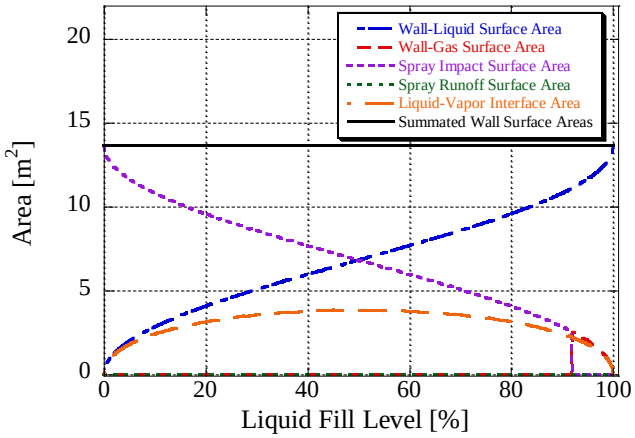

Figure 4.8: Internal Surface Areas of Interest in Chato and Sanabria (1991)

Chapter 4.5: Model Application to the Tank-Injector Configuration in Moran et al. (1991)

Moran et al. (1991) utilizes a domed cylinder tank with dip-tube, top-spray and bottom-jet injectors. Figure 4.9 below shows the liquid-vapor interface height as a function of liquid level and is the same in all three injector cases. Figures 4.10 through 4.12 present the internal surface areas of interest for each injector case. Notice how the bottom jet injector can no longer

hit the top of the tank with spray when the tank is around half full.

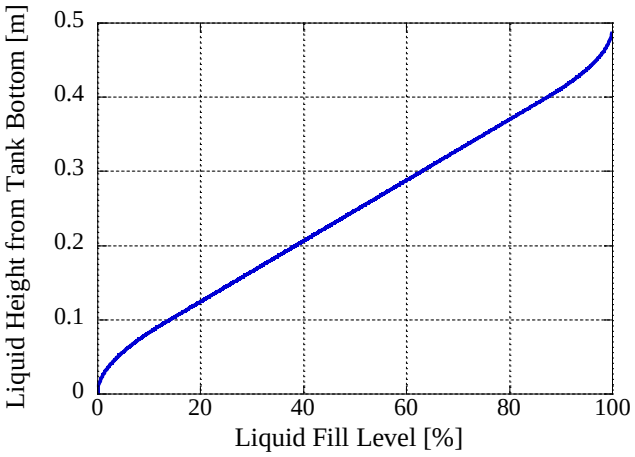

Figure 4.9: Liquid-Vapor Interface Height above Tank Bottom in Moran et al. (1991)

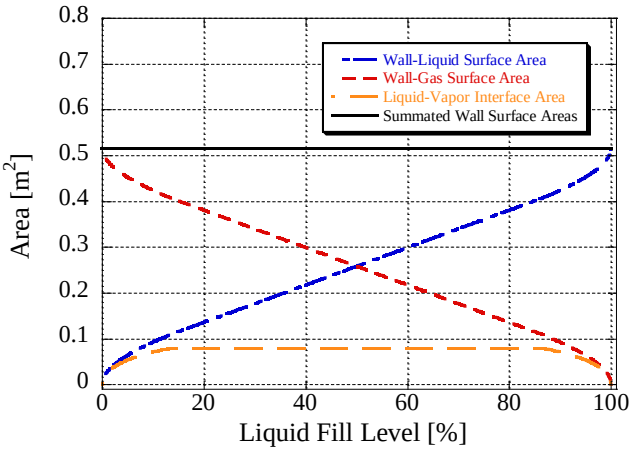

Figure 4.10: Internal Surface Areas of Interest for the Dip Tube in Moran et al. (1991)

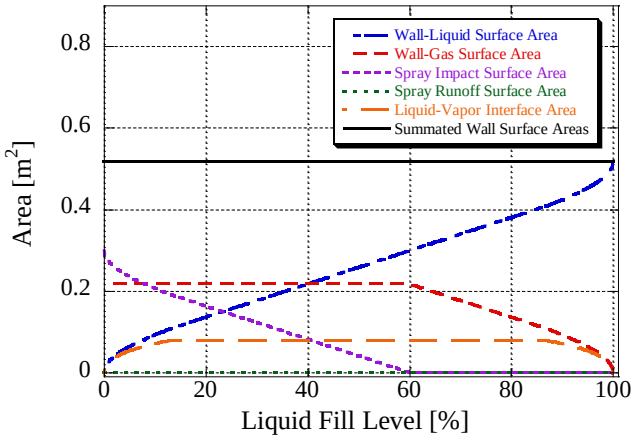

Figure 4.11: Internal Surface Areas of Interest for the Top Spray in Moran et al. (1991)

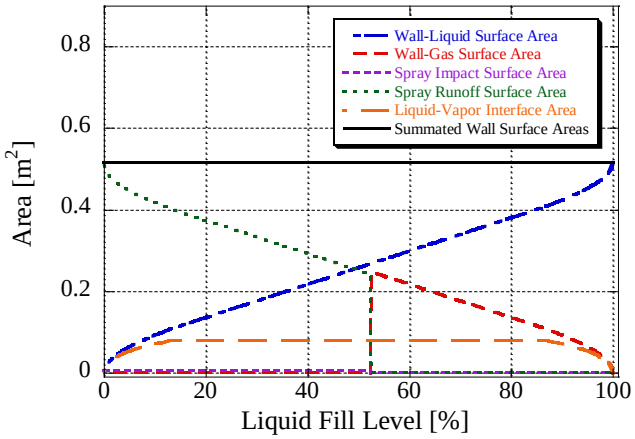

Figure 4.12: Internal Surface Areas of Interest for the Bottom Jet in Moran et al. (1991)

Chapter 4.6: Model Application to the Tank-Injector Configuration in Moran et al. (1992)

Just like Moran et al. (1991), Moran et al. (1992) utilizes a domed cylinder tank with three different spray-bar injectors and five top-spray injectors. However, the only difference among these injectors is their orifice sizes, so the trajectories are about the same across the spray bars and across the top sprays. Figure 4.13 below shows the liquid-vapor interface height as a

function of liquid level and is the same in all three injector cases. Figures 4.14 and 4.15 present the internal surface areas of interest in each injector case. The spray bar runs almost the entire length of the tank, so the spray is never fully submerged, and they can always cover the entire exposed portion of the tank wall.

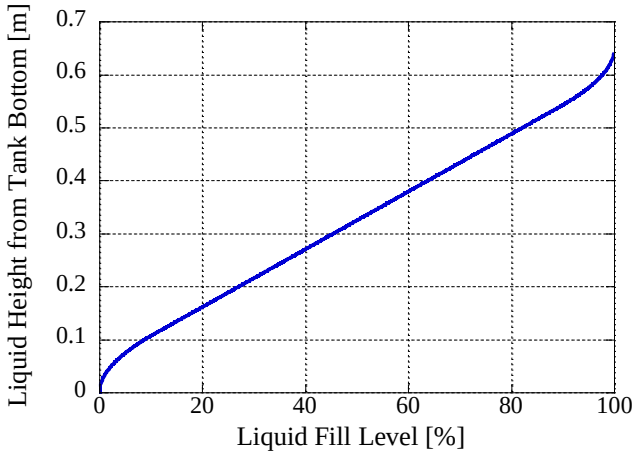

Figure 4.13: Liquid-Vapor Interface Height above Tank Bottom in Moran et al. (1992)

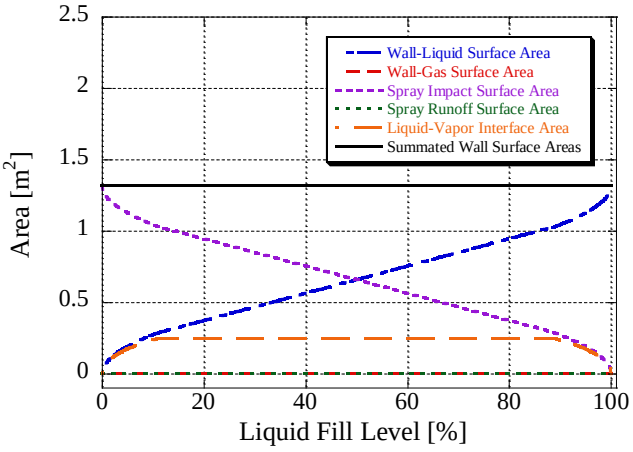

Figure 4.14: Internal Surface Areas of Interest for the Spray Bars in Moran et al. (1992)

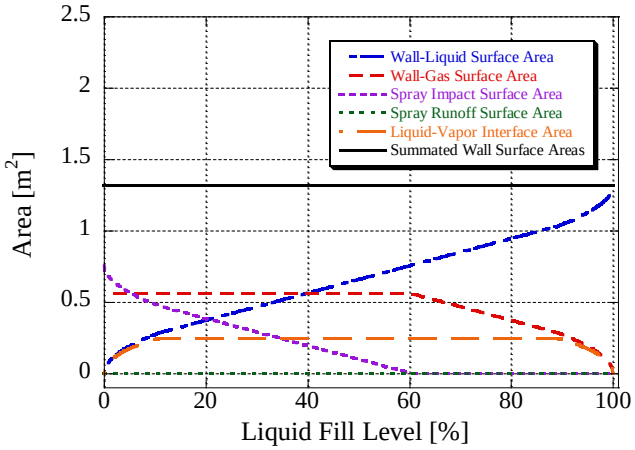

Figure 4.15: Internal Surface Areas of Interest for the Top Sprays in Moran et al. (1992)

Chapter 4.7: Model Application to the Tank-Injector Configuration in Chato et al. (1993)

Chato et al. (1993) utilizes another oblate spheroid tank with a spray bar and a bottom jet. From the experimentally determined mass flow rate it was determined that the velocity of the jet is always too low to hit the wall. Therefore, the bottom jet acts like a dip tube in this case. Additionally, the spray bar sits a bit below the top of the tank, always leaving a small area of tank wall unaffected by spray. Figure 4.16 below shows the liquid-vapor interface height as a function of liquid level and is the same in both injector cases. Figures 4.17 and 4.18 present the internal surface areas of interest plot in each injector case.

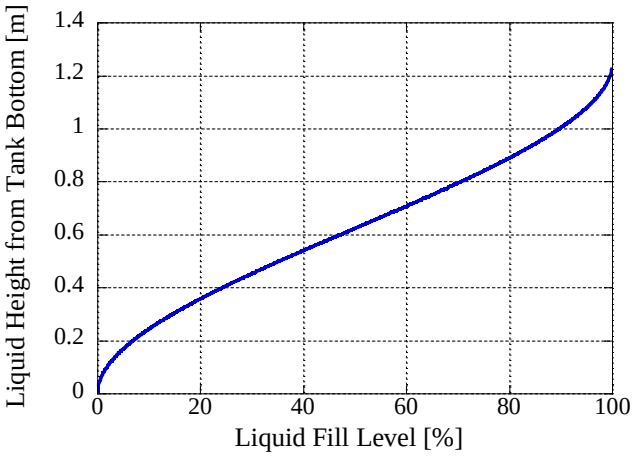

Figure 4.16: Liquid-Vapor Interface Height above Tank Bottom in Chato et al. (1993)

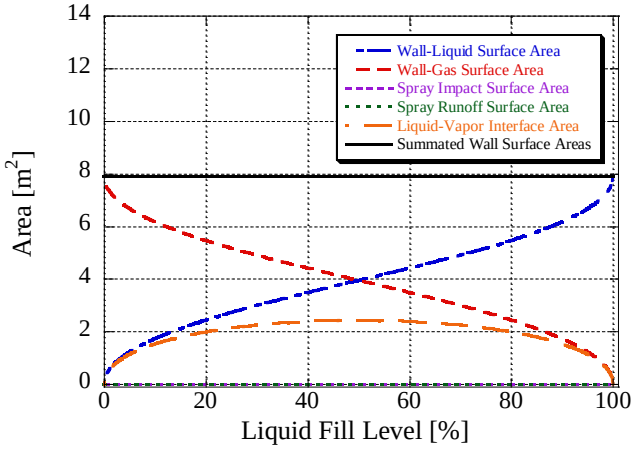

Figure 4.17: Internal Surface Areas of Interest for the Bottom Jet in Chato et al. (1993)

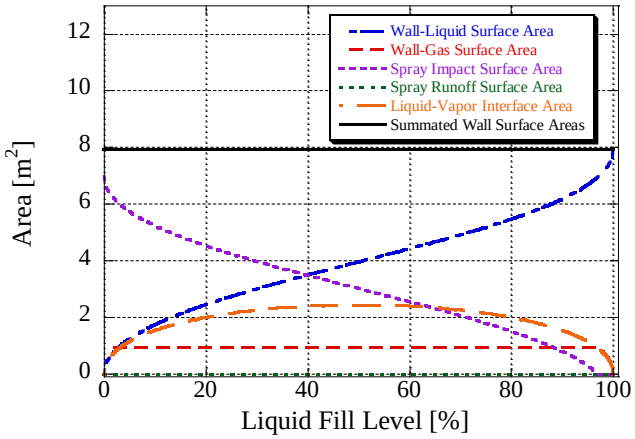

Figure 4.18: Internal Surface Areas of Interest for the Spray Bar in Chato et al. (1993)

Chapter 4.8: Model Application to the Tank-Injector Configuration in Kim et al. (2016)

The geometry of Kim et al. (2016) is unique in that it is the only historical test to use a simple cylindrical tank. Additionally, Kim et al. (2016) utilizes a nozzle at the top of the tank to inject liquid, acting similarly to a dip tube. Figures 4.19 and 4.20 present the liquid-vapor interface height above the tank bottom and the internal surface areas of interest plots. Notably, at the beginning and end of fill (0% and 100% filled) the wall-gas surface area sharply decreases, and the wall-liquid surface area sharply increases, respectively. Both cases are due to the liquid suddenly covering one of the ends of the cylinder.

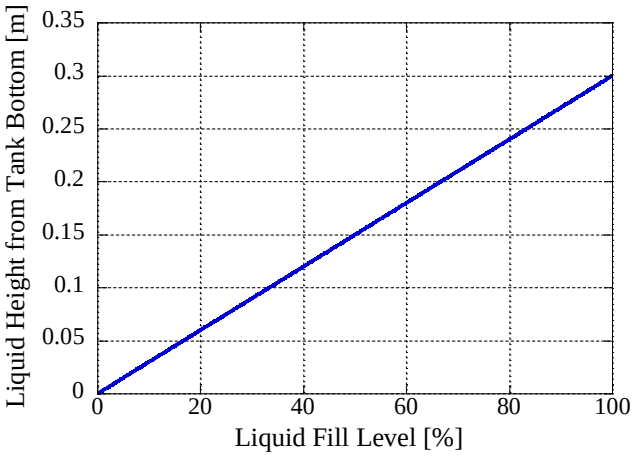

Figure 4.19: Liquid-Vapor Interface Height above Tank Bottom in Kim et al. (2016)

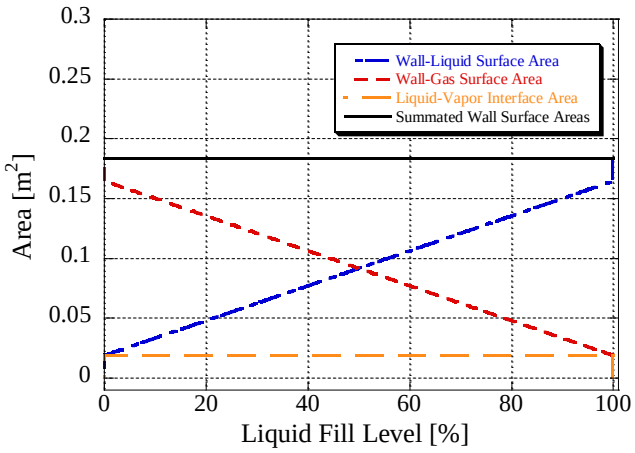

Figure 4.20: Internal Surface Areas of Interest in Kim et al. (2016)

Chapter 4.9: Model Application to the Tank-Injector Configuration in Hartwig et al. (2021)

The CRYOgenic Orbital TEstbed (CRYOTE) 2 experiment assessed in Hartwig et al. (2021) utilized a spherical tank with multiple injector styles. The first injector, the 16-hole inverted shower head, sits about 8 cm below the lid and shoots the spray upwards in a 90-degree cone. The second injector, the 8-hole inverted shower head with a single top spray nozzle, sits

about 8 cm below the lid and again shoots the spray upwards in a 90-degree cone. However, this injector also emits the spray downwards at 170 degrees, with the downward spraying portion of the injector sitting a few centimeters below the upwards spraying portion. The third injector uses three spray nozzles, and sits about 8 cm below the lid, shooting spray both upwards and downwards at 170 degrees, with the downward spraying portion of the injector again sitting a few centimeters below the upwards spraying portion. Figure 4.21 presents the liquid-vapor interface height above the tank bottom for all injector cases, and Figures 4.22 through 4.24 present the internal surface areas of interest for each injection method. Notice for the 16-hole inverted shower head how the spray impact area is quite small, while the runoff area is large. This difference exists because the injector sits close to the top of the tank, spraying upwards and causing only a small portion of the tank to be impacted by spray, leaving the remaining exposed tank surface area able to have runoff liquid.

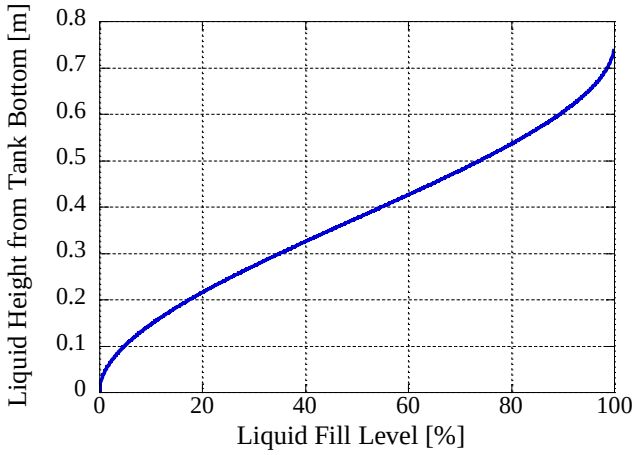

Figure 4.21: Liquid-Vapor Interface Height above Tank Bottom in CRYOTE

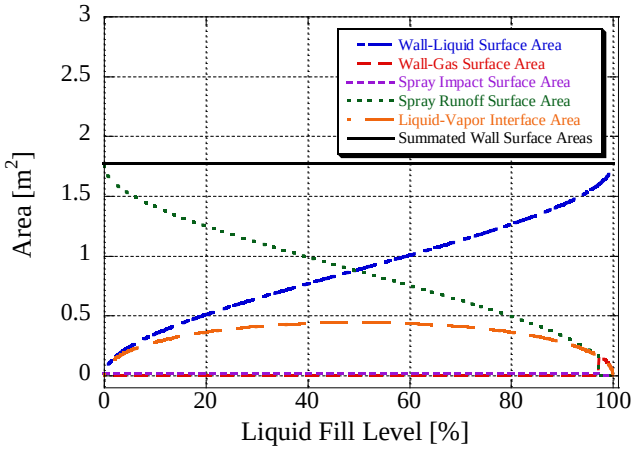

Figure 4.22: Internal Surface Areas of Interest for the 16 Hole Inverted Shower Head in CRYOTE

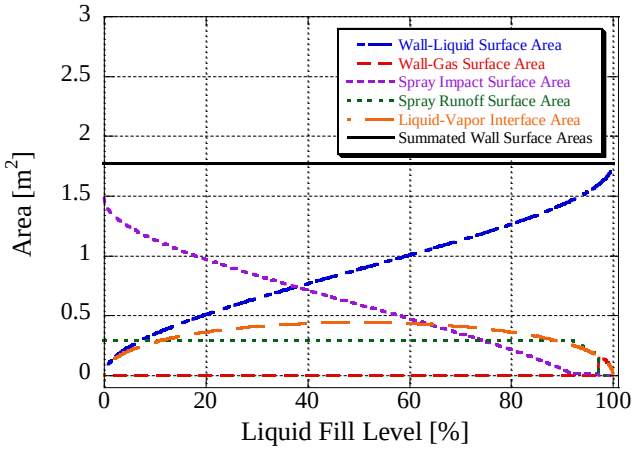

Figure 4.23: Internal Surface Areas of Interest for the 8 Hole Inverted Shower Head and Single Spray Nozzle in CRYOTE

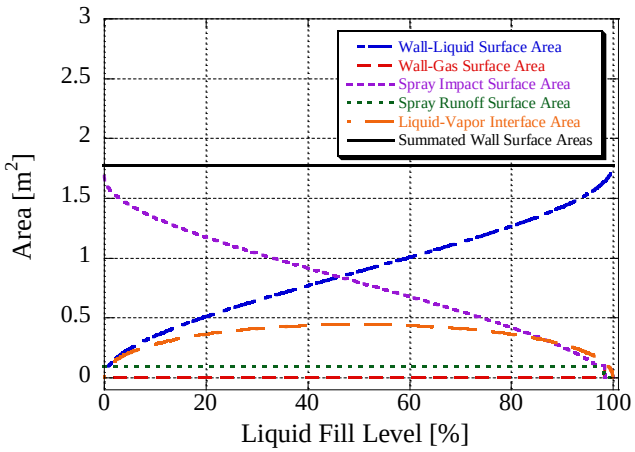

Figure 4.24: Internal Surface Areas of Interest for the 3 Spray Nozzle Injectors in CRYOTE

Chapter 4.10: Chapter Review and Future Work

This chapter has introduced a trajectory subroutine as a part of a 1st order transient thermodynamic modeling effort to accurately predict success or failure of a no-vent fill. The subroutine reliably outputs the necessary geometric parameters for the thermodynamic model based on the entered tank geometry, injector, and associated dimensions. The subroutine makes use of an axisymmetric assumption and assumes that gravity does not significantly affect the spray trajectories, since the flow moves sufficiently fast. Therefore, the subroutine could be made more accurate by allowing non-axisymmetric cases to be calculated, and by accounting for the effect of gravity on the spray trajectory, if the user would opt to include it.

Overall, though, this trajectory subroutine represents a major component of NASA's transient thermodynamic model and will help enable accurate predictions and subsequent designs for successful NVF and NVTO transfers. As such, successful and more efficient cryogenic fuel transfer methods can be developed, and a major step towards realizing on-orbit refueling and unlocking its potential can now be taken.

Chapter 5: Conclusions and Closing Remarks

This thesis has presented research aimed at enabling the efficient use of on-orbit refueling depots for cryogenic fuels and focuses on the orbital mechanics applications and the thermodynamic processes of realizing that goal. On the topic of orbital refueling, this thesis attempts to determine if optimal refueling depot orbits exist, and indeed it was found that significant mass savings can be realized by placing the depot in a more optimal orbit, and a preliminary method for determining these orbits can be devised

However, optimizing refueling orbits is only one requirement for realizing future fuel depots. Still though, more engineering needs to be performed to understand and ultimately enable reliable propellant transfer. Therefore, the thermodynamic processes of on-orbit refueling are also addressed to find an answer to the question of how to refuel warm tanks efficiently with cryogenic fuels when cryocooler technology is unavailable. A parameter for predicting the success of no-vent fill cryogenic fuel transfers has been defined, and successfully applied to 158 refueling historical tests performed in a 1-g environment. However, it has been shown in this thesis that a 0^{th} order thermodynamic model cannot fully characterize the refueling process, since the process is inherently path dependent. Therefore, a higher order model is needed to accurately predict the thermodynamics of the fill process. The author's contribution to a first order, 1-g, transient model being created by NASA's Reduced Gravity Cryogenic Transfer research group was discussed. Specifically, the author has created a set of trajectory scripts to extract the necessary geometric characteristics of injector-tank pairs, including spray impact area, liquid-vapor interfacial area, and spray impingement angle. A reader might ask why a computational fluid dynamics (CFD) software approach was not the primary method of investigation, due to its increased potential for accuracy over a nodal 1^{st} order transient model. However, CFD

simulations would likely be much more computationally expensive than a scripted nodal model and also lack basic "initial test conditions" at a sufficient level to anchor the model. Additionally, the 1st order transient nodal model has the ability to implement correction factors to incorporate empirical data. Therefore, the faster 1st order transient nodal model is a "simple initial tool" to predict when an NVF may be successful, while CFD could be used to assess specific tank and injector designs later in the fuel depot's detailed design process.

The research in this thesis is a meaningful contribution to the optimal utilization of on-orbit refueling depots, in areas of orbital location and propellant transfer. In a future where orbital refueling is fully realized, one could envision spacecraft that travel between refueling depots, en-route to their destinations, utilizing common fuels and rendezvousing with a range of depot types, depending on the mission. Additionally, depots themselves might travel between orbits (perhaps with OTVs) in order to meet the customer craft in a more beneficial orbit, and then travel back to a different orbit to refuel, utilizing Earth-produced fuels or ISRU-produced fuels. From this point these depots might even be filled and positioned deep in the solar system, well before a human mission arrives to use them. This approach would be akin to laying the railroad tracks before the train, so as to ultimately enabling a less expensive, infrastructure-based expansion of human life into the solar system and to allow the next phase of human space exploration to begin.

References

Adams R. B., Richardson, G. A. “Using the Two-Burn Escape Maneuver for Fast Transfers in the Solar System and Beyond” *NASA Archives.* 2010.

Banerjee, B. “An evaluation of plastic flow stress models for the simulation of high-temperature and high-strain-rate deformation of metals” DOI: 10.13140/RG.2.1.4289.9285 December, 2005.

Bentz, D., Prasad, K. “Thermal Performance of Fire Resistive Materials I. Characterization with Respect to Thermal Performance Models” *U.S. Department of Commerce* Ed. NISTIR 7401 February, 2007.

Borough, P. “Orbit of the Moon around the Earth” October 2019. Retrieved July 15, 2020, from https://www.peterboroughastronomy.com/LearningCentre/Novice%20Handouts/Novice%20Lesson%204%20Handout%20-%20SunMoonEarth.pdf.

Breon, S. R., Boyle, R. F., Francom, M. B., DeLee, C. H., Francis, J. J., Mustafi, S., Barfknecht, P. W., McGuire, J. M., Krenn, A. G., Zimmerli, G. A., Hauser, D. M. “Robotic Refueling Mission-3—an overview” *NASA Archives*. 2019.

Brown, T. M. “NASA Cryogenic Propellant Management Technology Efforts” *2019 AIAA Propulsion and Energy Forum* Indianapolis, Indiana, 19-22 August 2019. Retrieved 16 February 2021, from https://ntrs.nasa.gov/citations/20190030460

Buyco, E.H., Davis, F.E. “Specific Heat of Aluminum from Zero to Its Melting Temperature and Beyond. Equation for Representation of The Specific Heat of Solids” *Journal of*

Chemical & Engineering Data 15 (4), 518-523, DOI: 10.1021/je60047a035 October, 1970.

Chato, D. J. "Technologies for Refueling Spacecraft On-Orbit" *NASA Archives.* 2000.

Chato, D.J. "Ground Testing on the Nonvented Fill Method of Orbital Propellant Transfer: Results of Initial Test Series" *NASA-TM-91-2326* June, 1991.

Chato, D.J., and Sanabria, R. "Review and Test of Chilldown Methods for Space-Based Cryogenic Tanks" *NASA-TM-104458* June, 1991.

Chato, D.J., Moran, M.E., and Nyland, T.W. "Initial Experimentation on the Nonvented Fill of a 0.14 m^3 (5 ft^3) Dewar with Nitrogen and Hydrogen" *NASA-TM-103155* June, 1990.

Clark, J., Hartwig, J., "Assessment of Prediction and Efficiency Parameters for Cryogenic No-Vent Fill" *Cryogenics* 2021.

Clark, J., Horack, J., Newton, E., "Assessment of On-Orbit Cryogenic Refueling: Optimal Depot Orbits, Launch Vehicle Mass Savings, and Deep Space Mission Opportunities" *The 71st International Astronautical Congress*, 12-14 October 2020.

Das, K. "Heat Capacity of Solids in the Debye Approximation" Retrieved March 29, 2020, from demonstrations.wolfram.com/HeatCapacityOfSolidsInTheDebyeApproximation/ March, 2011.

Dunbar, B., Mohon, L. "Space Launch System (SLS) Overview" July 2020. Retrieved 20 July 2020, from https://www.nasa.gov/exploration/systems/sls/overview.html.

Flachbart, R.H., Hedayat, A., Holt, K.A., Sims, J., Johnson, E.F., Hastings, L.J., Lak, T. “Large-Scale Liquid Hydrogen Tank Rapid Chill and Fill Testing for the Advanced Shuttle Upper Stage Concept” *NASA/TP-2013-217482* April, 2013.

Gillespie, R. W. “Impulse Propulsion Gains Resulting from “Free” Retanking of Propellants on Various Orbits and Stations at the Earth, the Moon, Mars, and Venus” Proceedings on the Working Group on Extraterrestrial Resources - Fourth annual meeting *NASA Archives* 312-340. 1964.

Glaister, D., Schmidt, J., McLean, C., Mills, G. “Long Term Cryogenic Storage Technologies Overview for NASA Exploration Applications” *42nd AIAA Thermophysics Conference*, Honolulu, Hawaii, 27-30 June 2011. Retrieved 6 February 2021, from https://arc.aiaa.org/doi/pdf/10.2514/6.2011-3774.

Glasstone, S. “Sourcebook on the Space Sciences” *D. Van Nostrand Company, Inc*. 209. 1965.

Graham, S. “How Spacecraft Fly” *Praxis Publishing* 103-104. 2008.

Hartwig, J.W., Rhys, N., Clark, J., Mercado, M., LeClair, A., and Majumdar, A. “Test Data Analysis of the Vented Chill, No-Vent Fill Liquid Nitrogen CRYOTE-2 Experiments” *International Journal of Heat and Mass Transfer* 2021.

Heaton, A. F., Sood, R. “Space Launch System Departure Trajectory Analysis for Cislunar and Deep-Space Exploration” *NASA Archives*. 2020.

Hurst J.E. Jr, & Harrison, K.B. “Estimation of Liquid and Solid Heat Capacities Using A Modified Kopp's Rule” *Chemical Engineering Communications*, 112:1, 21-30, DOI: 10.1080/00986449208935989 June, 1991.

Izzo D. “esa/pykep: Major update. (Version 2.0)” 20 November 2017. Retrieved June 10, 2020, from http://doi.org/10.5281/zenodo.1063506

Izzo, D. “Tutorial1-PorkChopPlots.ipynb” 2016. Retrieved May 20, 2020, from https://gist.github.com/darioizzo/10643082#file-tutorial1-porkchopplots.

JetBrains, “PyCharm 2019.3.2 (Community Edition)”. 2019.

Johnson, W.L., Rhys, N.O., Bradley, D.E., Wollen, M., Kutter, B., Gravlee, M., and Walls, L.K. “Cryogenic Orbital Testbed (CRYOTE) Ground Test Article” *NASA-TM-218827* February, 2015.

Keefer, K.A. and Hartwig, J.W. “Development and Validation of an Analytical Charge-Hold-Vent Model for Cryogenic Tank Chilldown” International Journal of Heat and Mass Transfer 101, 175 – 189. 2016.

Kim, Y., Lee, C., Park, J., and Jeong, S. “Experimental Investigation on No-Vent Fill Process using Tetrafluoromethane (CF4)” *Cryogenics* 74, 123 – 130. 2016.

Kutter, B., Zegler, F., O’Niel, G., Pitchford, B., “Practical, Affordable Cryogenic Propellant Depot Based on ULA’s Flight Experience” *AIAA SPACE 2008 Conference and Exposition,* San Diego, California, 9-11 September 2008. Retrieved 6 February 2021, from https://www.ulalaunch.com/docs/default-source/extended-duration/a-practical-affordable-cryogenic-propellant-depot-based-on-ula's-flight-experience.pdf.

Kyle E., Mohon, L. “Space Launch Report - Space Launch System Data Sheet” May 2020. Retrieved July 19, 2020, from http://www.spacelaunchreport.com/sls0.html.

Lemmon, E.W., Bell, I.H., Huber, M.L., McLinden, M.O. “NIST Standard Reference Database 23: Reference Fluid Thermodynamic and Transport Properties-REFPROP, Version 9.0” National Institute of Standards and Technology, Standard Reference Data Program, Gaithersburg, 2010.

Ma, Y., Li, Y., Zhu, K., Wang, Y., Wang, L., Tan, H. “Investigation on no-vent filling process of liquid hydrogen tank under microgravity condition” 25 February 2017. *International Journal of Hydrogen Energy*, 42, 8264-8277. doi:10.1016/j.ijhydene.2017.02.198

Majumdar, A. “No Vent Tank Fill and Transfer Line Chilldown Analysis by Generalized Fluid System Simulation Program (GFSSP)” *Thermal and Fluids Analysis Workshop (TFAWS) 2013 IEEE Aerospace* Daytona Beach, Florida, 29 July-3 August 2013. Retrieved 6 February 2021, from https://ntrs.nasa.gov/citations/20140002987.

The Mathworks Inc, “MATLAB Version 9.7 (R2019b)”. 2019.

McLean, C., Pitchford, B., Mustafi, S., Wollen, M., Walls, L., Schmidt, J. “Simple, Robust Cryogenic Propellant Depot for Near Term Applications” *2011 IEEE Aerospace Conference* Big Sky, Montana, 5-12 March 2011. Retrieved 6 February 2021, from https://sciences.ucf.edu/class/wp-content/uploads/sites/58/2017/02/Propellant-Depots-IEEE-2011.pdf.

Moran, M.E. and Nyland, T.W. “Hydrogen No-Vent Fill Testing in a 5 Cubic Foot (142 Liter) Tank using Spray Nozzle and Spray Bar Liquid Injection” *NASA-TM-105759* July, 1992.

Moran, M.E., Nyland, T.W., and Driscoll, S.L. “Hydrogen No-Vent Fill Testing in a 1.2 Cubic Foot (34 Liter) Tank” *NASA-TM-105273* October, 1991.

Musk E. “Making Humans a Multiplanetary Species” *The 67th International Astronautical Congress*, Guadalajara, Mexico, 26-30 September 2016. Retrieved 23 July 2020, from https://www.spacex.com/media/making _life_multiplanetary_2016.pdf.

Musk, E. “Becoming a Multiplanet Species” *The 68th International Astronautical Congress*, Adelaide, Australia, 25-29 September 2017. Retrieved 22 July 2020, from https://www.spacex.com/media/making_life_multiplanetary-2017.pdf.

NASA Technology Transfer Program, “General Mission Analysis Tool (GMAT) Version R2018a”. 2018.

NASA, “Proceedings on the Working Group on Extraterrestrial Resources - Fourth annual meeting” *NASA Archives* 57-61. 1964.

National Institute of Standards and Technology, “Material Properties: 5083 Aluminum (UNS A95083)” Retrieved March 29, 2020, from trc.nist.gov/cryogenics/materials/5083%20Aluminum/5083Aluminum_rev.htm

National Institute of Standards and Technology, “Material Properties: 6061-T6 Aluminum (UNS A96061)” Retrieved March 29, 2020, from trc.nist.gov/cryogenics/materials/6061%20Aluminum/6061_T6Aluminum_rev.htm

National Institute of Standards and Technology, “Material Properties: 304 Stainless (UNS S30400)” Retrieved March 29, 2020, from trc.nist.gov/cryogenics/materials/304Stainless/304Stainless_rev.htm

Smith, D. A. “Space Launch System (SLS) Mission Planner’s Guide” *NASA Archives*. 2017.

Stephens J. R., W. L. Johnson, “Cryogenic Fluid Management: Technology Development

Roadmaps" *NASA Archives*. 2017.

Titanium Metals Corporation. (1998). "Properties and Processing of TIMETAL 6-4" Retrieved October 31, 2019, from https://www.timet.com/assets/local/documents/technicalmanuals/TIMETAL_6-4_Properties.pdf.

U.S. House of Representatives, Committee on Science and Astronautics, "H.R. 5466: 1964 NASA Authorization Hearings" *NASA Archives* 148-149. 1963.

Appendix A: Refueling Theory Proof

This proof begins by considering the example of a single stage rocket with a predetermined engine specific impulse (Isp), ratio of rocket structural mass to propellent mass (η), and payload mass (m_{pay}). Equation A1 below demonstrates how these parameters relate to the change in velocity of the craft, or delta-V (ΔV), with m_0 being the initial, wet mass of the spacecraft with payload, and mf being the final, dry mass of the spacecraft with payload. Additionally, m_{p0} is the mass of the propellant with no (zero) refueling depots in place, m_{s0} is the mass of the spacecraft structures with no refueling depots in place, and g_0 is the acceleration due to gravity on the surface of the Earth (9.81 m/s^2).

$$\Delta V = g_0 Isp \ln\left(\frac{m_0}{m_f}\right) = g_0 Isp \ln\left(\frac{m_{s0} + m_{p0} + m_{pay}}{m_{s0} + m_{pay}}\right) = g_0 Isp \ln\left(\frac{\left(\frac{1}{\eta} - 1\right) m_{p0} + m_{p0} + m_{pay}}{\left(\frac{1}{\eta} - 1\right) m_{p0} + m_{pay}}\right) \quad \text{(A1)}$$

If the rocket had the ability to stop mid-way through its mission and refuel to split the total, required delta-V (burn time) between multiple burns, the overall change in velocity equation would become Equation A2 below, with only parameter changing being the mass of the propellant and therefore the structural mass of the spacecraft as well.

$$\Delta V = g_0 Isp \ln\left(\frac{\left(\frac{1}{\eta} - 1\right) m_{p1} + m_{p1} + m_{pay}}{\left(\frac{1}{\eta} - 1\right) m_{p1} + m_{pay}}\right) + g_0 Isp \ln\left(\frac{\left(\frac{1}{\eta} - 1\right) m_{p1} + m_{p1} + m_{pay}}{\left(\frac{1}{\eta} - 1\right) m_{p1} + m_{pay}}\right) \quad \text{(A2)}$$

From here a general equation can be extracted for the division of the total burn time across N segments through utilization of N-1 refueling depots. Refer to Equation A3 below.

$$\Delta V = \sum_{i=1}^{N} g_0 Isp \ln\left(\frac{\left(\frac{1}{\eta}-1\right)m_{pN}+m_{pN}+m_{pay}}{\left(\frac{1}{\eta}-1\right)m_{pN}+m_{pay}}\right) = N g_0 Isp \ln\left(\frac{\left(\frac{1}{\eta}-1\right)m_{pN}+m_{pN}+m_{pay}}{\left(\frac{1}{\eta}-1\right)m_{pN}+m_{pay}}\right) \quad \text{(A3)}$$

Of course, for any number of refueling events chosen and an overall mission delta-V selected, the overall craft mass can be numerically solved and potential mass savings over the no-refueling case can be computed. In order to help visualize potential mass savings, an example single-stage rocket with an Isp of 400 seconds, a mass ratio of 0.95, a payload mass of 1000 kg, and required delta-Vs varying from 0 to 10 km/s are plotted for 0 through 10 refueling depots in place. Note that mass savings is defined as the total mass used in the no-refueling case divided by the total mass used in a case with N refueling events. Figure A1 below shows the specific results with N = 1 refueling depot, with mass normalized relative to payload mass. Figure A2 then shows how the number of refueling depots utilized affects the overall mass savings for the same parameters used. It can be seen here how utilization of refueling in general can prove worthwhile, with utilization of one refueling station specifically producing the largest benefit relative to the previous state. Additionally, as more refueling depots are added, the less the benefit of refueling becomes and a limit is approached. Finally, it can also be seen that as a mission requires more delta-V, the greater the mass savings resulting from orbital refueling become, and the more sense it makes to utilize orbital refueling. This supports the idea introduced in Chapter 1 that as more ambitious missions become necessary, orbital refueling will become more relevant or even necessary as well.

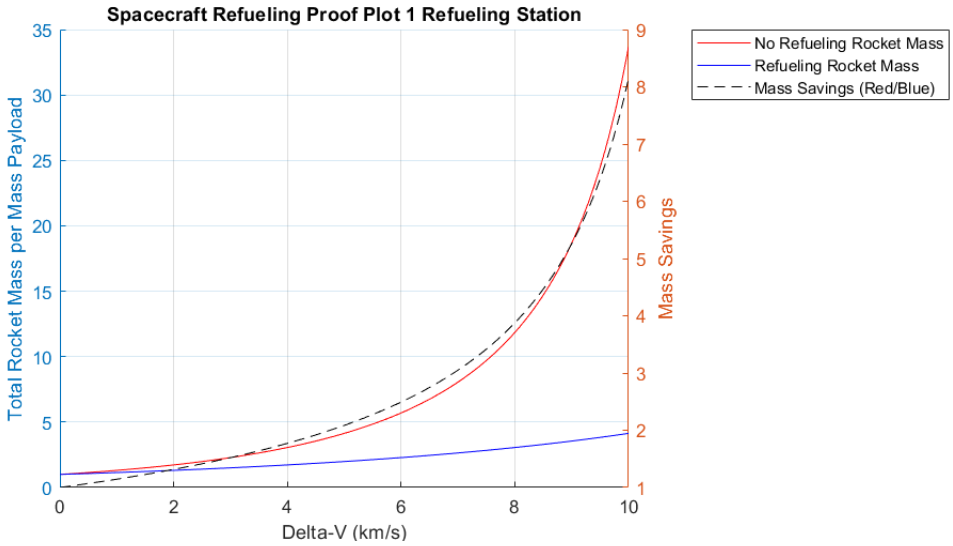

Figure A1: Total Rocket Mass as a Function of Delta-V with One Refueling Station

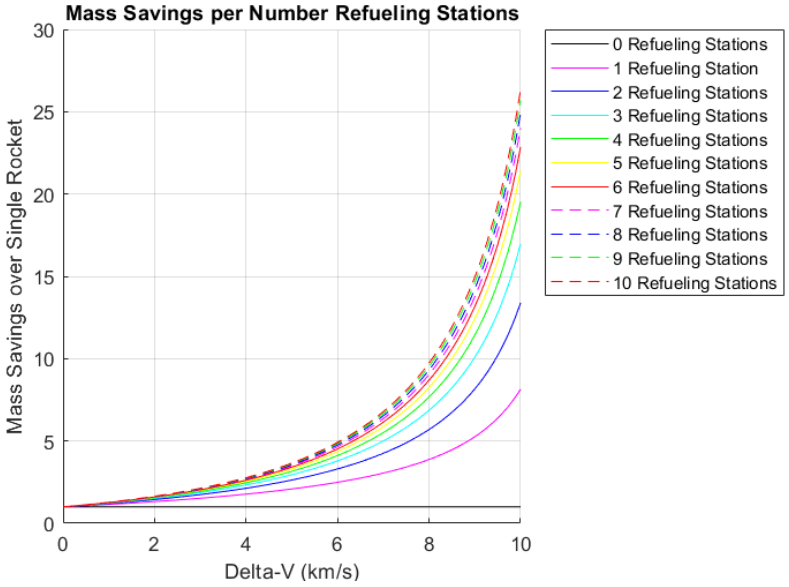

Figure A2: Mass Savings as a Function of Delta-V and the Number of Refueling Stations